Microwave Induced Plasma Sources at atmospheric pressure and Atomic Spectroscopy

Dissertation

zur Erlangung des Grades eines

Doktors der Ingenieurwissenschaften

des Fachbereichs Physik

der Universität Dortmund

Attila Michael Bilgic

spring 2000

DissDo 2000/130

DissDo 2000/130

UNIV.-BIBL.
DORTMUND

To Nora

Se non è vero, è bene trovato

Danksagung

An dieser Stelle möchte ich mich bei allen bedanken, die zum Gelingen dieser Arbeit beigetragen haben. Bei Herrn Prof. Dr.-Ing. E. Voges bedanke ich mich für die sehr gute Zusammenarbeit während der letzten vier Jahre und für die zahlreichen Diskussionen, welche immer eine Quelle neuer Ideen waren. Bei Herrn Prof. Dr. W. Weber bedanke ich mich für die freundliche Übernahme des Koreferates.

Mein besonderer Dank gilt auch den Herren Prof. Dr. J.A.C. Broekaert, Dipl.Chem. U. Engel und Dr. C. Prokisch aus der Analytischen Chemie. Die Zusammenarbeit war exzellent. Allen Kolleginnen und Kollegen des Lehrstuhls Hochfrequenztechnik, dies schließt auch Diplomanden und Studienarbeiter sowie studentische Hilfskräfte ein, bin ich ebenfalls zu Dank verpflichtet, halfen sie doch stets bei der Überwindung der kleinen alltäglichen Probleme.

I also would like to thank the group of Dr. van der Mullen at the Technische Universiteit Eindhoven and special thanks of course to himself for the exciting and interesting discussions we had.

Meiner Tochter Nora und meiner Frau Filiz danke ich für ihr Verständnis, das sie in den letzten Jahren aufgebracht haben, insbesondere während der Zeit des Verfassens dieser Arbeit.

Contents

1. Introduction 1

1.1. Atomic spectroscopy and analytical chemistry 2

1.2. Some common plasma sources in OES 3

1.2.1. Inductively Coupled Plasma ICP 3

1.2.2. Microwave induced plasmas (MIPs) 4

2. Fundamentals of Microwave Induced Plasmas 10

2.1. Characterisation of a plasma 10

2.1.1. Macroscopic neutrality 11

2.1.2. Debye shielding 12

2.1.3. Plasma and collision frequency 13

2.2. Theoretical approaches 14

2.3. Microwave induced plasmas at atmospheric pressure 15

2.3.1. Balances and Equilibrium 16

2.3.2. AC conductivity and dielectric model 19

2.3.3. Ambipolar diffusion 20

3. Coaxial Microwave Plasma Sources 23

3.1. Introduction 23

3.2. The modified Microwave Plasma Torch (MPT) 24

3.2.1. MPT as an impedance matching network 26

3.2.2. Experimental estimation of the effective plasma impedance . . 28

3.3. Thomson scattering measurements of the electron density and temperature 30

3.3.1. Principle of Thomson scattering and experimental set-up . . . 32

3.3.2. Electron density and temperature mappings under different operating conditions 35

3.4. Heavy particle temperature by spectroscopic measurements 48

3.5. Electro-magnetic fields of the MPT 50

3.5.1. Electro-magnetic field equations 51

3.5.2. Boundary conditions 53

3.5.3. Numerical approach 56

3.5.4. The electromagnetic field of the MPT without a plasma 59

3.5.5. Electromagnetic characteristics of the MPT after ignition of a plasma 60

3.6. Fluid-dynamic simulations of the MPT 70

4. Microstrip Plasma Sources **75**

4.1. Introduction . . . 75

4.2. Development and fabrication of microstrip plasma sources (MSPs) . . 76

4.2.1. Substrate processing . . . 78

4.2.2. Microstrip design and structuring . . . 78

4.2.3. Electromagnetic modelling . . . 79

4.2.4. Fluid flow modelling . . . 79

4.3. Application specific MSP designs . . . 82

4.3.1. An MSP for the optical emission spectrometric (OES) analysis of mercury . . . 82

4.3.2. An MSP for the optical emission spectrometric (OES) non-metal detection . . . 88

4.3.3. An MSP for the atomic absorption spectrometric (AAS) chlorine analysis . . . 90

5. Conclusion and final remarks **93**

A. Layouts of microstrip plasma sources **98**

B. Finite Differences on mapped grids **100**

B.1. Transformation coefficients, metric tensor and Christoffel symbols . . 100

B.2. Covariant formulation of Maxwell's equations and the vector wave equation . . . 102

B.3. Grid transformation example . . . 104

C. List of symbols **106**

D. Physical constants **108**

List of Figures

1.1. Schematic drawing of the ICP. 3
1.2. Schematic drawing of two non-resonant microwave plasma sources. The left drawing shows the elementary TIA set-up published by Moisan et al. in [1] and the right source is also developed by Moisan et al. in [2]. Both devices, however, did not find broad acceptance in OES applications. 6
1.3. Sketches of some classical MIPs used in OES. Figure a) shows the TM_{010} resonator according to Beenakker [3], the CMP shown in figure b) is taken from [4] and the Surfatron in c) is depicted in [5]. 7
1.4. The setup of the Microwave Plasma Torch (MPT) as published by Jin et al. in [6]. This plasma source was subject of manifold investigations in analytical chemistry as well as plasma diagnostic measurements. 8

2.1. Ranges of electron densities n_e and temperatures T_e for several plasma phenomena and their characteristic physical parameters as Debye length λ_D, plasma frequency ω_p and the number of electrons in a Debye sphere N_D. The photograph of an MPT plasma is shown as reference. 11
2.2. Electron energy distribution (EEDF) for a Maxwellian electron gas at electron temperatures of 5000 K, 10000 K and 20000 K. The higher the electron temperature the flatter and broader is the distribution function. 18
2.3. Ionisation degree α_{Ar} for argon with an ionisation energy of $E_{ion} \simeq 15.6\,\mathrm{eV}$ as a function of the electron temperature. 19

3.1. The modified MPT setup. Some characteristic dimensions and typical parameters are given aside the drawing. Dimensions are given for a tuned fixed setup without movable parts. 24
3.2. Equivalent circuit diagram of the MPT for the description as an impedance transformer. Definition of the amplitude scattering matrix $\mathbf{S}$. 26
3.3. Graphical representation of Poynting's theorem for the expression of a conductivity distribution as a complex impedance with reference to a waveguide opening. 27
3.4. Reflexion coefficient as a function of short stub length L_S for different incoupling positions L_T in terms of the free space wavelength λ_0. The fitting procedure yields the normalised complex plasma impedance $z_p = 0.87 + j\,0.19$. The right diagram shows matching conditions; here the short stub length is variable in a broad range thus suggesting a fixed setup without necessity for tuning elements. 29

3.5. Region for stable plasma operation in the case of the modified MPT. The Ar gas flow in the analyte channel is fixed to 250 $\mathrm{mL\,min^{-1}}$ 30

3.6. Dimensionless scattering parameter α in dependence on Debye length λ_D in μm. 33

3.7. Experimental set-up for the Thomson scattering measurement of the electron density and temperature of the MPT. 35

3.8. Photographic images of the MPT plasma under different operating conditions. The left column shows the influence of the water loading of 0 $\mathrm{mg\,min^{-1}}$, 4 $\mathrm{mg\,min^{-1}}$ and 10 $\mathrm{mg\,min^{-1}}$ from top down and the right column documents the changes of the plasma with the internal gas flow of 200 $\mathrm{mL\,min^{-1}}$, 500 $\mathrm{mL\,min^{-1}}$ and 1000 $\mathrm{mL\,min^{-1}}$, respectively. Forward power is always 100 W and outer gas flow is 200 $\mathrm{mL\,min^{-1}}$. 37

3.9. Electron density (left column) and temperature (right column) mappings for the Ar MPT operated with different internal and external gas flows; from top down: 500 $\mathrm{mL\,min^{-1}}$ and 200 $\mathrm{mL\,min^{-1}}$, 900 $\mathrm{mL\,min^{-1}}$ and 200 $\mathrm{mL\,min^{-1}}$, 500 $\mathrm{mL\,min^{-1}}$ and 700 $\mathrm{mL\,min^{-1}}$ for internal and external gas flow, respectively, at 100 W forward power. 39

3.10. Linear electron density n_e as a function of the observation height above the top of the torch. Power: 100 W; internal gas flow: 500 $\mathrm{mL\,min^{-1}}$; outer gas flow: 200 $\mathrm{mL\,min^{-1}}$. 41

3.11. Radial distribution of the electron density at observation heights of 4 mm (solid line) and 7 mm (dashed line) above the top of the MPT. Power: 100 W; internal gas flow: 500 $\mathrm{mL\,min^{-1}}$; outer gas flow: 200 $\mathrm{mL\,min^{-1}}$. . . 43

3.12. Electron density axial scans for different operating conditions. Power: 100 W; internal gas flow: 500 $\mathrm{mL\,min^{-1}}$; outer gas flow: 200 $\mathrm{mL\,min^{-1}}$ ($\triangle$); internal gas flow: 900 $\mathrm{mL\,min^{-1}}$; outer gas flow: 200 $\mathrm{mL\,min^{-1}}$ ($\square$); internal gas flow: 500 $\mathrm{mL\,min^{-1}}$; outer gas flow: 700 $\mathrm{mL\,min^{-1}}$ ($\times$). 44

3.13. Influence of water on the electron density (straight line) and the electron temperature (dotted line). Data for the centre of the plasma at an observation height of 7 mm above the top of the MPT. 45

3.14. Influence of the microwave forward power on the electron density (straight line) and the electron temperature (dotted line). Data for the centre of the plasma at an observation height of 7 mm above the top of the MPT. 47

3.15. Lateral scan of the rotational temperature of the OH radical in an MPT plasma (upper picture). Radial scan of the rotational temperature resulting from numerical Abel inversion (lower picture). 49

3.16. Schematic drawing of the upper end of the Microwave Plasma Torch (MPT). The computation domain is indicated by a grey background; the excitation boundary (dotted lines) is sufficiently deep in the coaxial line for a pure TEM field configuration. 53

3.17. The different convergence behaviours of the iterative solver CGS and BiCGStab for a typical FD problem on a mapped grid. 58

3.18. Contour (left) and vector (right) plot of the electrical field in the MPT without an operating plasma. The highest field strengths are localised around the outer corner of the inner conductor with approximately 200 kV m^{-1}. There is almost no microwave radiation leaving the plasma source. An integration of the Poynting vector around the computation domain boundary delivers a total radiated power of less than 3 W. The contour lines are scaled logarithmically; this applies to all following figures. 61

3.19. Electron-ion- ($\bar{\nu}_{ei}$) and electron-atom-collision frequency ($\bar{\nu}_{ea}$) for elastic momentum transfer. The frequencies are proportional to n_i and n_a, respectively. Here, $n_i = 2 \cdot 10^{20}\, m^{-3}$, $n_a = 2 \cdot 10^{24}\, m^{-3}$ ($\hat{=}$ 3600 K) $\Rightarrow \alpha = 10^{-4}$ are assumed. In addition, $\tilde{\nu}_{ea}$ and $\tilde{\nu}_{ei}$ (dotted lines) are plotted with variable n_a from the ideal gas-law (see text) and $n_i = \alpha n_a$. The sum of $\tilde{\nu}_{ea} + \tilde{\nu}_{ei}$ is only weakly dependent on T_e between 5000 K and 25000 K for constant pressure and ionisation degree α. 62

3.20. Analytical function to describe the electron density distribution of the MPT plasma. The parameter of the function are fitted to Thomson scattering data and reproduce the experimental values within the measurement domain with high accuracy. On the left side a density plot of the assumed electron density is shown, the right plots show the variation of some sub-functions of the analytical electron density approximation with the hight z above the torch: solid line $a(z)$, dotted line $b(z)$ and dashed lined $d(z)$. 64

3.21. Contour plot of the real part (right) and imaginary part (left) of the complex plasma dielectric constant. The corresponding specific conductivity distribution σ_{pl} follows from multiplying the shown values by the factor $\varepsilon_0 \omega \approx {}^{1}/_{7.3} (\Omega\ \mathrm{m})^{-1}$. The contour lines are scaled logarithmically; this applies to all following figures. 65

3.22. Contour (left, time averaged absolute value) and vector (right, temporal snapshot) plot of the electric field in the MPT with an operating plasma. The highest field strengths are localized around the lower outer boundary of the plasma just above the torch with approximately 60 kV m^{-1}. 66

3.23. Contour plot of the time averaged magnetic field $\mathbf{H}_\varphi$ of the MPT plasma in the full computation domain (left) and a magnified section showing the plasma region (right). The plots show that the plasma is confined by strong induced currents especially around the small spot of high electron density (hot spot). 67

3.24. Contour plot of the real part of the complex Poynting vector. The left plot shows the whole computation domain while the right plot shows a magnification of the plasma region. Integrating the Poynting vector along a volume enclosing the plasma shows that approximately 55 W is radiated into the surrounding. 69

3.25. Contour (left) and hill (right) plot of the power density in the MPT plasma. The highest values are reached at the "hot spot" inside the plasma 7 mm above the torch ending rapidly decreasing towards the plasma boundaries. The hill plot clearly shows the extreme gradients in the power density distribution. 71

3.26. Coloured contours of the power density P_A (right) and the time averaged electric field strength $\langle|\mathbf{E}|\rangle$ (left) in the MPT plasma. The colour gradients are scaled logarithmically to represent a broad range of values which can be depicted from the colour lookup table below the plot. This figure also very clearly shows the so called hollow structure of the MPT plasma, i.e. a region of low energy density inside the lower part of the toroidal plasma. . . 72

3.27. Two exemplary calculations of the Ar gas flow of the MPT performed with a commercial code (FLUENT). The upper picture shows the magnitude of the velocity field in m s^{-1} of a cold (300 K) Ar gas flow at standard conditions. The lower one includes an localized volumetric energy in-coupling of 10^{10} W m^{-3} over a torus above the inner conductor; velocity magnitudes have to be scaled by the factor 2. 74

4.1. Schematic drawing of a microstrip line on a substrate with dielectric constant ε_r and loss tangent δ_{ε_r}. 77

4.2. Electrostatic field of an MSP based on fused silica. The upper graph shows the electric field along the $x = 0$ (symmetry) axis for differently shaped gas channels. The applied voltage for all electrostatic calculations is 1 V. Obviously, the flat horizontally oriented form, i.e. along the x-axis is most favourable for highest field strengths in the channel. For comparison, the flat channel configuration is also included for a sapphire substrate. The lower picture shows the spatial electric field distribution. 80

4.3. Gas temperature distribution at different operating conditions inside the channel of a sapphire MSP with 0.9 mm cross section. From top to bottom: Ar at $P = 10$ W, $\dot{V} = 500$ mL min^{-1}; ditto for He; Ar at $P = 20$ W, $\dot{V} = 200$ mL min^{-1}; ditto for He. 81

4.4. Microstrip Plasma Source I (MSP I). The Plasma is confined in the gas channel under the central transmission line. It is reproducibly ignited there with the aid of a high voltage spark. The tapering of the central transmission line at the two open endings reduces the electrical field strength thus preventing a plasma ignition there. 82

4.5. Power and gas-flow range for a stable Ar plasma and low reflected power. The contour lines indicate areas of constant amplitude reflection coefficient. 83

4.6. CV-FI-MSP-OES set-up used. 85

4.7. Emission spectrum of a 15 W Ar MIP in the MSP (left) and calibration curve for Hg. This is obtained with standard solutions containing Hg between 0.5 and 10 ng mL^{-1} (Plasma conditions are 30 W forward power and an Ar gas flow of 300 mL min^{-1} plasma gas plus 400 mL min^{-1} carrier gas flow). 86

4.8. MSP II design and photograph with operating Ar plasma. 87

4.9. MSP II with separated aerosol introduction channels. 87

4.10. Microstrip plasma source for He (MSP III). The quadratic sapphire wafer is 30 mm long and 1.5 mm thick. It has a grown-in channel of 0.9 mm in diameter. The microstrip line has a width of 0.8 mm. Photograph of the MSP IV. The plasma can easily be recognised as the bright spot below the end of the microstrip. 88

4.11. CCD spectrum of $HCCl_3$ vapour volumes (absolute amount of $4\,\mu g$ ($20\,\mu l$) and $4\,\mu g$ ($50\,\mu l$), respectively) introduced into the plasma gas flow. The lines are shifted for a better graphical representation but belong both to the Cl (I) line at 912.1 nm 90

4.12. Schematic drawing (left) and photo (right) of an MSP IV device for LD-AAS operated at a modulated power of 13.5 W 91

4.13. Calibration for *Cl* in a He plasma of an MSP IV with LD-AAS. 91

B.1. Grid transformation example. 101

B.2. Covariant and contravariant base vectors of a curvilinear coordinate system. 103

List of Tables

1.1. Some low-temperature plasma sources grouped according to their properties. All examples but the ICP are microwave induced plasma sources. 5

2.1. Characteristic parameter of a typical atmospheric pressure microwave induced plasma in argon. 14

2.2. Proper balances: the momentum of the interacting particles prior to the collision are denoted with p and afterwards with p'. Particles symbolised with S do not suffer a change of internal energy, e.g. electrons or atoms after elastic collisions. For the Saha balance E_{q^+} includes the ionisation energy E_{ion}. 17

3.1. Some finite difference calculation results of the electromagnetic field of the MPT grouped in impedance transformation, field strengths and power. . . . 70

Abstract

This thesis deals with microwave induced plasma sources primarily operated at atmospheric pressure in noble gases like argon or helium. These are mainly used as radiation sources in analytical chemistry, here with a strong focus on atomic emission and absorption spectroscopy. The approach covers experimental and theoretical studies of plasma sources as well as research on the generated plasmas. Two fundamentally different techniques are used here, the construction of coaxial waveguide elements like the Microwave Plasma Torch (MPT) and the recently proposed use of microstrip technology to sustain a plasma in a dielectric wafer (MSP). To support the design of these circuits, the coaxial as well as the microstrip sources, numerical calculations of the electromagnetic properties and fluid dynamic field simulations are carried out. While the latter ones are performed with the aid of a commercial code a sophisticated library is developed for advanced finite difference calculations on mapped grids to numerically calculate the electromagnetic fields and the derived quantities. The mathematical theory of tensor calculus and numerical grid transformations on which this method bases on is also outlined and demonstrated on the example of the MPT. These simulations are complemented by plasma diagnostic measurements like Thomson scattering to determine the electron density and temperature distribution which are important input parameter since no completely self-consistent simulations are carried out here. The gained insight in the operational principles of these kind of plasma sources is resumed and potential and already transferred improvements of design optimisations are presented together with an outlook on possible advances in simulations and further applications.

1. Introduction

Plasmas are often called the fourth aggregate state of matter and appear in an extremely large variety of different conditions ranging from very high densities and temperatures as the plasma in the sun supplying the needed energy for the earth by nuclear fusion or a very low density and temperature plasma in interstellar space, see figure 2.1 for an overview. The word plasma originates from the Greek language and means "something molded". It was first used by Tonks and Langmuir to describe the inner region of a glowing ionised gas produced by an electric discharge inside a tube where the gas as a whole remains electrically neutral [7].
Of technical interest are the so called laboratory plasmas where high temperature plasmas are primarily used in nuclear fusion research while low temperature plasmas, often called cold plasmas, are the basic tool in the industrial production of modern materials and components of high technology. These laboratory plasmas were primarily used in the semiconductor industry but they found broad acceptance in the area of surface modification and treatment and material research. Many production processes were just made possible by this technology. Plasmas are also used in light generation, neon lamps probably being the most famous representative of this kind of application. Not that popular but no less important are the plasmas used in analytical chemistry as an atomisation, ionisation and radiation source. To simplify their usage, these are commonly operated at atmospheric pressure if possible thus overcoming the need for vacuum technology otherwise significantly complicating the analysis procedures. This is the main application topic of this thesis.
These plasmas can be created by many different techniques all of which have in common that energy of some kind, in general electromagnetic, has to be transferred to the plasma. This can be done e.g. by direct current, radio frequency or microwave excitation. Here, the focus will be exclusively on microwave induced plasmas. These have several advantages over other excitation methods like a generally larger deviation from thermodynamic equilibrium, high power densities, easy scalability and cheap construction. To provide sufficient power, usually magnetron generators at 2.45 GHz frequency are employed which are available at affordable cost. One of

the basic research subject of this thesis is the principal construction of microwave plasma sources allowing for much lower than the usual power levels of several 100 W still operating at atmospheric pressure. This will relax the tight binding to the standard frequency since low power levels of several W can easily be supplied by semiconductor transmitters within a broad frequency range. In addition, it allows for an integration of many components on a single chip thus providing the basis for very small and low cost total analysis systems known as μTAS[8].

1.1. Atomic spectroscopy and analytical chemistry

The aim of analytical chemistry is to gain information about the consistence and structure of matter. Its application ranges from industry to almost all areas of every day live like medicine and nutrition. Several methods have proven to be very powerful to fulfil this task in an adequate way. One of these is the "Optical Emission Spectrometry" (OES) which is the main field of application here. The principles of OES have a long tradition and are actually quite simple. The first spectral apparatus was described by Bunsen and Kirchhoff [9] in 1860 and based on observations of flames by Brewster, Herschel, Talbot and Foucault at the beginning of the 19nth century [10]. Its usage lead to the discovery of the elements Rb and Cs [11]. The principal of OES bases on the emission and detection of element specific radiation spectra. These are produced by radiating transitions. A population of the necessary levels can be accomplished by supplying sufficient energy e.g. in the form of thermal energy like in a flame or electromagnetic energy in the case of a plasma. The exact energy transfer mechanisms are rather complex and shall not be outlined in detail here. Benoy [12] states that in the kind of plasmas under consideration here electron collisions determine the internal state distribution much more than the heavy particle collisions do. The emitted radiation can be observed with a spectrometer and element specific lines in the spectrum will tell about the presence of a certain element. Via a calibration with an analyte of know concentration quantitative measurements are possible. Absolute measurements, i.e. calibration of a radiation source once and for all, are very complicated and not used in every day work. One reason is the strong temperature dependence of the radiation. In addition, many other also more practical reasons prohibit to proceed in such a way.
During the time, many different kinds of radiation sources evolved and became more or less standard devices in analytical chemistry. Just to list some of the most popular ones one would have to mention the "Inductively Coupled Plasma" (ICP), the "Capacitively Coupled Plasma" (CMP), the "Microwave Induced Plasma" (MIP),

the plasma arc, the spark, the laser induced plasma, the "Glow Discharges" (GDC), the "Hollow Cathode Discharge" (HCD) and finally the flames. Latter are still in use for the detection of alcalines but the plasmas have a lot of advantages and are dominant in general. Processes like the dissociation, atomisation and excitation of the analyte are generally more effective in a plasmas compared to a flame. This is partially due to the higher temperatures achieved in plasmas, e.g. 8000 K in case of the ICP compared to 3200 K of a C_2H_2/O_2 flame [13]. In addition, a plasma can provide free electrons with relatively high energies (some eV depending on plasma type) which can in turn significantly contribute to the analyte excitation. And finally a plasma for OES is in general operated with noble gases like argon or helium emitting comparably simple spectra while flames have a large spectral background from molecular bands. A disadvantage may be that a plasma has to be sustained by external energy and thus requires some more apparative equipment; but this is not a major drawback nowadays.

1.2. Some common plasma sources in OES

Some commonly used plasma sources shall be presented here with a strong focus on microwave induced plasma sources, in fact the ICP will be the only representative of alternative plasma sources discussed here due to its dominant position as the standard radiation source in OES.

1.2.1. Inductively Coupled Plasma ICP

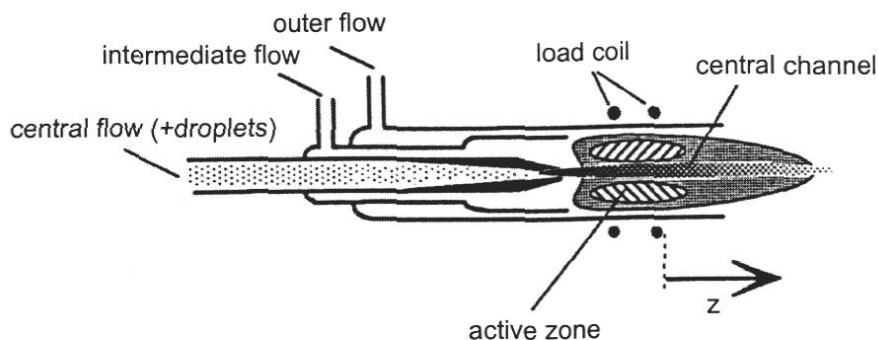

Figure 1.1.: Schematic drawing of the ICP.

The ICP was developed by Grennfield et al. [14] and Wendt and Fassel [15] in the

sixties. The first commercial ICP spectrometer presented in 1975 [16] based on Fassels plasma-burner from 1969. In the case of inductively coupled plasmas the plasma acts as the secondary coil of a transformer, in which electrons accelerated by the oscillating electromagnetic field induced by the primary coils transfer their energy to heavy particles, i.e. molecules, atoms and ions. Depending on the frequency of the induction current, the ions can also directly absorb energy from the electromagnetic field. ICPs are produced in a wide power range from several watts for medical equipment to the MW region for material treatment. The ICPs used in chemical analysis are usually operated at 1 kW or less and a gas flow of $10 - 20$ mL min^{-1} argon. The rf frequency is generally between 6 MHz and 100 MHz. Due to the skin-effect the energy in-coupling is limited to the outer sheaths of the plasma and the inner regions are heated thermically. In the standard ICP set-up the plasma is sustained via three concentric fused silica tubes, where the inner tube is supposed to be used for the analyte introduction. Thus, the analyte does not cause significant disturbances in the active plasma region where the main energy in-coupling takes place. This is one of the main reasons for the stability against even wet aerosol introduction [17, 18, 13] and this principle will be met again in other set-ups later. Another advantage of the ICP is its relatively high temperatures of 6000 K – 9000 K [19] depending on the observed region inside the plasma. All together the ICP has a large linearity (4–5 decades), low detection limits (e.g. 0.1 ng mL^{-1} for Mg and Ca) and small standard deviations ($< 1\%$ for pneumatic desolvatisation) [17].
Today ICP-OES is the standard for multi element analysis in environmental analysis [20], in clinical chemistry [21], in geology [22] or in industrial analytical chemistry [23]. Other ICP sources can also be found in lighting applications [24] or process chamber in the semiconductor industry. Much research, experimental and theoretical has been carried out to understand the processes going on in the plasma and to optimise the construction of the ICP as in [25, 26, 12], only to name a very few. And the work still goes on.

1.2.2. Microwave induced plasmas (MIPs)

These positive features of the ICP are contrasted with its high costs in construction and maintenance due to high gas flows and power levels required. It would be rather in-economic to operate e.g. a helium plasma with an ICP which in turn is important for the OES detection of non-metals [27]. And as a matter of fact, the construction of microwave induced plasmas (MIPs) leads further back in time to the fifties compared to ICPs. Their common use in spectrochemical analysis however looks upon a history of two decades. Early types of low-power MIPs such as the

TM_{010} resonator described below consists essentially of a resonant structure with little tolerance against solvent loading of the aerosol introduced into the plasma.

MIP		Non-MIP
resonant	non-resonant	
Surfatron	MPT	
Beenakker-Cavity	TPS	ICP
CMP	TIA	

Table 1.1.: Some low-temperature plasma sources grouped according to their properties. All examples but the ICP are microwave induced plasma sources.

Many efforts have been made to eliminate this shortcoming [28, 29] and several designs for improved and new MIP sources such as the Surfatron, see below, and others as in [30, 31, 1] have been proposed. Jin et al. [6] developed a new kind of source by empirically altering the Surfatron and called it a microwave plasma torch (MPT). Although historically based on the Surfatron, it actually has nothing in common with it from the operational point of view, as will be discussed in chapter 3. Recently, Moisan et al. [2] developed a new plasma source called TPS ("Torche à plasma de Surfatron"), analysed its electromagnetic characteristics and stressed the importance of a non-resonant operation. This feature together with the typically hollow structure of the plasmas generated by coaxial sources is believed to be a basic reason of the stability of these sources [32]. Accordingly, one may group the plasma sources discussed here in the categories as shown in table 1.1.

The TIA [1] and the TPS [2] did not find broad acceptance in the spectrochemical community but the TIA was frequently used as a plasma source for diagnostic measurements as in [33, 34, 35]. Some of the MIPs shown in table 1.1 are discussed in detail below.

Capacitively Coupled Plasma (CMP)

The capacitively coupled plasma was the first microwave induced plasma source used for analytical chemical purpose. It was first described by Cobine and Wilbur [36] in 1951 and investigated by Mavrodineau and Hughes [37], Jechte and Kessler [38]

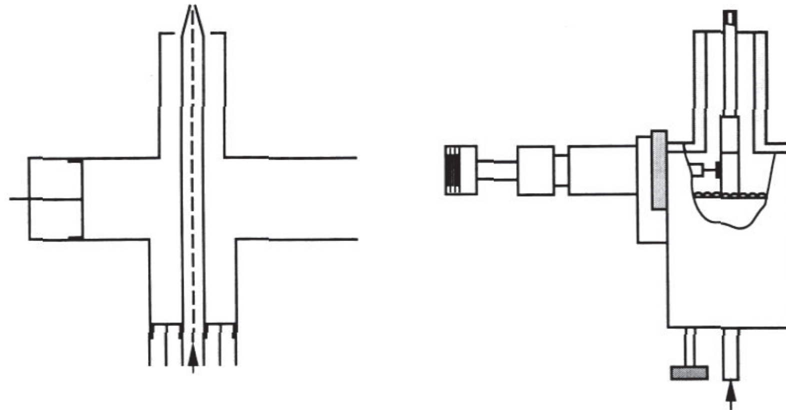

Figure 1.2.: Schematic drawing of two non-resonant microwave plasma sources. The left drawing shows the elementary TIA set-up published by Moisan et al. in [1] and the right source is also developed by Moisan et al. in [2]. Both devices, however, did not find broad acceptance in OES applications.

and Tappe and van Calker [39] for its analytical applicability in OES. The aerosol is introduced together with the plasma gas within one channel and leaves the pipe through holes in the electrode. The plasma is situated on top of this electrode in the form of filaments in the case of argon or as an ensemble of filaments for nitrogen. The direct contact of the electrode with the plasma leads to an erosion of the electrode with time even for metals with a high heat conductivity, e.g. Cu, Ag, Au, or high melting point like W and Mo. An active water cooling system is used to reduce these effects. The CMP is operated with power levels between 400 W and 800 W at gas flows typically in the $\mathrm{L\,min^{-1}}$ range. A lot of plasma diagnostical studies were carried out at the CMP generated plasmas [40, 41] and also many analytical chemical applications were performed [27, 42], nonetheless it did not found comparable acceptance as the ICP. Reasons may be the electrode–plasma contact not only destroying the former but also increasing the background due to the elements in the electrode. The detection limits are an order of magnitude worse as compared to the ICP [43], although the CMP found some specialised applications in which it can dominate the ICP in terms of cost and manuability.

$\mathrm{TM_{010}}$ resonator

To overcome the drawbacks of the electrode-plasma interaction Beenakker developed an electrodeless plasma source in *1976* [3] on the basis of a $\mathrm{TM_{010}}$ resonator. It can be operated with argon or helium with power levels between $50\,W$ and $300\,W$ and gas flows of less than $1\ \mathrm{L\,min^{-1}}$ [44]. The filament-like plasma is generated

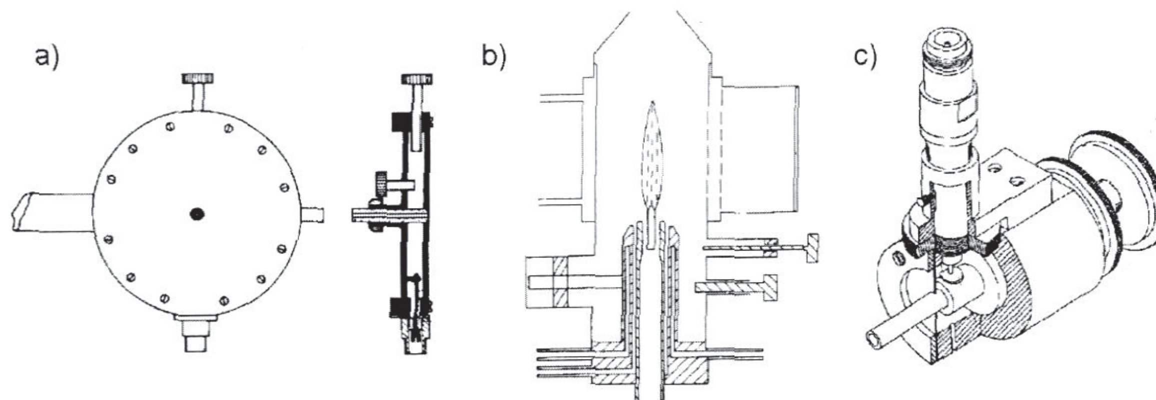

Figure 1.3.: Sketches of some classical MIPs used in OES. Figure a) shows the TM_{010} *resonator according to Beenakker [3], the CMP shown in figure b) is taken from [4] and the Surfatron in c) is depicted in [5].*

inside a fused silica tube positioned in the centre of the resonator. The analyte is introduced together with the plasma gas leading to a high analytical performance but also to the already addressed problems in stability. Here, a shift in the resonance frequency easily produced by changes in the plasma conditions like wet analyte introduction has a great effect on power in-coupling. For this reason the Beenakker-resonator is often used in connection with electro-thermal vaporisation (ETV) as analyte preparation [45, 46] or as an element specific detector in gas chromatography (GC) [47]. Therefore, the ability to sustain a helium plasma is of great importance for the detection of non-metals like the halogens which can be easily excited due to the high ionisation energy of helium.

Surfatron

In the same decade Hubert et al. published a set-up for a microwave induced plasma source called "Surfatron" [48] stemming from the surface wave effect occurring along the interface of the plasma and its surrounding capillary tube. The filament-like argon or helium plasma extends some distance out of the device depending on the power levels. These range from 20 W to 200 W at gas flows of $0.5\ \mathrm{L\,min^{-1}}$ to $2\ \mathrm{L\,min^{-1}}$. It is more stable against aerosol [5] or hydrate loading [49] as compared to the Beenakker resonator and small changes in the operating parameters like the gas flow induce only small effects on the plasma. Nevertheless, a resonance effect is used here and a tuning is necessary though not as critical as for a conventional resonator. It finds similar applications as the Beenakker resonator as a detector for GC [50, 51] and in the detection of non-metals like Cl, Br, I, C, S and P in solutions

[52] or as a detector for supercritical fluids [53] with better detection limits and higher stability [5, 54, 55].

Microwave Plasma Torch (MPT)

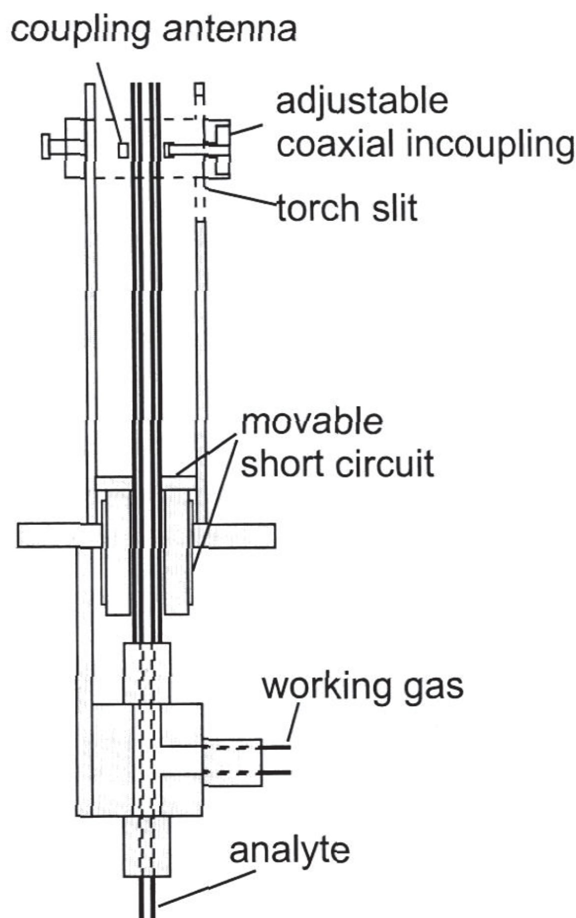

Figure 1.4.: The setup of the Microwave Plasma Torch (MPT) as published by Jin et al. in [6]. This plasma source was subject of manifold investigations in analytical chemistry as well as plasma diagnostic measurements.

Basing on the Surfatron Jin et al. empirically developed a new plasma source called the "Microwave Plasma Torch" (MPT) [6]. Despite its origination it has nothing in common with the Surfatron and its operational principals are very different. This plasma source is still subject of intense research and plays a central role in this thesis as the exemplary set-up for coaxial microwave plasma sources. Its operation parameters vary in a large range from 50 W to 500 W of forward power and 50 $\mathrm{mL\,min^{-1}}$ to 5 $\mathrm{L\,min^{-1}}$ of argon or helium gas flow producing a toroidal flame like plasma of

2 cm to 4 cm length. The plasma shape gave the device the name "torch". The use of alternative plasma gases like N_2 or air is also reported but remains an unpopular exception. It possesses a surprisingly high stability against molecular aerosol loading like H_2O or acetonitrile which is unprecedented for low power microwave plasmas. The separate plasma gas and analyte introduction as in the ICP is accounted for this feature and will be analysed throughout chapter 3. In its original design the MPT consists of three concentric metal tubes, the outer two of which form the inner and outer conductor of a coaxial wave guide as shown in figure 1.4. The plasma gas flows in-between the inner and intermediate tube and the analyte is introduced in the inner tube which can also be made of fused silica as proposed in [56]. The microwave field is coupled into the coaxial waveguide via a capacitive antenna ring around the inner conductor (intermediate tube) near the upper end of the MPT. The plasma is located above the top of the tubes without touching them, the lower end is terminated with a movable short circuit plunger for matching. In addition, the axial position of the antenna ring is also variable. Mechanical constrains cause some problems for the handling of this set-up and lead to improvements [32] as outlined in section 3.2. Many investigations were already undertaken with this plasma source, such as coupling with high pressure liquid chromatography (HPLC) [57], coupling with thermospray [58] and ETV [59], or in GC and SFC [60] and even in connection with time of flight mass spectrometry [61]. A review of the analytical MPT applications can be found in [42]. Also plasma diagnostic studies such as Thomson scattering [62] or the determination of rotational temperatures [63] were already performed as well as numerical simulations on certain aspects of the MPT operation [64]. Some of these are subject of chapter 3.

2. Fundamentals of Microwave Induced Plasmas

2.1. Characterisation of a plasma

A wide variety of macroscopically neutral substances containing many interacting free electrons and ionised atoms or molecules are called Plasmas [7]. Due to the long range Coulomb interaction they exhibit collective behaviour. But the term plasma is not assigned to all media containing charged particles and certain criteria like the electron density n_e, the electron and heavy particle temperatures T_e and T_h or energies and the density among others to be introduced below have to be satisfied. Figure 2.1 shows a variety of plasma phenomena for a large range of parameters. Many aspects of the plasmas that are of interest here are covered by the phenomena of electrical discharges in gases. The separation between plasma physics and gaseous discharges, an introduction can be found in [65], leads back to the fifties. While the first was mainly to serve the nuclear fusion and other "higher" research like MHD theory and kinetic methods the latter had emphasis on the dark and bright areas near the electrodes and the ramified and unpredictable structure of lightning, thus considered less as an exact science [66]. The situation changed considerably and since the seventies the field of high frequency discharges has been ever growing, driven mainly by applications in microelectronics [67]. To distinguish between discharges and plasmas became more and more artificial and nowadays the term plasma is assigned to both phenomena. However, some basic concepts originating from the theory of gas discharges are very suitable for a first approach to the plasma characterisation. These are discussed in the following paragraphs together with an estimation of their values for a typical MIP considered here.

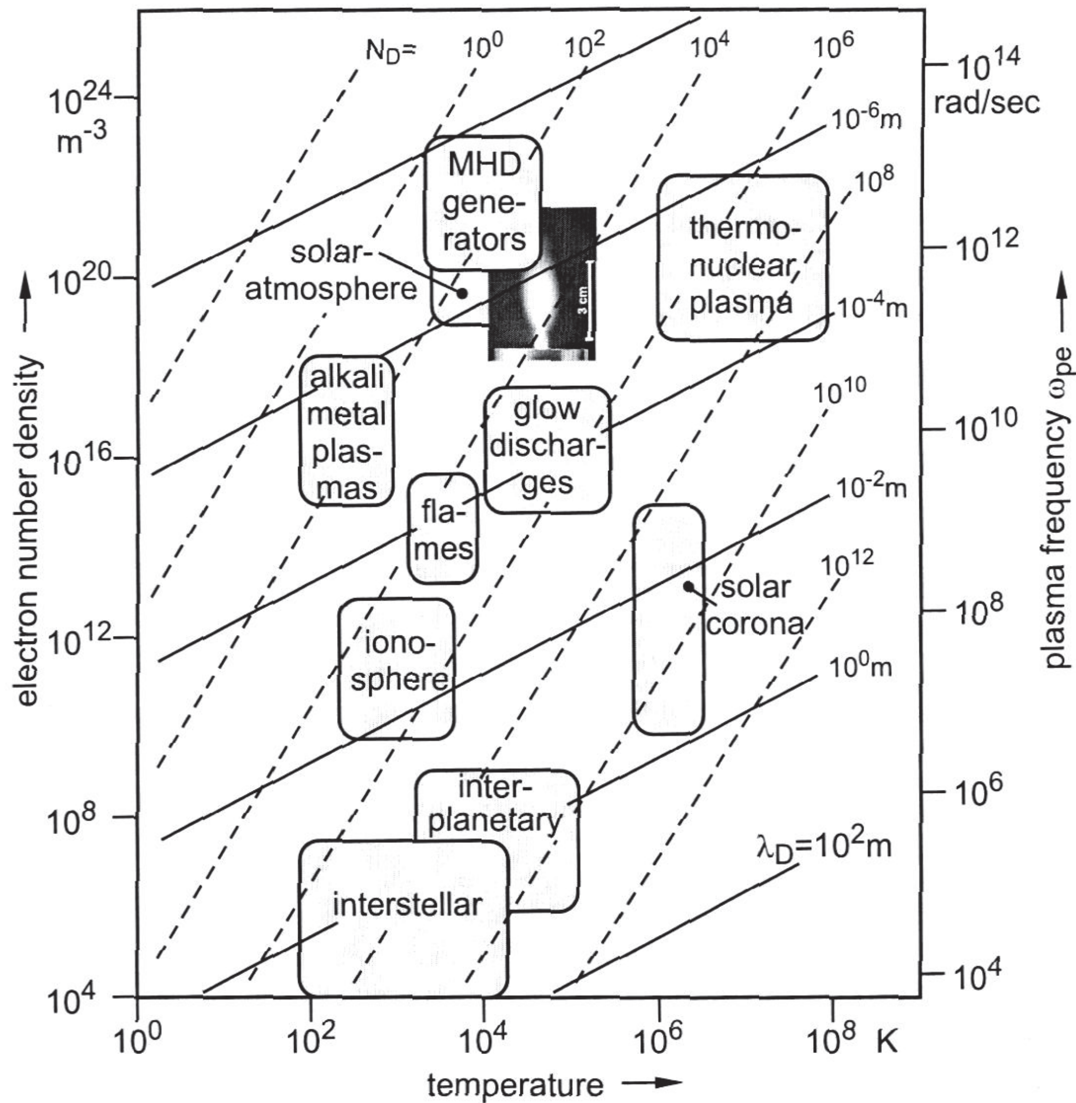

Figure 2.1.: Ranges of electron densities n_e and temperatures T_e for several plasma phenomena and their characteristic physical parameters as Debye length λ_D, plasma frequency ω_p and the number of electrons in a Debye sphere N_D. The photograph of an MPT plasma is shown as reference.

2.1.1. Macroscopic neutrality

In the absence of external forces a plasma is macroscopically neutral. Here, macroscopically means a length scale on which all variations of macroscopic parameters such as pressure and temperature are constant or vary slowly yet large enough to contain a sufficient number of particles to justify the introduction of macroscopic (average) quantities. A deviation from this neutrality, i.e. $n_e \simeq n_i$, would cause an enormous potential energy due to the large Coulomb forces compared to the kinetic

energy of the particles. If in a plasma with an electron density of $n_e = 10^{20}$ m^{-3} and the positive ion density would exceed this by 1% in a sphere of 10^{-3} m a plasma temperature of several millions of Kelvin would be necessary to balance the electric potential energy [7]. Therefore, this charge separation can only happen on a typical length scale on which the thermal particle energy is able to balance the electrostatic energy, called the "Debye length".
For the MIPs discussed here the typical temperatures are of the order of some eV and thus the macroscopic neutrality applies here.

2.1.2. Debye shielding

The Debye length is an important physical parameter in the characterisation of a plasma. It gives the order of magnitude within which an external perturbation can propagate into the plasma or the distance over which the field of a single particle is felt by other particles due to shielding effects of the neighbours. The calculation of the shielding distance was first performed by Debye for an electrolyte [7]. It can also be considered as a measure of the distance over which fluctuating electric potentials may appear. The expression

$$\lambda_D = \sqrt{\frac{\varepsilon_0 k_B T_e}{n_e e^2}} \tag{2.1}$$

for λ_D follows then by equating the elongation energy to the kinetic energy of a particle. A sphere inside the plasma of radius λ_D is called a "Debye sphere". It follows that each particle interacts only with particles inside its Debye sphere and that the interaction with particles outside can be neglected. The number of electrons inside a Debye sphere is given by

$$N_D = \frac{4}{3}\pi\lambda_D^3 n_e = \frac{4\pi}{3}\left(\frac{\varepsilon_0 k_B T}{n_e^{1/3} e^2}\right)^{3/2} \quad . \tag{2.2}$$

The Debye shielding effect is a characteristic of all plasmas and can thus be used as a criterion for the definition of a plasma as that if l is a typical length of the plasma, e.g. the diameter, it is required that

$$l \gg \lambda_D \quad . \tag{2.3}$$

For the MIPs with typical dimensions of some mm with $n_e \simeq 10^{20}$ m^{-3} and $k_b T_e \simeq$ 1.5 eV the Debye length is approximately $\lambda_D \simeq 1\,\mu$m and this criterion is definitely fulfilled.

Since the shielding is a collective effect, it follows that the number of electrons inside a Debye sphere has to be large enough, i.e.

$$n_e \lambda_D^3 \gg 1 \quad , \tag{2.4}$$

meaning that the average distance between electrons given by $n_e^{-1/3}$ must be small compared to λ_D. In case of the MIPs of interest here, $N_D \simeq 200$ may not be overwhelmingly large but still large enough to allow for collective shielding effects. Macroscopic neutrality, although implied by equation 2.3, is also required as a plasma criterion

$$n_e = \sum_s n_i^s \tag{2.5}$$

where n_i^s represents ion density of species s.

2.1.3. Plasma and collision frequency

The macroscopic neutrality may be disturbed by external forces. But as soon as these disappear the Coulomb attraction will tend to restore the neutrality causing an oscillation of the electrons around the equilibrium position due to their inertia. The frequency of this oscillation is given by

$$\omega_p = \sqrt{\frac{n_e e^2}{m_e \varepsilon_0}} \quad . \tag{2.6}$$

This oscillation is damped by collisions between electrons and heavy particles taking place with the collision frequency ν_{eh}. The fourth criterion for the existence of a plasma is therefore that the collision frequency has to be smaller than the plasma frequency

$$\omega_p > 2\pi\nu_{eh} \quad . \tag{2.7}$$

Otherwise the electrons will be forced by collisions to be in equilibrium with the heavy particles and the medium can be treated as a neutral gas. The MIPs considered here have a plasma frequency around $10^{12}\,s^{-1}$ being two orders of magnitude larger than the average collision frequency thus also fulfilling this criterion. Figure 2.1 shows the classification of a typical MIP in the large variety of plasma phenomena.

n_e	T_e	ω_p	λ_D
$\simeq 10^{20}$ m^{-3}	$\simeq 10^4$ K $\cong$ 1 eV	$\simeq 10^{12}$ s^{-1}	$\simeq 10^{-6}$ m

Table 2.1.: Characteristic parameter of a typical atmospheric pressure microwave induced plasma in argon.

2.2. Theoretical approaches

Bittencourt [7] states four different approaches for the description of plasma phenomena each applying to different circumstances with several choices of approximations. One is the "particle orbit theory" describing the motion of charged particles in given electromagnetic fields. Although not being a real plasma theory this approach has proven to be useful for very low density plasmas or cathode ray tubes. It is not applicable for the type of MIPs studied in this thesis.
Due to the very large number of particles in a plasma, like in a gas, statistical methods seem to be appropriate here. This is known as the "kinetic theory" just requiring the distribution function of the species under consideration for a prediction of macroscopic quantities. The problem consists in solving the kinetic equations governing the evolution of the distribution function in phase space. This can turn out to be rather tedious in general, but several approximations exist, and these will be used for the description of the MIPs studied here.
In case of high collision frequencies the plasma particles may be able to maintain a local equilibrium distribution and they may be treated as a fluid with local density, temperature and velocity. This theory is called "two-fluid" or "many-fluid theory". Its application to the atmospheric pressure MIPs is discussed controversially in the literature but may nevertheless be a reasonable approximation.
Finally, one may treat the plasma as a "single conducting fluid", the most popular simplified form known as "magnetohydrodynamic theory" (MHD) for very low frequency phenomena in highly conducting fluids immersed in magnetic fields. This is certainly not the case for the MIPs discussed here.

2.3. Microwave induced plasmas at atmospheric pressure

In kinetic theory all relevant information about the system under consideration are derived from the distribution function $f_s = f_s(\vec{r}, \vec{v}, t)$ defined such that

$$f_s(\mathbf{r}, \mathbf{v}, t)\,\mathrm{d}^3\mathbf{r}\,\mathrm{d}^3\mathbf{v} = \mathrm{d}^6 n_s(\mathbf{r}, \mathbf{v}, t) \tag{2.8}$$

gives the number $\mathrm{d}^6 n_s(\mathbf{r}, \mathbf{v}, t)$ of particles of species s in the differential volume element $\mathrm{d}^3\mathbf{r}\,\mathrm{d}^3\mathbf{v}$ of phase space. If no collisions between the particles and no radiation losses occur and particle creation and annihilation are unimportant, Liouville's states that the total time derivative of the distribution function is zero:

$$\frac{\mathrm{d}}{\mathrm{d}t} f_s := \frac{\partial}{\partial t} f_s + \mathbf{v}\nabla_r f_s + \dot{\mathbf{v}}\nabla_v f_s = 0 \quad . \tag{2.9}$$

This is known as the collisionless Boltzmann equation. If particle interactions have to be taken into account this equation will change to an inhomogeneous partial differential equation

$$\frac{\mathrm{d}}{\mathrm{d}t} f_s := \frac{\partial}{\partial t} f_s + \mathbf{v}\nabla_r f_s + \dot{\mathbf{v}}\nabla_v f_s = \left(\frac{\partial f_s}{\partial t}\right)_{coll} \tag{2.10}$$

know as the Boltzmann transport equation (BTE). Solving this equation is a forbidding task so that many approximations for the collision term exist. One of which is known as the "Relaxation Model" or "Krook Model" and can be written as

$$\left(\frac{\partial f_s}{\partial t}\right)_{coll} = \frac{(f_s - f_{s0})}{\tau} \tag{2.11}$$

where τ is a typical relaxation time in which a non-equilibrium distribution $f_s(\mathbf{r}, \mathbf{v}, t)$ reaches equilibrium $f_{s0}(\mathbf{r}, \mathbf{v}, t)$. More elaborated expressions are the Boltzmann collision integral and the Fokker-Planck collision term.

The average value of a quantity $q(\mathbf{r}, \mathbf{v}, t)$ with reference to the distribution function f_s can be obtained from

$$\langle q(\mathbf{r}, \mathbf{v}, t)\rangle_s := \frac{1}{n_s(\mathbf{r}, t)} \int q(\mathbf{r}, \mathbf{v}, t) f_s(\mathbf{r}, \mathbf{v}, t)\,\mathrm{d}^3 v \tag{2.12}$$

with the particle density $n_s(\mathbf{r}, t)$ defined as

$$n_s(\mathbf{r}, t) = \int f_s(\mathbf{r}, \mathbf{v}, t)\,\mathrm{d}^3 v \quad . \tag{2.13}$$

Thus the first four moments of the distribution function can be defined as

$$n_s(\mathbf{r},t) = \int f_s(\mathbf{r},\mathbf{v},t)\,\mathrm{d}^3v \qquad (2.14)$$

$$u_s^i(\mathbf{r},t) = \left\langle v^i(\mathbf{r},\mathbf{v},t)\right\rangle_s \qquad (2.15)$$

$$P_s^{i,j}(\mathbf{r},t) = \rho_s \left\langle v^i(\mathbf{r},\mathbf{v},t)v^j(\mathbf{r},\mathbf{v},t)\right\rangle_s \qquad (2.16)$$

$$E_s^{i,j,k}(\mathbf{r},t) = \rho_s \left\langle v^i(\mathbf{r},\mathbf{v},t)v^j(\mathbf{r},\mathbf{v},t)v^k(\mathbf{r},\mathbf{v},t)\right\rangle_s \qquad (2.17)$$

where we introduced the average velocity vector u_s^i, the average momentum flow $P_s^{i,j}(\mathbf{r},t)$ and the energy flow $E_s^{i,j,k}(\mathbf{r},t)$ tensors. This definitions can be extended straight forward to higher moments. But it is not necessary to solve the Boltzmann equation for the distribution function in order to calculate these macroscopic variables. Instead, these can be calculated from macroscopic transport equations obtained by taking the various moments of the Boltzmann equation. If $q(\mathbf{v})$ represents a physical property of the plasma particles which only depends on the particle velocity, the general transport equation will read as

$$\frac{\partial}{\partial t}(n_s \langle q\rangle_s) + (\nabla \cdot (n_s \langle q\mathbf{v}\rangle_s)) - n_s \langle(\dot{\mathbf{v}} \cdot \nabla_{\mathbf{v}})\, q\rangle_s = \int q \left(\frac{\partial f_s}{\partial t}\right)_{coll} \mathrm{d}^3v \quad . \qquad (2.18)$$

Substituting e.g. $q_s = m_s$ the mass of the species s for the general property q leads to the continuity equation

$$\frac{\partial}{\partial t}\rho_s + (\nabla \cdot (\rho_s \mathbf{u}_s)) = S_s \qquad (2.19)$$

where ρ_s is the mass density of species s and S_s an appropriate source term for particle creation and losses due to collisions, i.e. ionisation and recombination. In a similar manner equations involving the higher moments of the Boltzmann equation like the conservation of momentum and energy can be obtained but always with an excess of new variables since every new equation introduces new unknowns. Thus one ends up with an incomplete set of equations and therefore has to truncate the series at a certain point. Taking just the first two moments, i.e. the equations of conservation of mass and momentum leads to the so called cold plasma model. Encompassing also the conservation of energy is known as the warm plasma model. Benoy [12] describes a warm plasma model for the ICP which he solves numerically. In the most general case when higher moments are required it is simpler to directly work with the distribution functions as outlined above [7].

2.3.1. Balances and Equilibrium

The equilibrium distribution functions are the time-independent solutions of the Boltzmann equation 2.9 in the absence of external forces. The principle of detailed

balance of statistical mechanics stating that under equilibrium the effect of each type of collision is exactly compensated by the inverse collision can be used to derive the corresponding distribution functions as outlined in [68].

equilibrium	process	conservation equation
Maxwell (2.20)	elastic collisions $S_1 + S_2 \rightleftharpoons S_1 + S_2$	$p_1 + p_2 = p'_1 + p'_2$ $\frac{p_1^2}{2m_1} + \frac{p_2^2}{2m_2} = \frac{p_1'^2}{2m_1} + \frac{p_2'^2}{2m_2}$
Boltzmann	excitation and de-excitation $S + A_r \rightleftharpoons S + A_q$	$p_S + p_A = p'_S + p'_A$ $\frac{p_S^2}{2m_S} + \frac{p_A^2}{2m_A} + E_r = \frac{p_S'^2}{2m_S} + \frac{p_A'^2}{2m_A} + E_q$
Saha (2.22)	ionisation and recombination $S + A_r \rightleftharpoons S + A_q^+ + e$	$p_S + p_A = p'_S + p'_A + p_e$ $\frac{p_S^2}{2m_S} + \frac{p_A^2}{2m_A} + E_r = \frac{p_S'^2}{2m_S} + \frac{p_A'^2}{2m_A} + E_{q^+} + \frac{p_e^2}{2m_e}$
Planck	absorption and emission $A_r\ (+\,h\nu) \rightleftharpoons A_q + h\nu\ (+\,h\nu)$	$p_A = p'_A + \frac{h\nu}{c}$ $\frac{p_A^2}{2m_A} + E_r = \frac{p_A'^2}{2m_A} + E_q + h\nu$

Table 2.2.: Proper balances: the momentum of the interacting particles prior to the collision are denoted with p and afterwards with p′. Particles symbolised with S do not suffer a change of internal energy, e.g. electrons or atoms after elastic collisions. For the Saha balance E_{q^+} includes the ionisation energy E_{ion}.

Table 2.2 resumes the most important balances in plasmas. Here, only the Maxwell-Boltzmann distribution and the Saha equation are presented, see [68] for a detailed discussion. The Maxwell-Boltzmann distribution

$$f_s(E)\,\mathrm{d}E = \frac{2\pi n_s}{(\pi k_B T_s)^{3/2}} \sqrt{E}\,\mathrm{e}^{-\frac{E}{k_B T_s}}\,\mathrm{d}E \tag{2.20}$$

is defined such that $f_s(E)\,\mathrm{d}E$ is the number of particles of species s per unit volume having kinetic energy between E and $E + \mathrm{d}E$. Figure 2.2 shows the normalised, i.e. divided by the density n_e, electron energy distribution function (EEDF) of an MPT plasma under the assumption of a Maxwellian distribution for several electron temperatures. Only a very small fraction of the electrons have sufficient energy for a direct ionisation of e.g. argon ($\simeq 15.6\,\mathrm{eV}$ first ionisation energy).

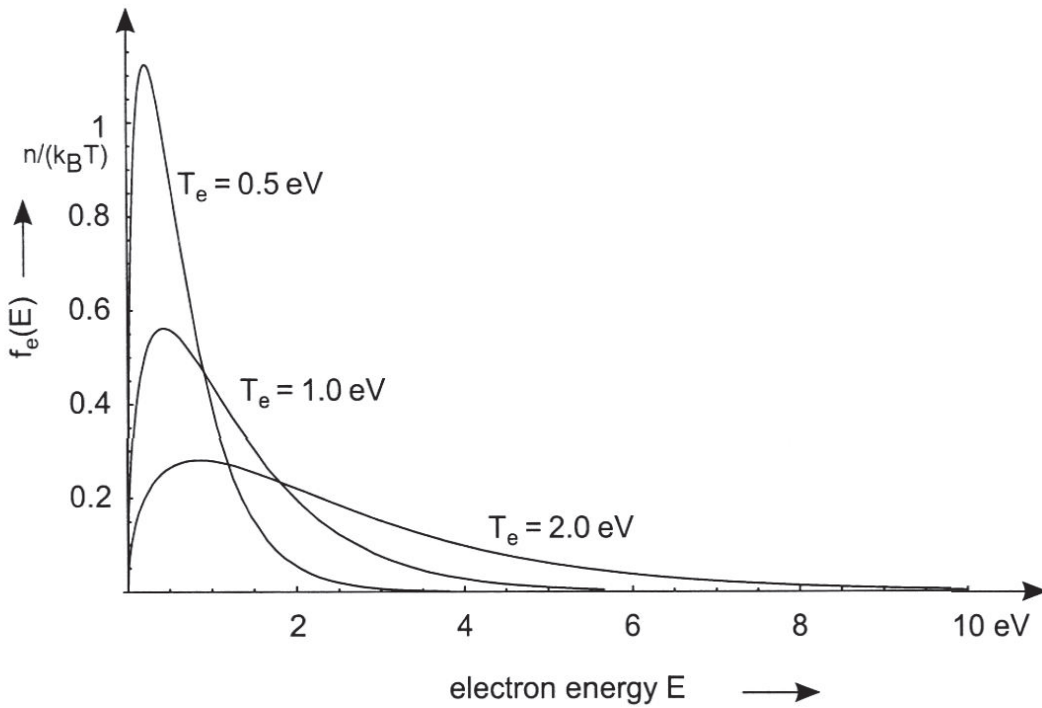

Figure 2.2.: Electron energy distribution (EEDF) for a Maxwellian electron gas at electron temperatures of 5000 K , 10000 K *and* 20000 K . *The higher the electron temperature the flatter and broader is the distribution function.*

The Saha distribution is generated by inelastic collisions involving an equilibrium of ionisation and recombination processes. The high degeneracy of the ionised state, the phase space volume of the free electron is $h^{3N}N!$ and thus the relation of the statistical weights of ionised g_i and ground state g_1

$$\frac{g_i}{g_1} = \frac{(2\pi m_e k_B T_e)^{3/2}}{h^3 n_i} \tag{2.21}$$

allows for a non-vanishing degree of ionisation at temperatures well below the ionisation energy. From the Boltzmann distribution it follows for the Saha distribution

$$\frac{n_i}{n_1} = \frac{(2\pi m_e k_B T_e)^{3/2}}{h^3 n_i} \, \mathrm{e}^{-\frac{E_{ion}}{k_B T_e}} \quad . \tag{2.22}$$

Together with the ideal gas law it follows that

$$(\frac{n_i}{n_1})^2 = \frac{(2\pi m_e k_B T_e)^{3/2} (k_B T_h)^{3/2}}{h^3 p} \, \mathrm{e}^{-\frac{E_{ion}}{k_B T_e}} \quad . \tag{2.23}$$

with the pressure p and Planck's constant h. This directly allows the calculation of the degree of ionisation $\alpha := \frac{n_i}{n_i+n_1}$. Figure 2.3 shows α for a typical MPT plasma as a function of the electron temperature. Thus in an atmospheric pressure argon plasma with an electron temperature of 1.5 eV the ionisation degree in Saha equilibrium is $\alpha \simeq 0.253$. This has to be contrasted to the experimental value of $\alpha \simeq 10^{-4}$ under the assumption that $n_i \simeq n_e$, see section 3.3 for experimental values of n_e, which clearly shows that the MPT plasma is not in Saha equilibrium. In fact, the ground state is overpopulated in comparison to the Saha equilibrium with falling tendency for the higher levels. Therefore, one denotes this as the partial local Saha equilibrium for the higher levels (pLSE) [68].

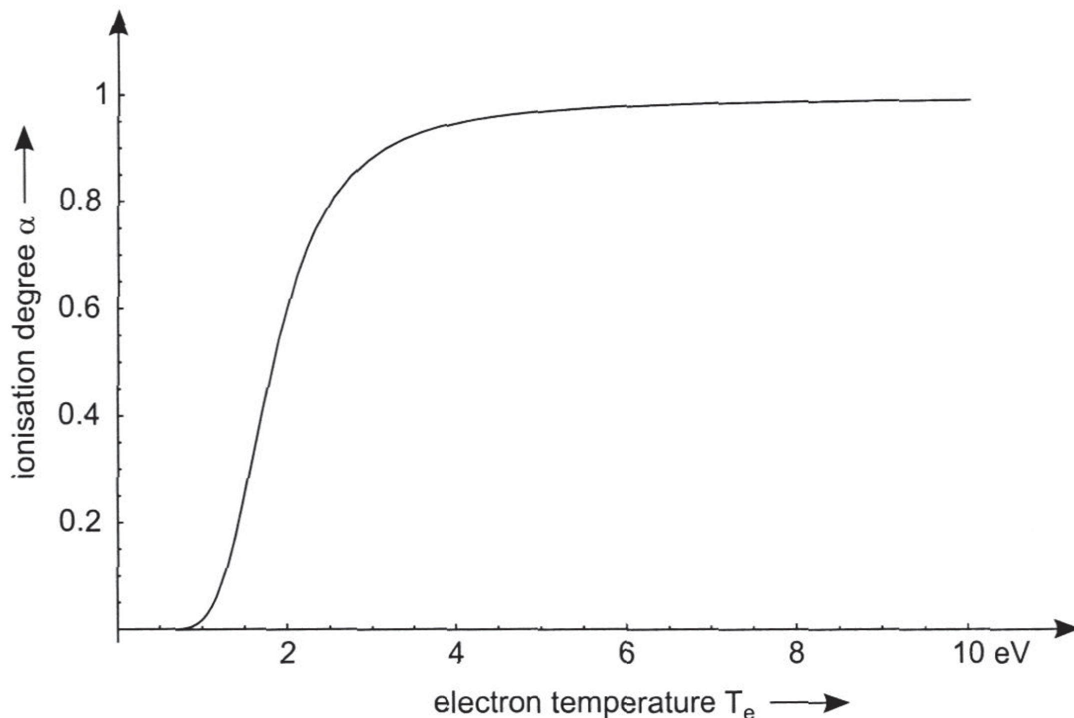

Figure 2.3.: Ionisation degree α_{Ar} for argon with an ionisation energy of $E_{ion} \simeq$ 15.6 eV as a function of the electron temperature.

2.3.2. AC conductivity and dielectric model

If for a weakly ionised cold plasma the collision term in the macroscopic equation of motion for the average electron is replaced by the empirical expression $\mathbf{F}_{coll} =$

$-\nu_{eh} m_e \mathbf{u}_e$ one arrives at the so called Langevin equation of motion

$$m_e \frac{\mathrm{d}}{\mathrm{d}t}\mathbf{u}_e = -e\mathbf{E} - \nu_{eh} m_e \mathbf{u}_e \tag{2.24}$$

in the absence of a magnetic field. For situations in which $|\mathbf{u}_e \times \mathbf{B}| \ll |\mathbf{E}|$, for plane waves this means $|\mathbf{u}_e| \ll |\omega/\mathbf{k}|$, the situation greatly simplifies in that a linearisation can be carried out and the Langevin equation for time harmonic fields reads as

$$e\underline{\mathbf{E}} = -m_e(\nu_{eh} - j\omega)\underline{\mathbf{u}}_\mathbf{e} \quad . \tag{2.25}$$

From this expression one readily identifies the conductivity under the assumption of the validity of Ohm law [1]

$$\sigma = \frac{n_e e^2}{m_e(\nu_{eh} + j\omega)} \quad . \tag{2.26}$$

Considering Maxwell's equation for time harmonic fields

$$\nabla \times \underline{\mathbf{B}} = \mu_0(\underline{\mathbf{J}} + \mathrm{j}\varepsilon_0\omega\underline{\mathbf{E}}) = \mu_0(\sigma + \mathrm{j}\varepsilon_0\omega)\underline{\mathbf{E}} \tag{2.27}$$

which shows that one can define the plasma permittivity

$$\underline{\varepsilon}_{pl} := 1 - \mathrm{j}\frac{\sigma}{\omega\varepsilon_0} = 1 - \left(\frac{\omega_p}{\omega}\right)^2 \frac{\omega}{\omega - \mathrm{j}\nu} \quad . \tag{2.28}$$

In fact, this will be the only quantity of the plasma involved in the electromagnetic simulations of the plasma sources. It involves the electron density n_e and the effective electron heavy particle collision frequency ν_{eh} the determination of which is still all but a simple task depending on the approximations and simplifications to be carried out for an adequate description. This is beyond the scope of this thesis nevertheless the only way to proceed for a full modelling except for some semi-empirical approaches basing on fits of experimental data (see chapter 3).

2.3.3. Ambipolar diffusion

Inhomogeneities in the electron density distribution cause a diffusion in the opposite direction of the density gradients. An analogous effect takes place for the ions following the common free diffusion law

$$\mathbf{\Gamma}_{e,i} = -D_{e,i}\nabla n_{e,i} := \frac{k_B T}{m_e \nu_{eh}}\nabla n_{e,i} \quad . \tag{2.29}$$

[1] For the general case the generalised Ohm's law [7] has to be applied but for steady state plasmas and under the assumption of vanishing electron pressure (no point but this could be questioned for the MPT plasma) and $\omega_p^i \ll \nu_{eh}$ this reduces to the Ohm's law in its well known form.

Since the free diffusion coefficient D is inversely proportional to the mass, the electrons diffuse much faster than the ions leaving an excess of positive charge behind. This in turn gives rise to a space charge field accelerating the ions and slowing down the electrons in such a way that both species move at the same intermediate velocity. This effect is called ambipolar diffusion, which under the assumption $n \simeq n_e \simeq n_i$, follows the relation

$$\frac{\partial}{\partial t} n = D_a \nabla^2 n \tag{2.30}$$

with the ambipolar diffusion coefficient

$$D_a = k_B \frac{T_e + T_i}{m_e \nu_{eh} + m_i \nu_{ei}} \quad . \tag{2.31}$$

Note that this diffusion is proportional to the square of the density gradient in contrast to the free diffusion. A simple estimation of orders of magnitude shows that if l denotes a typical length scale over which the electron density varies significantly the ambipolar diffusion can be neglected if

$$l^2 \ll \lambda_D \quad . \tag{2.32}$$

This condition is rarely satisfied as the Debye length is rather small in general, and it is also not fulfilled for the MIPs studied here.
Using the approximation

$$D_a = D_i \left(1 + \frac{T_e}{T_h}\right) \tag{2.33}$$

for D_a and the first Chapman-Enskog approximation [69, 70] for D_i

$$D_i = \frac{3 k_B^2 T_h^2}{8 p m_h \Omega(T_h)} \tag{2.34}$$

where $\Omega(T_h)$ is the ion-atom collision integral [33] leads to the numerical value of

$$D_a \approx 0.05 \text{ m}^2 s^{-1} \tag{2.35}$$

for the MPT plasma, with $T_e = 1.5\,\text{eV}$ and $T_h = 0.5\,\text{eV}$ respectively.

In summary, it follows that MIPs such as those generated by the MPT cannot be treated with magnetohydrodynamic methods. They are far from thermodynamic equilibrium and even an equilibrium within a single species as e.g. the electrons is not maintained rigorously. Although this can be assumed locally as a good approximation due to the high collision frequency. Energy in-coupling takes exclusively

place via the electrons, the ions are much to slow to follow the high excitation frequency of the microwave field. Ambipolar diffusion has to be considered here due to the small Debye length. A kinetic treatment could be carried out within the warm plasma model as it has been done for the ICP [12]. However, the steep gradients occurring for these kind of plasmas significantly complicate the situation and solutions for the macroscopic transport phenomena are difficult to obtain.

3. Coaxial Microwave Plasma Sources

3.1. Introduction

The advantages of non-resonant MIP sources in comparison to resonant designs for usage in spectrochemical analysis, at least for the investigation of wet aerosols, were pointed out in chapter 1 of this thesis. One of the simplest approach is their construction out of coaxial waveguide components (MPT, TPS) or a combination of coaxial and hollow waveguides(TIA). The latter are useful in the case of higher microwave powers exceeding several 100 W .
Some commonly used devices were introduced briefly in chapter 1 together with their advantages and drawbacks for certain applications. Here the focus will be on a special coaxial microwave induced plasma source (MIP) which turned out to be ideally suited for lower power applications in OES, the so-called "Microwave Plasma Torch" (MPT, the name stems from the torch like shape of the plasma). Apart from its construction and operational principles, diagnostic measurements at the MPT generated plasma and different simulations will be presented. They lead to an advanced understanding of this plasma source and the principles of non-resonant MIPs in general.

Most parts of this chapter have been published in [32, 64, 62]

3.2. The modified Microwave Plasma Torch (MPT)

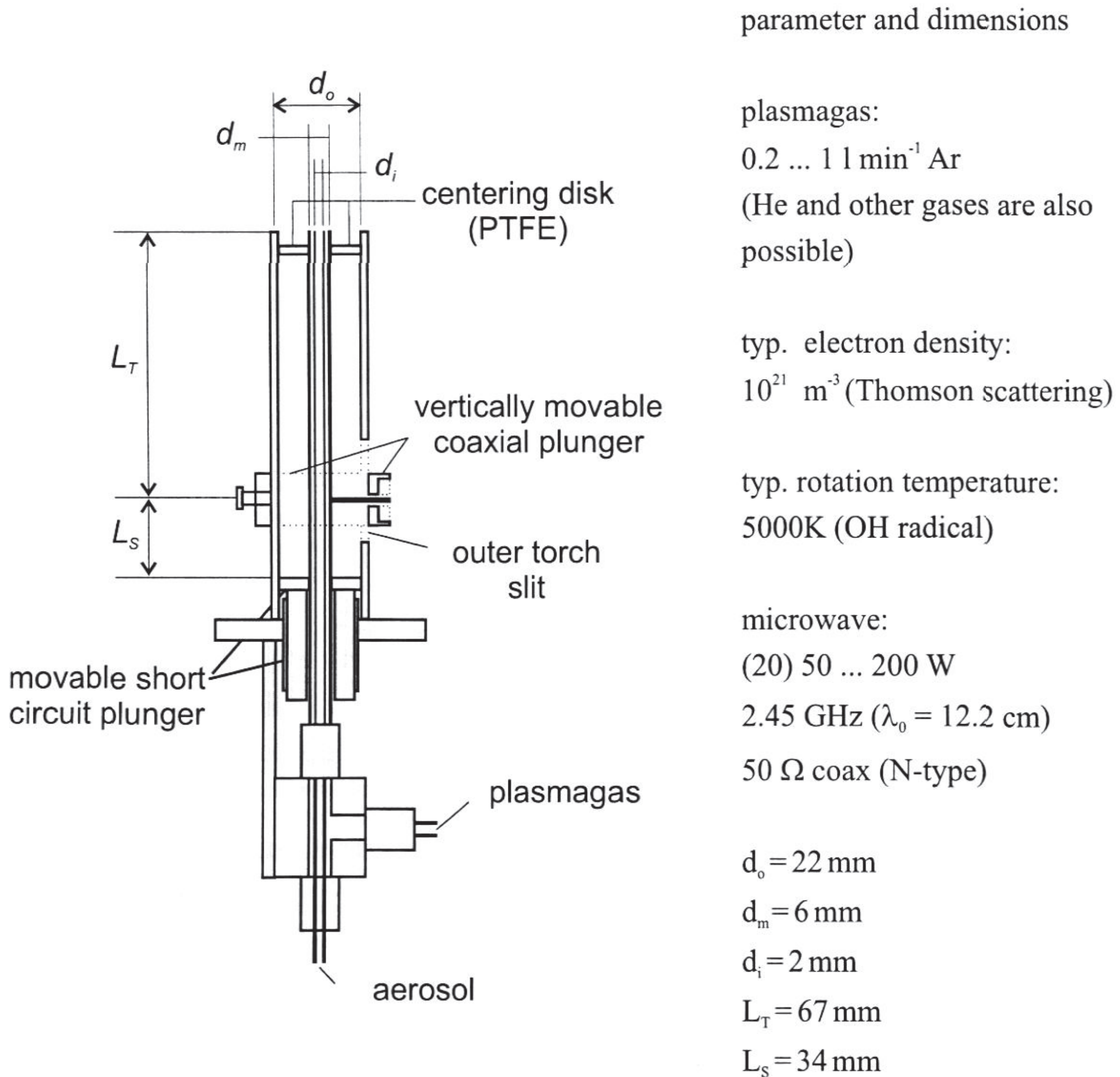

Figure 3.1.: The modified MPT setup. Some characteristic dimensions and typical parameters are given aside the drawing. Dimensions are given for a tuned fixed setup without movable parts.

The "Microwave Plasma Torch" (MPT) as developed by Jin et al.[6] contains several critical elements, the movable antenna ring turns out to be difficult to adjust in everyday usage and the tuning by a movable short circuit is another source of

difficulties in operation, in particular as a result of often improper ohmic contacts. Therefore, it was obvious to modify this setup in order to optimise for stability, low power consumption and easy construction with as little requirements to time and material resources as possible [32]. As it is often the case, the modifications lead to a better understanding of the device and vice versa, as will be clear in the following sections. First, we describe the modified setup as presented in figure 3.1 from the high frequency engineering point of view, which also exhibits already a way of looking at its functionality. The MPT used mainly consists of a short-circuited coaxial line with a radially attached N-type connector for the attachment of a coaxial 50 Ω power input cable as well as connections for entering the working gas, which in our case is always Ar unless stated otherwise, and the analyte aerosol. This coaxial section consists of three concentric tubes, the outermost two of which constitute the coaxial wave-guiding conductors. The inner is of almost no importance for the electromagnetic characteristics but used for a separate aerosol introduction (actually a mixture of aerosol and Ar). The plasma gas is introduced between the inner and the intermediate tube.

Since a capacitive coupling of the input line with an antenna ring around the inner conductor (intermediate tube), see chapter 1, of the MPT proved to be unstable, it was replaced by a galvanic coupling with a mechanically soft metal interface. Numerical eigenvalue calculations show, that in this case the in-coupling has to be moved to the second 50 Ω point approximately $\lambda_0/2$ off the MPT ending downwards the coaxial section. This is due to the fringe fields occurring at the symmetry-breaking in-coupling; these vanish approximately after a length equal the diameter of the coaxial line. The inner conductor of the main coaxial section is centred with the aid of a PTFE spacer. This proved to be essential for obtaining a cylindrical symmetric electromagnetic field, which in turn partially accounts for the stability of this plasma source. It is also possible to completely fill the field propagation volume of the MPT with a low loss dielectric as PTFE. Besides the mechanical stabilisation this also allows for smaller set-ups as the wavelength λ_0 reduces with increasing permittivity ε_r and thus shortens transformation lengths. Such a modified MPT found application in a work about "Direct solid atomic emission spectrometric analysis of metal samples by an Ar microwave plasma torch coupled to spark ablation" [71].

3.2.1. MPT as an impedance matching network

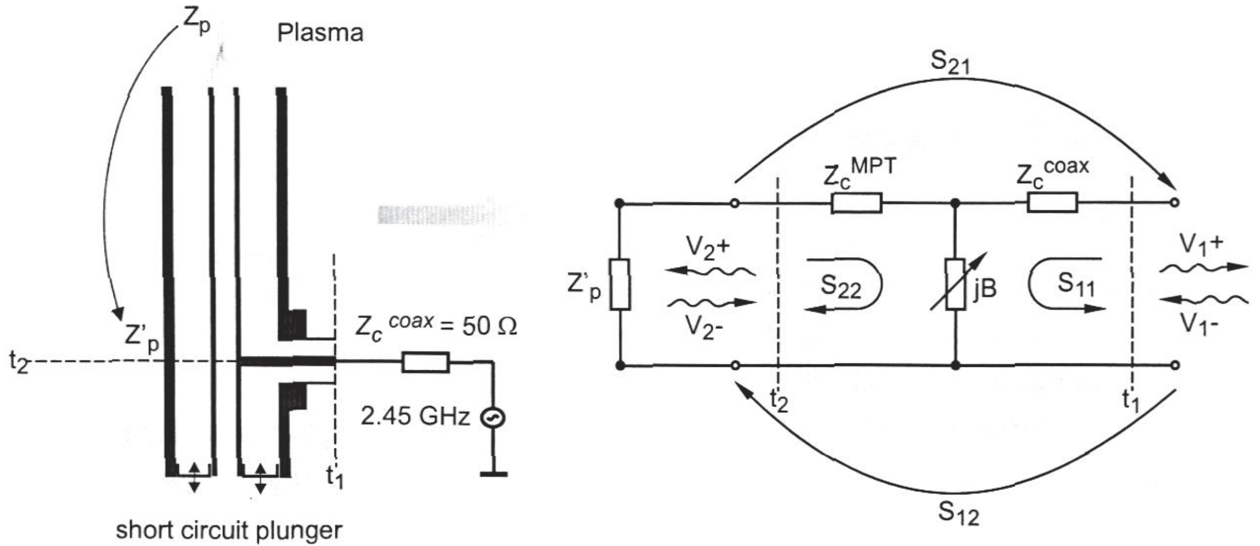

Figure 3.2.: Equivalent circuit diagram of the MPT for the description as an impedance transformer. Definition of the amplitude scattering matrix **S**.

Due to its historical development from the Surfatron (see chapter 1), the MPT was considered as a resonance structure. This description seems to be inappropriate, at least in the case of an ignited plasma, since the respective quality factor would be very small, i.e. the half-width of the resonance curve would be extremely broad. Therefore, a description in terms of an impedance transformer which matches the plasma impedance to the wave impedance of the feeding coaxial line seems more suitable here. An excellent introduction to transmission line analysis can be found in [72]. However, the MPT without an ignited plasma behaves like a $^3/_4\,\lambda$-resonator with more or less well defined resonances as numerical Finite Difference Time Domain calculations show. The broadening of the resonance peaks is due to the non-ideal open end of the MPT which radiates a small amount of microwave energy into the surrounding.

The impedance transformation properties of the MPT are analysed by a two-port equivalent circuit given in figure 3.2. The definition of the scattering matrix and its calculation will be addressed to later when dealing with the numerical electro-

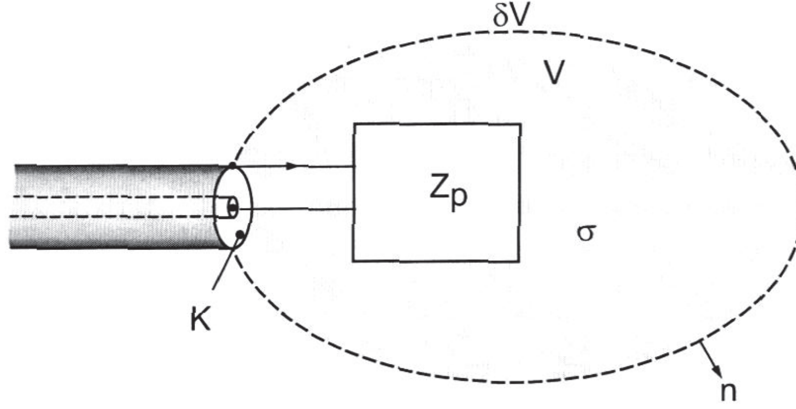

Figure 3.3.: Graphical representation of Poynting's theorem for the expression of a conductivity distribution as a complex impedance with reference to a waveguide opening.

magnetic simulation of the MPT. We will now quickly step through the circuit and discuss the constituent elements. The impedance $\underline{Z}_p'$ is the transformed effective plasma impedance $\underline{Z}_p$ which can be defined for time harmonic fields with the aid of Poynting's theorem

$$\underline{Z}_p = \frac{1}{|I|^2}(P_A + 4j\omega \int_V (w_e - w_m)\, \mathrm{d}^3r + \oint_{\partial V - K} \underline{\mathbf{S}} \cdot \mathbf{n}\, \mathrm{d}\mathbf{a}) \tag{3.1}$$

It expresses a conductivity distribution $\sigma(\mathbf{r})$ in volume V as a complex impedance $\underline{Z}_p$ with reference to a waveguide opening K in terms of electromagnetic fields $\underline{\mathbf{E}}$ and $\underline{\mathbf{H}}$ as well as their energy densities w_e, w_m and P_A and the Poynting vector $\underline{\mathbf{S}} = {}^1\!/_2\, \underline{\mathbf{E}} \times \underline{\mathbf{H}}$, see figure 3.3 for a graphical representation. The electric and magnetic field energy densities and the dissipated power are given by

$$w_e = \frac{1}{4}\varepsilon_0 \varepsilon_r \left|\underline{\mathbf{E}}\right|^2 \tag{3.2}$$

$$w_m = \frac{1}{4}\mu_0 \left|\underline{\mathbf{H}}\right|^2 \tag{3.3}$$

$$P_A = \int_V \sigma \left|\underline{\mathbf{E}}\right|^2 \mathrm{d}^3 r\,, \tag{3.4}$$

respectively and the equivalent current is the line integral along the surface of the inner or outer conductor of the (coaxial) waveguide

$$\underline{I} = \oint \underline{\mathbf{H}}\, \mathrm{d}s\,. \tag{3.5}$$

This complex plasma impedance $\underline{Z}_p$ is transformed along L_T (see figure 3.2) yielding an admittance $\underline{Y}_p' = {}^1\!/_{\underline{Z}_p'}$ of

$$\underline{Y}_p' = Y_c^{MPT} \frac{\underline{Y}_p + jY_c^{MPT} \tan \beta L_T}{Y_c^{MPT} + j\underline{Y}_p \tan \beta L_T} . \tag{3.6}$$

Here, we introduced the propagation constant $\beta_0 = {}^{2\pi}/_{\lambda_0}$ for a TEM wave with free space wavelength λ_0 ($\simeq 0.12\,m$ at $2.45\,GHz$) and the characteristic wave impedance of the MPT

$$Z_c^{MPT} = \frac{1}{Y_c^{MPT}} = \frac{1}{2\pi}\sqrt{\frac{\mu_0}{\varepsilon_0\varepsilon_r}} \ln \frac{R_O}{R_I} \simeq 60\ \Omega\ \ln \frac{R_O}{R_I} , \tag{3.7}$$

which is only a function of the setup dimension and propagation space permittivity (air, in general). The standard MPT used here with dimensions given in figure 3.1 has a characteristic impedance of approximately 78 Ω. The short circuit is transformed along the coaxial line of length L_S into an admittance jB given by

$$jB = -jY_c^{MPT} \cot \beta L_S . \tag{3.8}$$

The parallel connection of jB and $\underline{Y}_p'$ and the capacitive fringe field C_f with a frequency ν dependent conductance of $j2\pi\nu C_f$ must yield an input impedance Z_c^{coax} equal to the $50\,\Omega$ connector impedance at the coupling point (reference plane t1 in figure 3.2). Note that the effect of the fringe field is included in the short circuit reactance in terms of a short circuit length correction δL_S. This condition can be satisfied by proper choices of the lengths L_T and L_S. By these two degrees of freedom only it is possible to match virtually any plasma impedance since the length L_T can always be chosen such that the real part of the transformed plasma impedance $Re[\underline{Z}_p']$ equals the connector wave impedance and the imaginary part $Im[\underline{Z}_p']$ can be compensated for by the transformed short reactance $jX = {}^{1}/_{\text{jB}}$. One should note that the quality factor of this impedance transformation is rather low because of a high resistive part of $\underline{Z}_p$; experimentally, $Re[\underline{Z}_p] \simeq Z_c^{MPT}$ is observed, see following section. This results in the fact that the arrangement is basically non-resonant.

3.2.2. Experimental estimation of the effective plasma impedance

It is possible to determine the effective plasma impedance within the framework of an equivalent circuit model by measuring the absolute value of the reflection factor, only

$$|\underline{\Gamma}| = \left| \frac{\underline{Z}_L - Z_c^{coax}}{\underline{Z}_L + Z_c^{coax}} \right| = \left| \frac{Y_c^{coax} - \underline{Y}_L}{Y_c^{coax} + \underline{Y}_L} \right| , \tag{3.9}$$

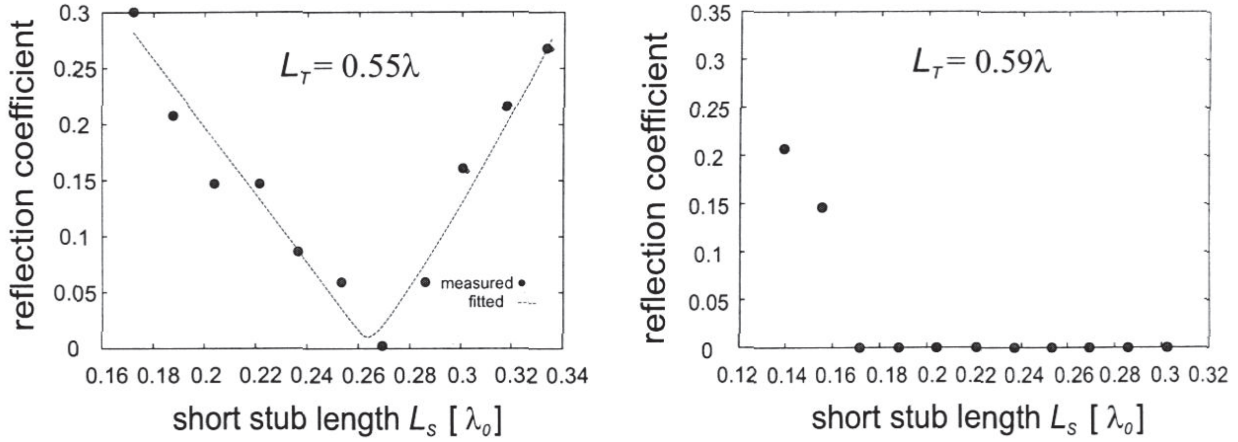

Figure 3.4.: Reflexion coefficient as a function of short stub length L_S for different in-coupling positions L_T in terms of the free space wavelength λ_0. The fitting procedure yields the normalised complex plasma impedance $z_p = 0.87 + j\,0.19$. The right diagram shows matching conditions; here the short stub length is variable in a broad range thus suggesting a fixed setup without necessity for tuning elements.

where $\underline{Z}_L$ represents the load impedance given by the equivalent circuit, i.e. the effective in-coupling impedance at reference plane t_1 in figure 3.2, for different values of L_T and L_S and fit the data to the equivalent circuit. These measurements were made with a simple setup including an MPT with a movable short circuit plunger and a slotted main coaxial section in order to adjust the coupling position, i.e. L_T, and two directional couplers for measuring the forward and reflected power in a range from 20 W to 200 W at Ar gas flows of 700 mL min^{-1} in the intermediate channel (working gas) and (250 mL min^{-1}) in the central channel (aerosol channel). The effective plasma impedance can then be determined by choosing it as the fit parameter in the equivalent circuit model. In addition, a correction for the short circuit length has to be taken into account due to the fringe field effects at the coupling position. This turns out to shift the real short circuit length towards smaller values. This tendency is confirmed by electromagnetic field simulations. Due to the non-linearity of the regression function, standard methods are unsuitable here. Instead, a non-linear "least-squares" fit employing the Levenberg-Marquardt [73] algorithm was carried out. A typical example of such a fit is given in figure 3.4. The resistive part of the fitted normalised plasma impedance, i.e. the plasma impedance with respect to the wave impedance of the main coaxial section of the MPT $Re[\underline{z}_p' = \underline{Z}_p'/Z_c^{MPT}]$, is of the order of unity. The reactive part is considerably smaller, $Im[\underline{Z}_p'] \simeq Z_c^{MPT}/10$.

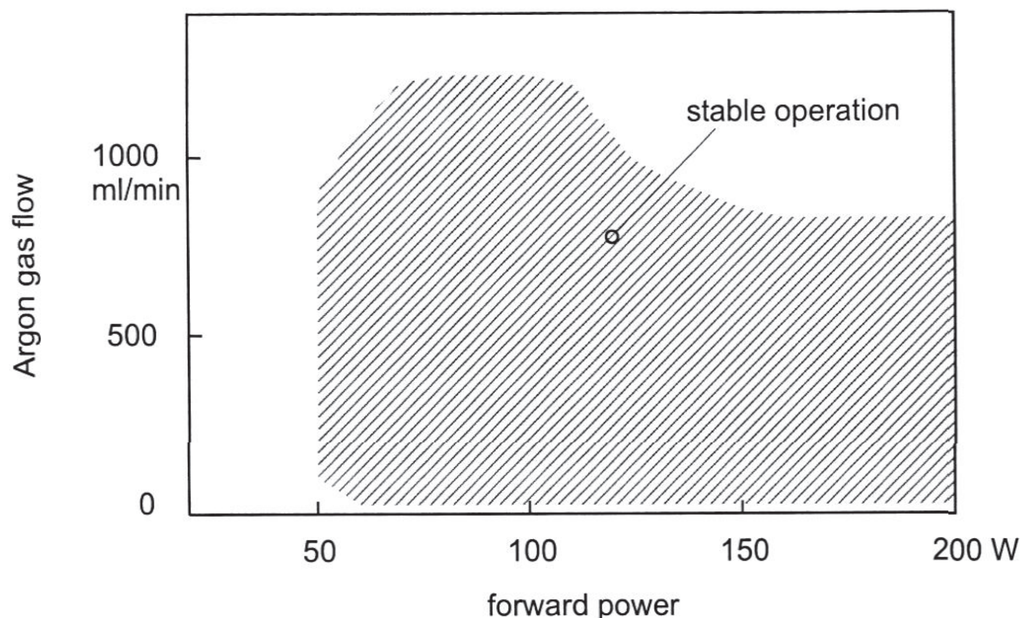

Figure 3.5.: Region for stable plasma operation in the case of the modified MPT. The Ar *gas flow in the analyte channel is fixed to* 250 $\mathrm{mL\,min^{-1}}$.

The existence of a flat plateau in the curve representing the reflection coefficient as a function of short circuit length for a specific in-coupling position L_T, see figure 3.4, indicates that the reactive part is by far less important to match as compared to the resistive one. Indeed, the plasma adjusts its reactance in a certain range in order to absorb maximum power. This directly leads to the possibility of a fixed setup without movable parts as proposed in [32]. Once adjusted to low reflections, the MPT works relatively stable for power variations. Figure 3.5 shows the power and gas-flow range for stable plasma operation for such an optimised set-up. Note that a plasma can also be obtained with parameters others than the ones given in figure 3.5, but the type of plasma preferred in Atomic Spectrometry is limited to the shown parameter range.

3.3. Thomson scattering measurements of the electron density and temperature

To gain further information about the plasma except the effective plasma impedance which only makes sense within the framework of an equivalent circuit, sophisticated plasma diagnostic measurements are required. This is a broad and complex subject of continuous research, especially in the case of (microwave induced) atmospheric

pressure plasmas. A comparative overview can be found e.g. in [25], an introduction to plasma spectroscopy can be found in [74]. Major parameters to characterise a plasma are its electron density and temperature. Concerning their measurement, numerous papers have been published on the inductively coupled plasma (ICP) but relatively few deal with microwave plasmas. Electron number densities in capacitively coupled microwave plasma (CMP) [36], the "Torche à Injection Axiale" (TIA) [1] and the Surfatron [48] have been determined from the ration of atom and ion lines [40] as well as from Stark broadening of the H_β or H_α line [75, 76, 77]. In the case of the latter papers, however, no spatial distributions of electron number densities were reported. Kitagawa et al. [78] determined excitation temperatures in the CMP from the intensity ration of two atomic lines and this was similarly done for the Surfatron [77], the MPT [79] and the TIA [76]. However, this method makes use of the assumption of a Boltzmann distribution. In a recent paper it was shown that at least for the TIA this assumption does not apply [35]. Without need for assumptions on the existence of LTE, electron number densities and electron temperatures can be determined by Thomson scattering, which already has been proven to be a very powerful tool for plasma diagnostics [80, 81, 82, 83]. With this method mappings of plasma parameter also can be made without need for Abel inversion, as it was shown for the ICP [84, 85, 86]. Thomson scattering measurements also have already been performed for the MPT [81] and the TIA [35]. However, up to now only some lateral and axial scans of electron number densities and electron temperatures have been carried out [87].

In this section mappings of electron densities and electron temperatures for the plasma obtained from a modified MPT [32] are presented. The influences of the gas flow rates, the power and water introduction on the electron temperature and density are described. The results are compared with those obtained for other microwave plasmas and for the ICP. In oder to further illustrate the influence of the gas flow and the water introduction on the plasma obtained from the MPT digitally recorded photographic images of the plasma under different working conditions are used. Since the experimental set-up used is not of major interest here, just a brief description will be given below. A detailed description can be found in [86]. For completeness a short theoretical introduction to Thomson scattering will be given prior to presenting the measurement results.

3.3.1. Principle of Thomson scattering and experimental set-up

Thomson scattering is the scattering of photons on free electrons [88]. An outline of the theory can be found in [89] and some modifications to consider also not purely Gaussian shapes of the signal are given in [90]. Thomson scattering was considered a diagnostic tool in fusion plasma research [91] but found its way into the laboratories of so called technical plasma applications.

In the classical approximation, no frequency shift of the scattered photons occurs if the electron is at rest. Otherwise, the scattered light will be Doppler-shifted [91]. The cross section can be derived classically or from Quantumelectrodynamics (QED) and leads to respectively different formulas. In QED the differential cross section in know as the "Klein-Nishina-Formula" for Compton scattering (see [92] for derivation)

$$\frac{\mathrm{d}\sigma_{Th}}{\mathrm{d}\Omega} = \frac{\alpha^2}{4m_e^2}(\frac{k'}{k})^2(\frac{k'}{k} + \frac{k}{k'} + 4(\varepsilon \cdot \varepsilon')^2 - 2) \tag{3.10}$$

in units of $\hbar = c = 1$ with k and k' denoting the incident and scattered photon wave vector respectively. In the non-relativistic limit and neglecting quantum mechanical effects, this reduces to

$$\frac{\mathrm{d}\sigma_{Th}}{\mathrm{d}\Omega} = \frac{\alpha^2}{4m_e^2}\left(\varepsilon_0 \cdot \varepsilon_s\right)^2 \tag{3.11}$$

with the polarisation vectors ε_0 and ε_s of the incident and scattered photon, respectively and the fine structure constant $\alpha \simeq {}^1\!/_{137}$[1]. The overall polarisation independent cross section in the MKSA system is given by

$$\sigma_{Th} = \frac{2}{3}\alpha^2(4\pi R_e^2) \tag{3.12}$$

where R_e is the Compton wavelength of the electron

$$R_e = \frac{\hbar}{m_e c}\ . \tag{3.13}$$

Substituting the respective numerical values of the physical constants shows that its value $\simeq 10^{-28}$ m^2 is rather small. This is one of the intrinsic problems of Thomson scattering diagnostics.

[1]The small value of α is actually the reason for the successful perturbative approach in QED.

For electron temperatures and photon energies occurring in our experiment the classical cross section is a good approximation and we will also limit our considerations to the classical calculation of the Doppler shift. This depends on the velocity component of the interacting electron along the differential scattering wave vector $\mathbf{k}$ given by

$$\mathbf{k} = \mathbf{k}_0 - \mathbf{k}_s \tag{3.14}$$

where $\mathbf{k}_0$ is the wave vector of the incident photon and $\mathbf{k}_s$ is the wave vector of the scattered photon along the observation direction. Since the absolute values of $\mathbf{k}_0$ and $\mathbf{k}_s$ are very similar $|\mathbf{k}|$ can be calculated by

$$|\mathbf{k}| = 2\,|\mathbf{k}_0| \sin\frac{\theta}{2} = \frac{4\pi}{\lambda_0} \sin\frac{\theta}{2} \tag{3.15}$$

where θ is the angle between $\mathbf{k}_0$ and $\mathbf{k}_s$. The frequency shift of the scattered light is then given by [89]

$$\Delta\omega = \omega - \omega_0 = -\left(\mathbf{k} \cdot \mathbf{v}\right) , \tag{3.16}$$

i.e. the highest frequency shift occurs when $\mathbf{k}$ and $\mathbf{v}$ are (anti)parallel.

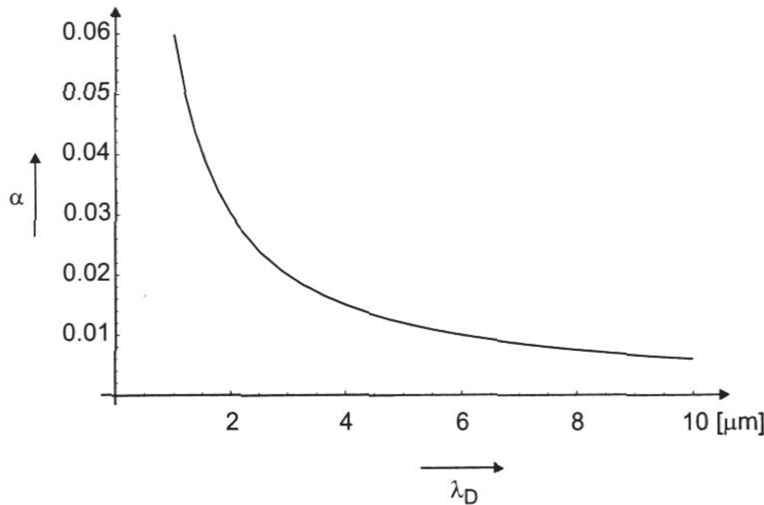

Figure 3.6.: Dimensionless scattering parameter α in dependence on Debye length λ_D in μm.

The scattering parameter determines whether the photon is scattered at a single electron or an ensemble of electrons and is defined as

$$\alpha = \frac{1}{|\mathbf{k}|\,\lambda_D} , \tag{3.17}$$

where λ_D is the Debye-length of the plasma. If $\alpha \ll 1$ the scattering spectra reflect the energy and velocity distribution of free electrons. This is called incoherent scattering. When $\alpha \gg 1$, the scattering takes place on a group of electrons and represents their collective movement. In this case the scattering is said to be coherent. For the expected electron densities and temperatures $\alpha \leq 1$, see figure 3.6, and therefore coherent scattering plays a modest role. When coherent scattering effects are neglected, the electron temperature T_e can be calculated from the full $1/e$ width of the Gaussian fit to the measured data using [93]

$$T_e = \frac{m_e c^2}{32 \sin\frac{\theta}{2}\, k_B \lambda_0} (\Delta\lambda_{1/e})^2 \,. \tag{3.18}$$

The electron density n_e is proportional to the area A_{Th} of the signal profile and the scattering cross section

$$A_{Th} = C n_e \sigma_{Th} \tag{3.19}$$

where the proportionality constant C can be determined from scattering experiments on a gas with well-know density and cross section. If incoherent scattering gives significant contribution to the scattering signal, one has to turn to a modified Gauss function as described e.g. in [89]. This leads in general to a broadening of the wings and flattening of the peak of the signal curve.
Rayleigh scattering on Ar can be used for calibrating the set-up since its cross-section is well-known and the density can be calculated via the ideal gas law. C follows from equation 3.19

$$C = \frac{A_{Ray}}{n_{Ar}\sigma_{Ray}} \tag{3.20}$$

where A_{Ray} is the area of the Rayleigh scattering signal and n_{Ar} the density of Ar at the actual measuring conditions. This leads to the expression

$$n_e = n_{Ar} \frac{A_{Th}}{A_{Ray}} \frac{\sigma_{Ray}}{\sigma_{Th}} \tag{3.21}$$

for the electron density. However, in case the Rayleigh scattering is laborious or impossible to measure one option is to employ Raman scattering for the calibration. This is done here for several reasons, one of which is just the blocking of the detector for Rayleigh photons due to the strong signal from the plasma while performing Thomson scattering, i.e. it is not possible to measure Rayleigh and Thomson scattering with the same set-up. As a consequence, in the experiments described below the calibration was performed by measuring the Raman scattering while introducing nitrogen at room temperature into the MPT as discussed in [86].

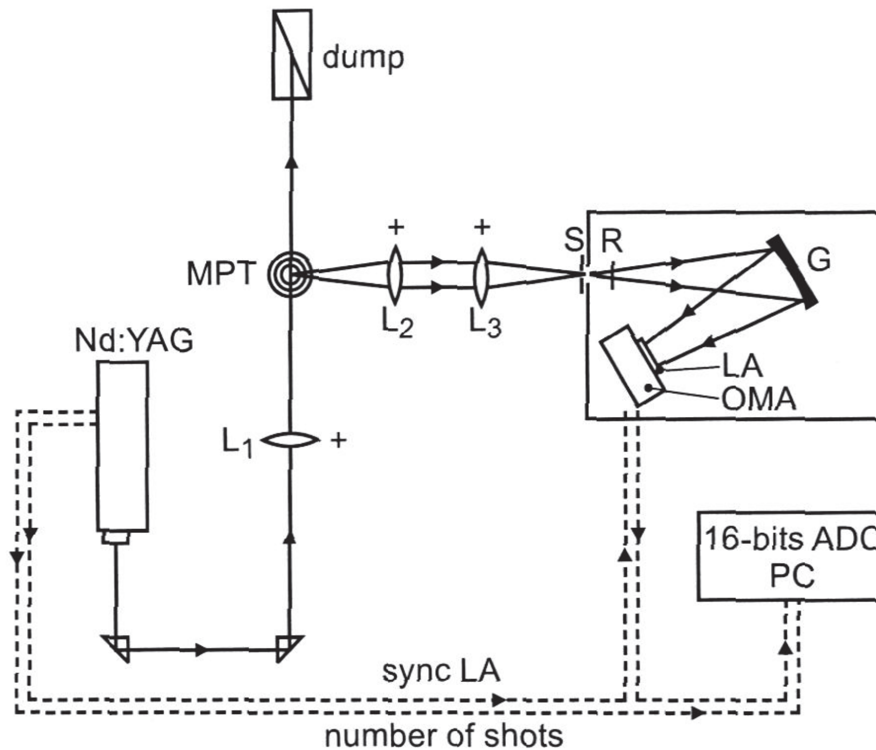

Figure 3.7.: Experimental set-up for the Thomson scattering measurement of the electron density and temperature of the MPT.

The MPT used in these experiments is described in section 3.2. The Thomson scattering measurements were performed with a Nd:YAG laser operated at 10 Hz at an energy of 0.4 J per pulse and a wavelength of 532 nm after frequency duplication. The radiation was directed through the plasma and the scattering profile was recorded at an angle of 90° with the aid of a high-resolution high-efficiency monochromator equipped with a cooled photo diode array. For the spatially resolved measurements the diameter of the probing beam was reduced from 1.0 mm to 0.2 mm. Spatially resolved measurements were made possible by placing the MPT on a y-z translation stage, with a positioning accuracy of 0.05 mm. A sketch of the set-up is given in 3.7.

3.3.2. Electron density and temperature mappings under different operating conditions

Photographic studies of the plasma

From digitally recorded pictures of the plasma a first impression of the influence of different parameters on the plasma shape could be obtained. As in the wavelength

range of 585 – 596 nm the greater part of the overall radiation density consists of continuum radiation we used an interference filter (585 – 596 nm) in front of the video camera. As this continuum emission is a consequence of free-bound-electron-transitions and is related to the plasma electron number density and the electron temperature, the changes in the recorded radiation densities do not stem from changes in the intensities of some lines. In figure 3.8 a picture of the plasma obtained at standard operation conditions is presented in the left upper corner. The plasma can be divided into two parts and as can be seen and we will refer to the lower and the upper part of the plasma as plasma cone and plasma plume, respectively. It was found that the general shape of the plasma does not change significantly within the typical power range of 50 – 150 W.

Influence of water on the plasma shape

As reported in [57] the Ar MPT is stable when introducing water or even acetonitrile droplet loaded aerosols, which distinguishes it from most other microwave plasmas like the ones obtained in a Surfatron or in the Beenakker cavity. In figure 3.8 three pictures of an Ar plasma obtained in an MPT when introducing different amounts of water vapour are given. The water was added to the internal gas flow while the total internal gas flow was kept constant. The introduction of water vapour was found to have no influence on the plasma stability in the range of $0 - 9\ \mathrm{mg\,min^{-1}}$ of water vapour as applied in this work. The general form of the plasma remains unchanged, however, at increasing water loading the plasma becomes more diffuse and an opening of the plasma cone is observed. The high stability of the plasma in the MPT could be explained from the fact that the initial plasma generating zone is located near the tip of the intermediate tube. The internal gas flow, which carries the aerosol, enters the plasma in the middle, as depicted by an arrow, and the high stability of the plasma when introducing the aerosol is due to the fact that little interaction occurs between the plasma and the aerosol in the region which is most critical for the plasma generation. In contrast herewith, both the Beenakker resonator and the Surfatron are mostly operated with one gas flow only and therefore there is no separation of the plasma generating zone from the sample introduction zone. This might explain the difference between the MPT and the Surfatron as well as the Beenakker cavity with respect to their reaction on the introduction of water loaded aerosols.

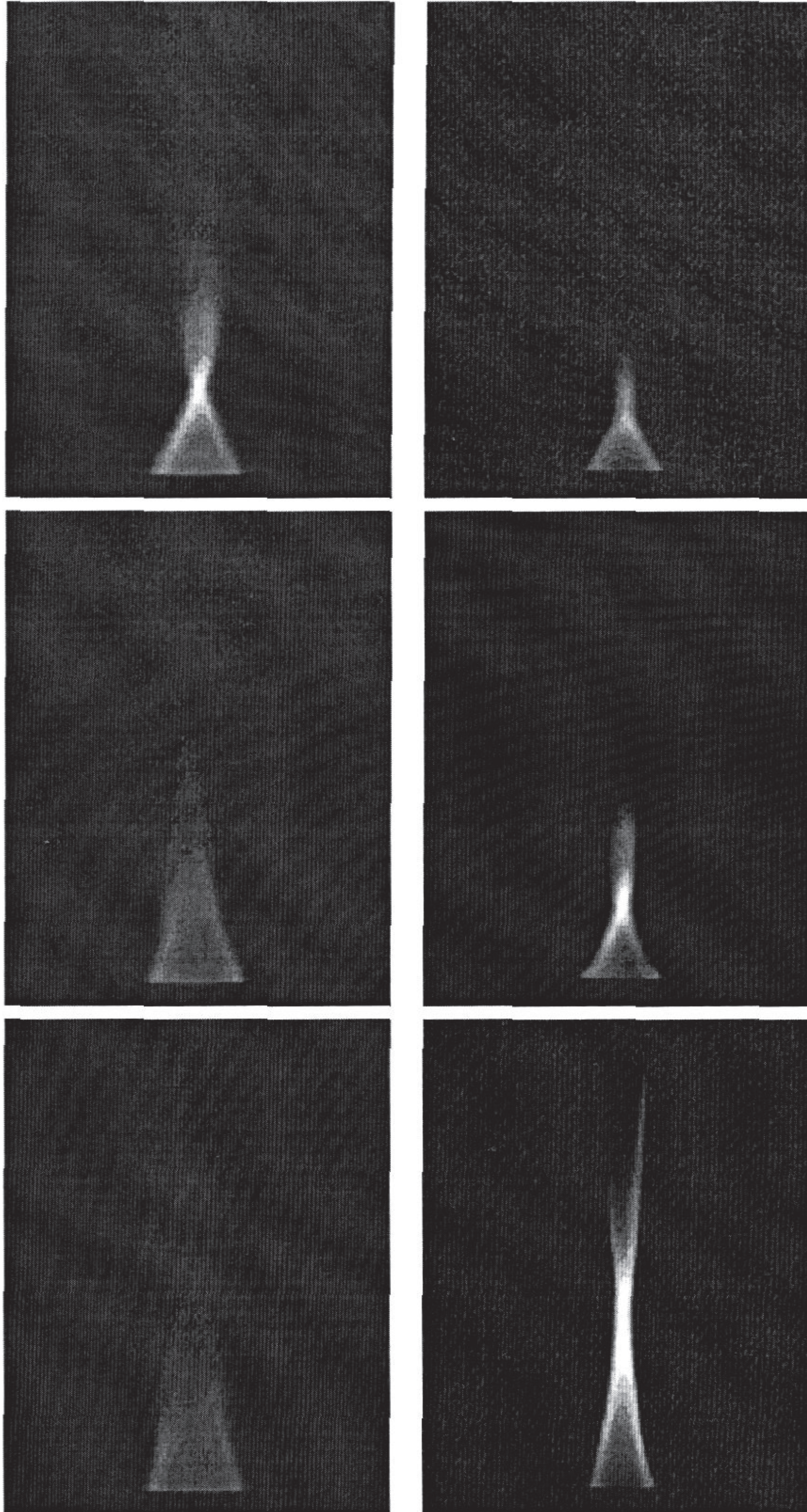

Figure 3.8.: Photographic images of the MPT plasma under different operating conditions. The left column shows the influence of the water loading of 0 mg min^{-1} , 4 mg min^{-1} *and* 10 mg min^{-1} *from top down and the right column documents the changes of the plasma with the internal gas flow of* 200 mL min^{-1} , 500 mL min^{-1} *and* 1000 mL min^{-1} *, respectively. Forward power is always* 100 W *and outer gas flow is* 200 mL min^{-1} .

Influence of the internal gas flow rate on the plasma shape

Changes in the flow rates of the internal gas of the MPT were found to have a drastic influence on the plasma shape. For a change of the internal gas flow between 200, 500 and 1000 $\mathrm{mL\,min^{-1}}$ of Ar (figure 3.8) the height of the plasma cone changes from about 5 mm (200 $\mathrm{mL\,min^{-1}}$) to 15 mm (1000 $\mathrm{mL\,min^{-1}}$) and the plasma emissivity increases. With gas flows of over 9 $\mathrm{L\,min^{-1}}$, being 50 times as high as in the normal operation mode, the plasma cone is elongated further but the form of the plasma remains unchanged. Variations of the outer gas flow in the range of 200 $\mathrm{mL\,min^{-1}}$ to 700 $\mathrm{mL\,min^{-1}}$ were also found to change the plasma shape. However, such variations are less relevant for analytical applications but indicate the facilities of the MPT as a plasma source for surface treatment.

Electron number density and electron temperature mappings

For the measurements of the Thomson profiles the scattering signals of 500 – 6000 laser shots were integrated. The estimated limit of detection for the electron number density is of the order of $5\,10^{19}$ $\mathrm{m^{-3}}$, as below this level the signals become very weak and the results of the calculations sometimes become unreasonable. The coordinate system was established at the beginning of the measurement campaign and was not changed afterwards, so that for every measurement the results refer to the same point in the plasma. For the spatially resolved measurements records were made at −0.8, −0.5, −0.3, 0, 0.2, 0, 4, 0.7 and 1 mm away from the plasma centre. Assuming a rotational symmetry of the plasma with respect to the plasma centre, we mirrored the values obtained for each side to the respectively other side and obtained values at 0, 0.2, 0.3, 0.4, 0.5, 0.7, 0.8 and 1 mm away from the plasma centre. The assumption of plasma symmetry was found to apply at least at the macroscopic level as indicated by the pictures of the plasma. Moreover, after this data manipulation no unreasonable profiles were obtained. Accordingly, half of the resulting plasma mapping contains all information.

Electron number density and electron temperature mappings at normal operation conditions

The first experiment was carried out with an MPT at normal operation conditions, namely at an internal gas flow of 500 $\mathrm{mL\,min^{-1}}$ Ar, at an outer gas flow of 200 $\mathrm{mL\,min^{-1}}$ Ar and at a microwave power of 100 W. Unless mentioned otherwise, no water vapour was introduced. For two reasons the lower limit for the observation height in the case of Thomson scattering was selected at about 4 mm above the

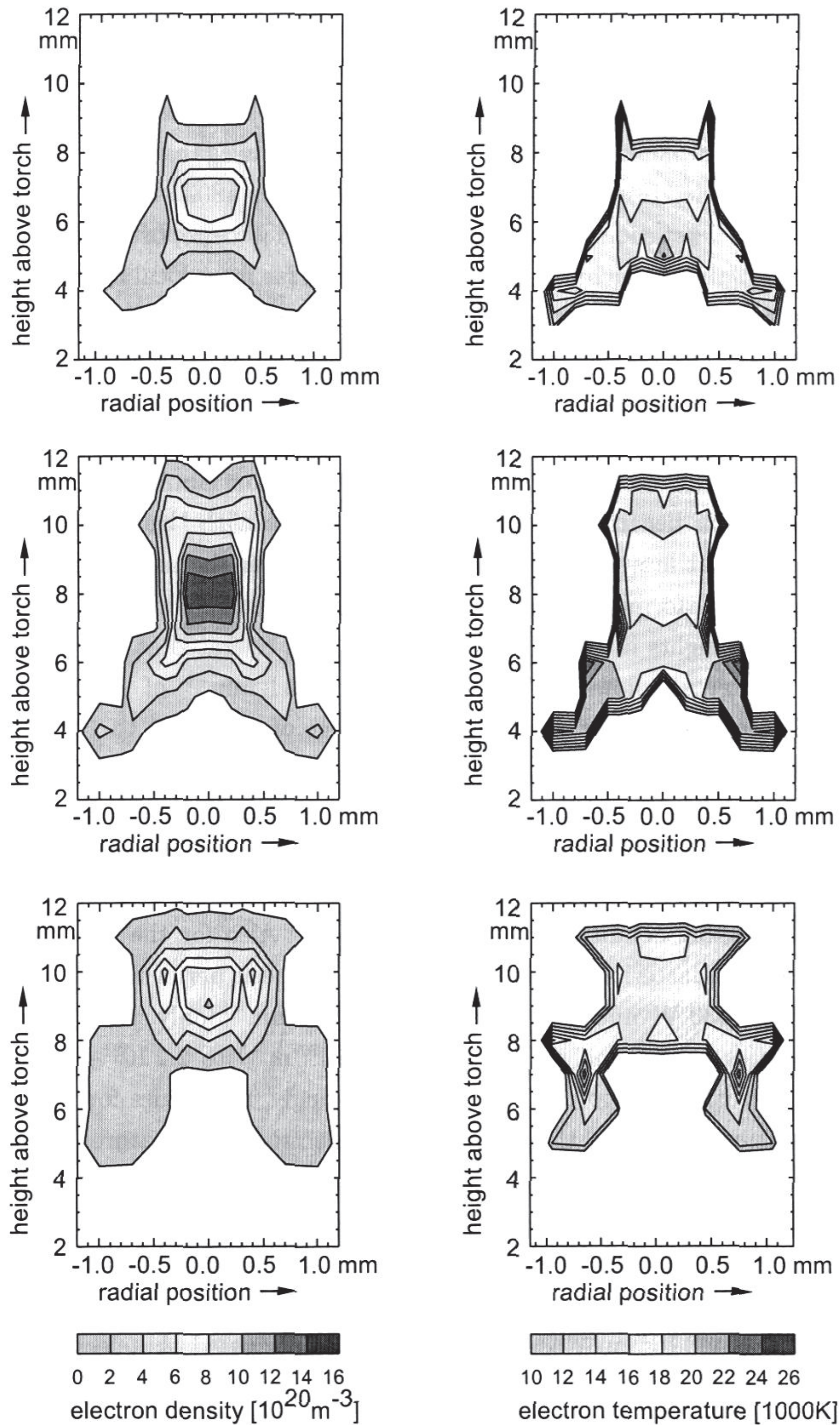

Figure 3.9.: Electron density (left column) and temperature (right column) mappings for the Ar *MPT operated with different internal and external gas flows; from top down:* 500 mL min^{-1} *and* 200 mL min^{-1}, 900 mL min^{-1} *and* 200 mL min^{-1}, 500 mL min^{-1} *and* 700 mL min^{-1} *for internal and external gas flow, respectively, at* 100 W *forward power.*

tip of the MPT. Firstly, at observation heights below 4 mm the signal became very weak indicating low electron densities and secondly stray radiation due to scattering of the laser radiation on the MPT torch itself drastically increased at lower observation heights. The measured electron number densities found range from 10^{20} m $^{-3}$ to 10^{21} m $^{-3}$ and the electron temperatures from 16000 K to 18000 K. As in an earlier work on the MPT rotational temperatures of 3600 K were reported [63] (see also next section) it can be concluded, that the plasma is far from local thermal equilibrium. Whereas the values of the electron number densities in the plasma were found to vary over about one order of magnitude the variation of the electron temperatures in the plasma is quite low. A comparison of the electron number density mappings with the digitally recorded pictures reveals that the highest electron number densities were found in the plasma cone region. The electron number densities in the plasma plume soon became too low to be measurable with the system used and they are therefore at least by an order of magnitude lower than in the plasma cone. Huang et al. [81] performed Thomson scattering measurements in the plasma centre and at different heights in the MPT. Their MPT was operated at 300 W and with internal and outer gas flows of 0.8 L min^{-1} and 1.2 L min^{-1} of Ar, respectively. They found electron number densities in the range of 10^{20} m $^{-3}$ to 10^{21} m $^{-3}$ and that the electron number density is maximum at 6 mm above the MPT torch. The electron temperatures were found to be of the order of 13000 K. Whereas the electron number density values agree very well with those found in our measurements the electron temperatures do not. This might be due to the considerable differences in the working conditions used in both cases. Also for the TIA microwave plasma Thomson scattering measurements [35] have been performed. This plasma was operated at 330 W and with one gas flow of 2 L min^{-1} only. Here the electron number densities were found to range from 3.5 10^{20} m $^{-3}$ to 2.2 10^{21} m $^{-3}$ and the electron temperatures to up to 24000 K. Accordingly, the values for the electron number densities as well as the values for the electron temperatures are slightly higher than those we found for the MPT. Cortino et al. [77] have determined the electron number densities in a Surfatron plasma from Stark broadening measurements of the H-line. At a microwave power of 100 W, a gas flow of 1 L min^{-1} and with end-on observation of the plasma they obtained values for the electron number densities of about 3 10^{20} m $^{-3}$. As for all plasmas discussed the electron number densities always were found to be in the range of 10^{20} m $^{-3}$ – 2 10^{21} m $^{-3}$, it can be concluded that these electron number densities are not a feature of the specific microwave plasma used but of microwave plasmas at atmospheric pressure in general. Marshall et al. [82] performed Thomson scattering measurements at an 875 W ICP

with an outer gas flow of 12 $\mathrm{L\,min^{-1}}$, an intermediate gas flow of 0.5 $\mathrm{L\,min^{-1}}$ and an internal gas flow of 0.6 $\mathrm{L\,min^{-1}}$. They first used Thomson scattering and found that the electron number density is maximum at the plasma axis and amounts to $2.3\,10^{21}\ \mathrm{m^{-3}}$ whereas the electron temperature at the same point is 11400 K [82]. Spatially resolved data for example have been provided by De Regt et al. [86]. For the case of a 1.2 kW Ar ICP they found that the electron number densities are in the range of $2\,10^{20}\ \mathrm{m^{-3}} - 1\,10^{21}\ \mathrm{m^{-3}}$ and the electron temperatures are about 6000 K to 8000 K. Whereas the electron number densities are very similar to the values found in this work for the case of the MPT, the electron temperature is much lower. The maximum electron number densities for the case of the ICP, the Surfatron and the TIA were found to occur just above the load coil and the launcher, respectively, and the electron number densities were found to decrease continuously with the observation height [5, 94, 95]. In contrast herewith it was found that the maximum electron number density for the case of the MPT, just as reported by Huang et al. [86] occurs at a height of 6 – 7 mm above the torch.

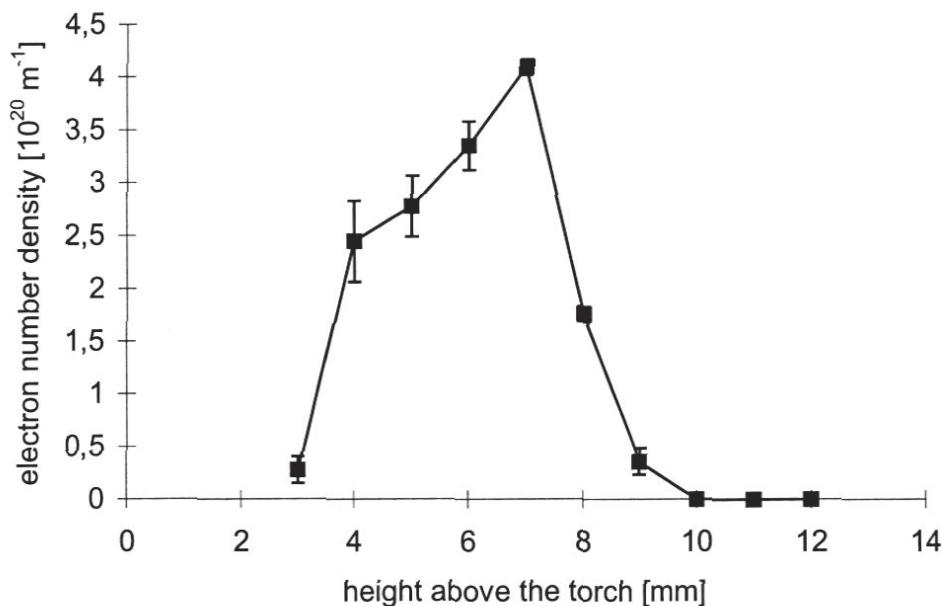

Figure 3.10.: Linear electron density n_e as a function of the observation height above the top of the torch. Power: 100 W *; internal gas flow:* 500 $\mathrm{mL\,min^{-1}}$ *; outer gas flow:* 200 $\mathrm{mL\,min^{-1}}$.

One might assume that the overall electron number remains the same for the whole plasma and that the high number density at 7 mm above the torch is just the result of the smaller plasma cross section here. In order to investigate this point in detail a

procedure described by Nowak et al. [94] can be followed, who proposed to integrate the electron number density over the whole plasma cross section. This results in a so-called linear electron number density N:

$$N(z) = 2\pi \int_0^R n_e(r, z)\, r\, \mathrm{d}r \tag{3.22}$$

where R is the plasma radius and z is the height above the torch. Of course, one has to be very careful with statements drawn from such calculations as only a fraction of the real electron density distribution is captured via Thomson scattering. This point is addressed again in the MPT modelling section.
The linear electron number density depends only on z and is defined in such a way that $N(z)\,\mathrm{d}z$ represents the total number of electrons in a horizontal slice of the plasma with a height $\mathrm{d}z$. The result of such a calculation, see figure 3.10, shows that not only the electron number density but also the total electron number has its maximum at 7 mm above the torch of the MPT. This contrasts with the ICP for which a decrease of the linear electron number density with the observation height at viewing positions between 5 and 20 mm above the load coil was observed [82].

Laterally resolved electron number density measurements at the MPT at normal operation conditions

Two lateral scans of the electron number densities in the MPT plasma were made at observation heights of 4 and 7 mm, respectively, see figure 3.11. At 4 mm above the torch the electron number densities were found to be of the order of 10^{20} m^{-3}. The maximum electron number density was found to occur at a radial distance of 0.8 mm away from the plasma centre. In the plasma centre no Thomson scattering signal could be observed, which indicates that the electron number density there is below $5\,10^{19}$ m^{-3}. Obviously at a location of 4 mm above the torch the plasma cone has a hollow structure. In contrast herewith the electron number density at 7 mm above the torch has a maximum in the plasma centre and no hollow structure could be observed.

The electron number density there was found to be $9.8\,10^{20}$ m^{-3}, which is almost by one order of magnitude higher than at a location of 4 mm above the torch. The occurrence of low electron number densities in the plasma centre has also been reported for the case of Thomson scattering at the ICP [84]. In contrast herewith, however, hollow structures are less common for microwave plasmas at atmospheric pressure such as the Surfatron and the Beenakker cavity, where normally filament plasmas are obtained. However, for the TIA operated at 1 kW a dip in the electron number density also was found to occur at an observation height of 2 mm [95].

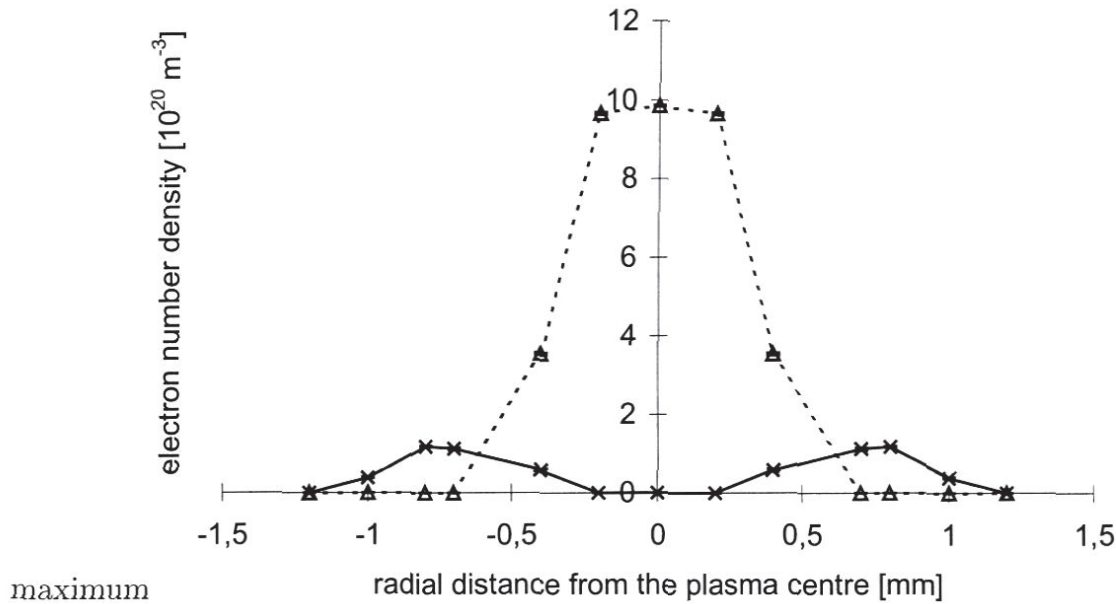

Figure 3.11.: Radial distribution of the electron density at observation heights of 4 mm *(solid line) and* 7 mm *(dashed line) above the top of the MPT. Power:* 100 W *; internal gas flow:* 500 $\mathrm{mL\,min^{-1}}$ *; outer gas flow:* 200 $\mathrm{mL\,min^{-1}}$.

Influence of gas flows on the electron density and the electron temperature

Systematic investigations of the influence of the gas flow rates on the plasma parameters of microwave discharges are hardly found in the literature. As the photographic images of the plasma showed that the gas flows in the case of the MPT are very important parameters, it was decided to investigate the influence of the gas flow rates on the electron temperatures and electron number densities in the MPT. The results for MPTs with internal gas flows of 500 $\mathrm{mL\,min^{-1}}$ to 900 $\mathrm{mL\,min^{-1}}$ and a constant power of 100 W as well as an outer gas flow of 200 $\mathrm{mL\,min^{-1}}$ show that an increase of the internal gas flow leads to a 2 mm upwards shift of the upper end of the zone in which electron number densities can be measured. This is understandable from the fact that with an increase of the internal gas flow the upper end of the plasma cone shifts upwards as it was discussed in 3.3.2. The maximum electron number density was also found to shift upwards by 2 mm and it increases from $8\,10^{20}$ $\mathrm{m^{-3}}$ to $1.6\,10^{21}$ $\mathrm{m^{-3}}$. The electron temperature remains almost unaffected when increasing the internal gas flow and only at the edges of the plasma an increase in temperature can be observed. The electron number density and electron temperature mappings for an MPT operated at different outer gas flows (200 to 700 $\mathrm{mL\,min^{-1}}$), at a power

of 100 W and with an internal gas flow of 500 $\mathrm{mL\,min^{-1}}$ are shown in 3.9. An increase of the outer gas flow was found to result in an upwards shift of the upper end of the zone in which electron number densities can be determined but the plasma length seems to remain unchanged. In contrast with the findings for the internal gas flow, an increase of the outer gas flow does not lead to higher electron number densities in the plasma centre. Only at the edges of the plasma the electron number density was found to increase slightly. An increase of the outer gas flow further was found to lead to a cooling of the plasma and the electron temperature measured decreases from 18000 K to 16000 K.

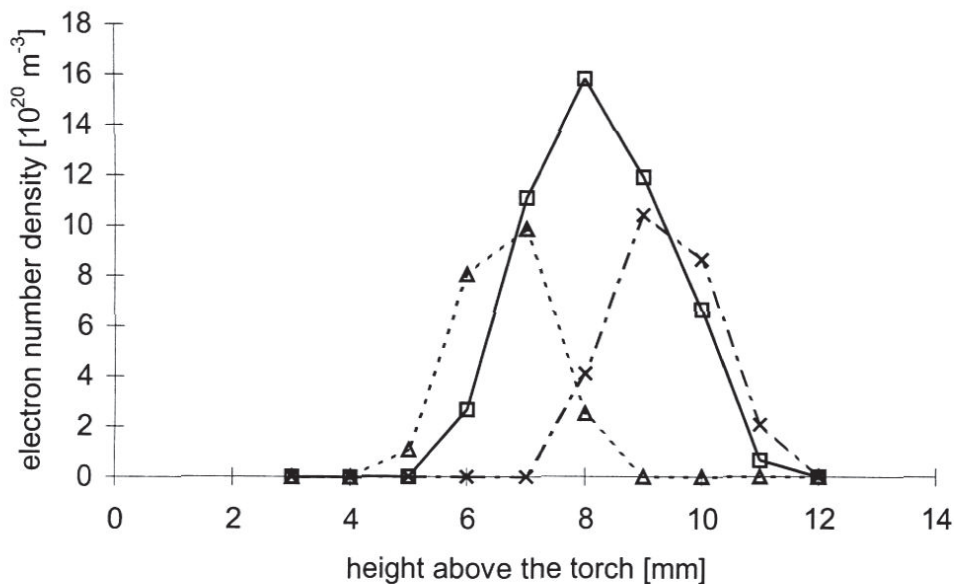

Figure 3.12.: Electron density axial scans for different operating conditions. Power: 100 W*; internal gas flow:* 500 $\mathrm{mL\,min^{-1}}$*; outer gas flow:* 200 $\mathrm{mL\,min^{-1}}$ *(△); internal gas flow:* 900 $\mathrm{mL\,min^{-1}}$*; outer gas flow:* 200 $\mathrm{mL\,min^{-1}}$ *(□); internal gas flow:* 500 $\mathrm{mL\,min^{-1}}$*; outer gas flow:* 700 $\mathrm{mL\,min^{-1}}$ *(×).*

The influence of the observation height on the electron number density is shown by the plot of the electron number density in the middle of the plasma versus the observation height in figure 3.12. The errors are of the order of $3-5\%$ and therefore no error bars are provided. The data show that with an increase of the internal gas flow from 500 $\mathrm{mL\,min^{-1}}$ to 900 $\mathrm{mL\,min^{-1}}$ a drastic increase of the maximum of the electron number density occurs and the position of the maximum shifts 1 mm upwards. Also the length of the zone in which electron number densities can be

measured was found to increase from 4 mm to 6 mm. In contrast herewith an increase of the outer gas flow from 200 mL min^{-1} to 700 mL min^{-1} does not lead to an elongation of the zone in which electron densities can be measured. Further, an increase of the outer gas flow does not affect the maximum electron number density, however, the position of the maximum moves 2 mm upwards.

Influence of water introduction on the electron density and the electron temperature in the MPT

In order to investigate the influence of water on the plasma parameters we mixed the internal gas flow with different amounts of the Ar flow saturated with water vapour. We only measured at the tip of the plasma cone, which was located 7 mm above the torch and in order to avoid artifacts arising from small spatial changes in the plasma we increased the diameter of the laser beam to 1 mm.

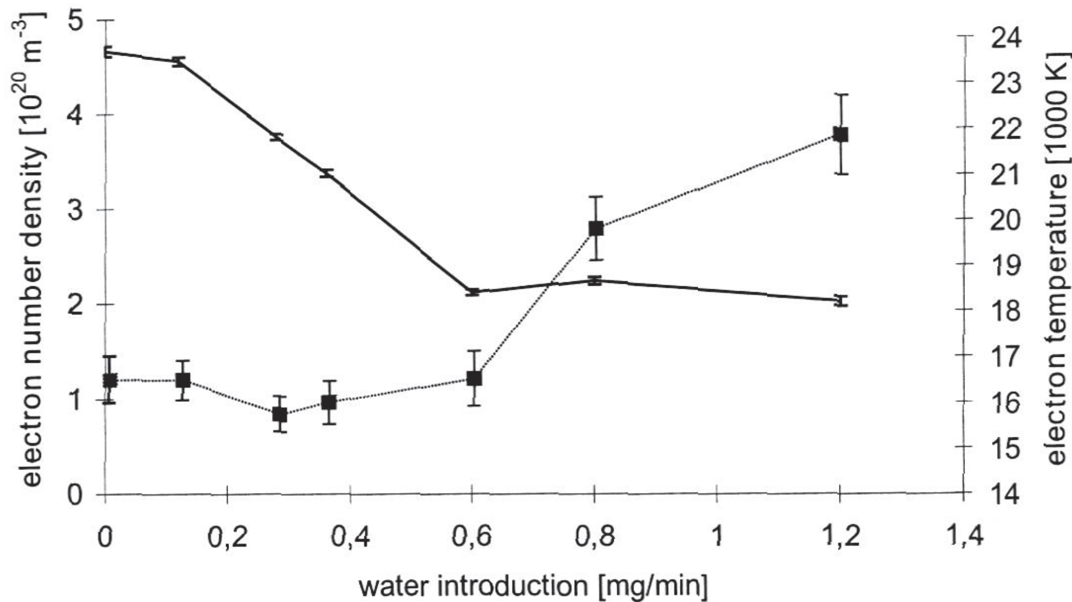

Figure 3.13.: Influence of water on the electron density (straight line) and the electron temperature (dotted line). Data for the centre of the plasma at an observation height of 7 mm *above the top of the MPT.*

The measurement point used was selected because the tip of the cone is easy to find and also because the electron number density at this point can be expected to be well above the limit of detection. Accordingly, it also should be easily possible to measure decreases in the electron number density as a result of water introduction.

The results in figure 3.13 show that the electron number density decreases up to a water uptake rate of 0.6 mg $\min^{-1}$ but at a still higher water loading of the internal gas flow it remains constant. The electron temperature was found to remain constant up to a water loading of 0.6 mg $\min^{-1}$ and increases from 17500 K at a water loading of 0.6 mg $\min^{-1}$ to 22500 K at a water loading of 1.2 mg $\min^{-1}$. Especially for the case of the ICP the influence of the water loading has been well discussed in the literature. Alder et al. [96] and Long et al. [97] reported an increase in electron number density when introducing water into the plasma. Caughlin and Blades [98] found the same trend but noted that the effects were not significantly beyond the measurement error. Nowak et al. [40] also reported that the electron number density increases with the water loading of the internal gas flow. However, because the plasma is shrinking the total number of electrons in a horizontal slab of the plasma decreases. In these works temperatures were determined from measurements of line intensities or Stark broadening and it was necessary to perform an Abel-inversion of the data resulting in a significant error for measurement points along the plasma axis. Huang et al. [84] first used Thomson scattering to investigate the influence of water on the spatial distribution of electron number densities and electron temperatures in the ICP. They found that the influence of water on the plasma parameters strongly depends on the power. At high power levels the electron number densities increase with the water loading while at low power levels a decrease of the electron number densities can be observed. This may be the result of a competition of two mechanisms. On the one hand hydrogen promotes the energy transfer from the sides of the plasma to the centre but on the other hand energy has to be used to heat the water and to dissociate it. The latter might have only a limited influence in the case of the ICP since the power available by far exceeds the power necessary for the dissociation of water and therefore an increase of the electron densities as a result of the increasing amounts of hydrogen is observed. At a lower power the energy required for the vapourisation and dissociation of water might become increasingly important and therefore a decrease of the electron number density as a result of water introduction is observed for the case of a 0.75 kW ICP. Along this line of interpretation the decrease of the electron number density with an increasing input of water for the case of the MPT is well understandable. Indeed the latter is operated at 100 W only, by which the energy required for a vapourisation and dissociation of the water can be understood to significantly contribute to the energy balance. Further, the introduction of molecular compounds also provides for additional electron loss channels. However, there are other differences between low power ICPs and the 100 W MPT and for a detailed comparison of the effect of

water in both cases, experiments with high power microwave plasmas such as the TIA or the CMP should be carried out.

Influence of the microwave power on the electron densities and the electron temperatures in the MPT

The influence of the microwave power on the electron number densities and the electron temperatures was investigated for one location in the plasma. The results in figure 3.14 show that the electron number densities increase from $3.8\,10^{20}$ m $^{-3}$ to $7.2\,10^{20}$ m $^{-3}$, when the power changes from 80 W to 180 W. The electron temperatures were found to remain widely unchanged, except for the higher value at a power of 80 W. This fact is in good agreement with the theory since an increase in power and accordingly in electrical field strength is supposed to influence the electron number density and not the average electron energy [67]. However, for the ICP both the electron temperature and the electron number density were found to increase with the power [84].

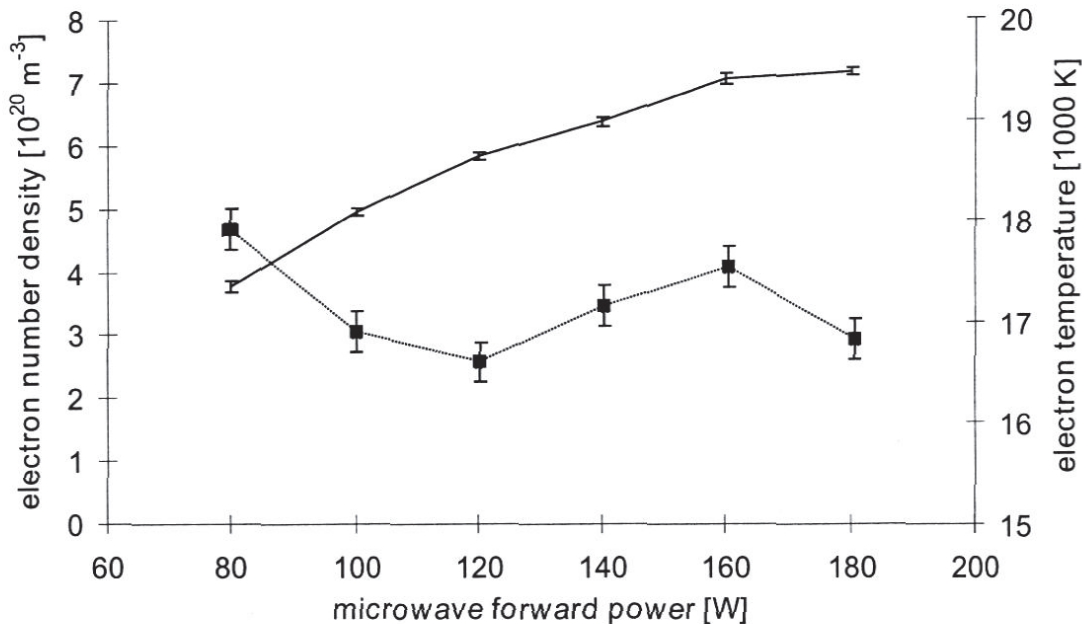

Figure 3.14.: Influence of the microwave forward power on the electron density (straight line) and the electron temperature (dotted line). Data for the centre of the plasma at an observation height of 7 mm *above the top of the MPT.*

Discussion of results

In this section electron number density mappings as well as pictures of an Ar MPT operated at 2.45 GHz at different operating conditions are presented. It is shown that the plasma can be separated in a plasma cone with a hollow structure and a plasma plume. Under normal operation conditions, including an internal gas flow of 500 $\mathrm{mL\,min^{-1}}$, an outer gas flow of 200 $\mathrm{mL\,min^{-1}}$ and a power level of 100 W, the electron number densities range from 0.5 10^{20} $\mathrm{m^{-3}}$ to 10^{21} $\mathrm{m^{-3}}$ and the electron temperatures from 16000 K to 18000 K. The hollow structure of the plasma cone could be verified. The form of the plasma proves to strongly depend on the internal gas flows. An increase of the internal gas flow from 500 $\mathrm{mL\,min^{-1}}$ to 900 $\mathrm{mL\,min^{-1}}$ leads to an elongation of the plasma cone and to an increase of the maximum electron number density by a factor of 2. In contrast herewith an increase of the outer gas flow from 200 $\mathrm{mL\,min^{-1}}$ to 700 $\mathrm{mL\,min^{-1}}$ does not effect the maximum electron number density, however, causes the plasma to be lifted slightly. An increase of the power leads to higher electron number densities, as it was shown for specific locations in the plasma, whereas the resulting electron temperatures remain unchanged. Water loadings of up to 0.6 $\mathrm{mg\,min^{-1}}$ in the internal gas flow cause a decrease of the electron number density at the tip of the plasma cone by a factor of 2 whereas the electron temperatures also remain unchanged. With an increase of the water loading from 0.6 $\mathrm{mg\,min^{-1}}$ to1.2 $\mathrm{mg\,min^{-1}}$ the electron temperatures were found to increase from 16000 K to 22000 K whereas the electron number densities remain constant. These specific properties of the Ar MPT operated at 2.45 GHz are visualized by pictures of the plasma at the different operation conditions.

3.4. Heavy particle temperature by spectroscopic measurements

A further important parameter in the characterisation of a plasma is its gas kinetic temperature. The rotational temperature of the OH radical is a good approximation to this. The measurement procedure uses the the $A^2\Sigma^+ \rightarrow X^2\Pi_i$ OH band [99] at 306.4 nm and the temperatures are obtained from the slope of a Boltzmann plot, i.e. thermodynamic equilibrium between the heavy particles is assumed. A charge coupled device (CCD) in combination with a Czerny-Turner monochromator is used to obtain spatially resolved intensities and to simultaneously detect the different rotational lines.

As the measured signals are line integrated along the path of sight, an Abel inversion

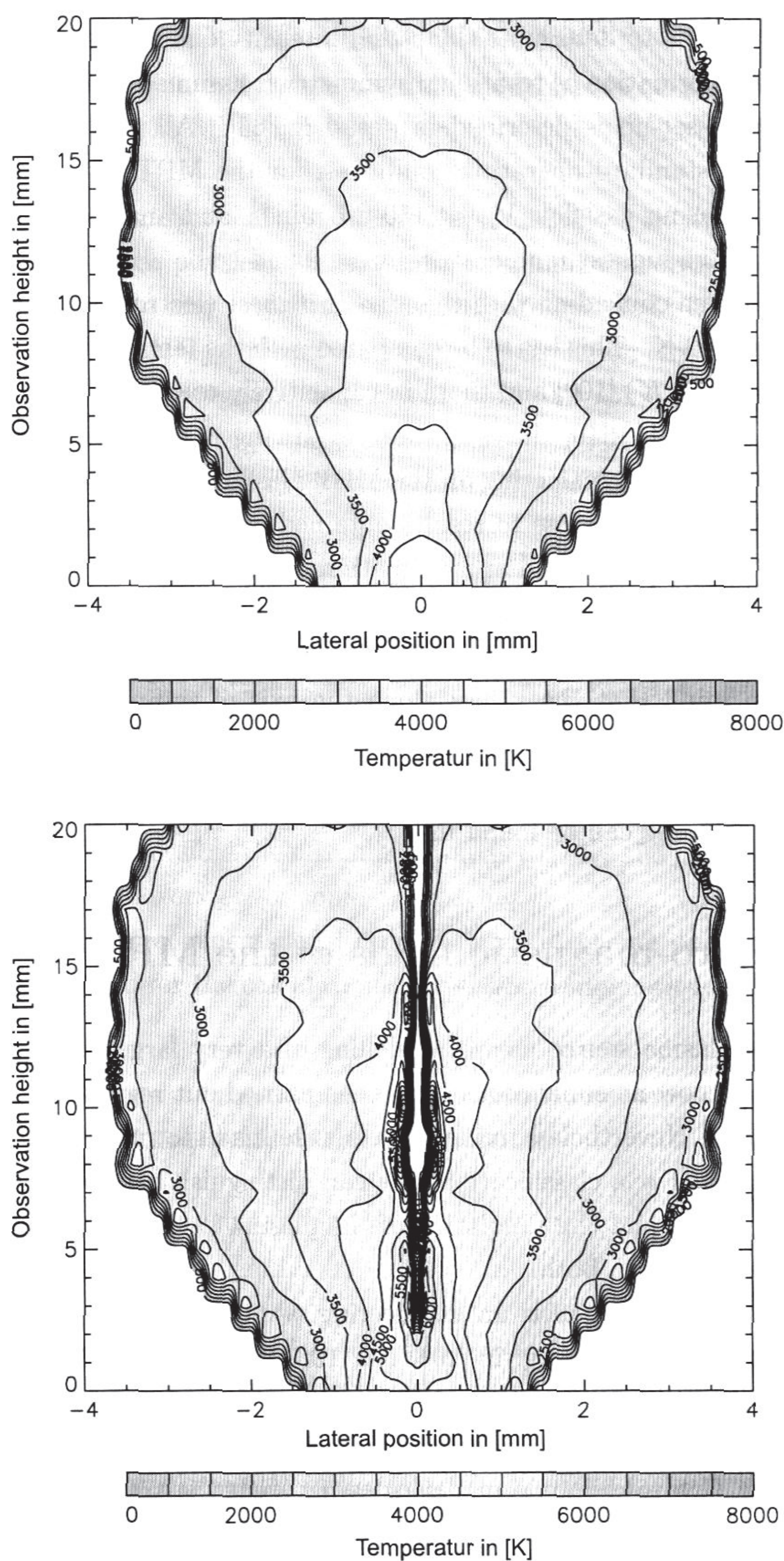

Figure 3.15.: Lateral scan of the rotational temperature of the OH radical in an MPT plasma (upper picture). Radial scan of the rotational temperature resulting from numerical Abel inversion (lower picture).

has to be carried out to determine the radial intensity distribution. This is a two dimensional transformation as rotational symmetry is assumed here. The procedure and experimental set-up is described in detail in [63]. All the results presented here refer to the standard operating conditions for the MPT, i.e. forward power $P_{in} = 100$ W, plasma gas flow $\dot{V}_{ar} = 150$ mL min^{-1} and analyte gas flow $\dot{V}_{an} = 450$ mL min^{-1}. The highest temperatures were found to be about 5000 K near the centre of the plasma coinciding with the area of highest electron density. The mean temperature is 3600 K. This has to be compared with the temperatures measured in resonant MIPs (2000 K) [100] and those in capacitively coupled microwave plasmas (CMP) (3400 – 4200 K) [40]. Investigations by Huang et al. [95] of the gas kinetic temperature by Rayleigh scattering on the MPT plasma revealed a maximum of up to 6000 K, which is quite close to results obtained by spectroscopic measurements here and demonstrates the good approximation of the method. A lateral scan, i.e. line integrated along path of sight, of the rotational temperature is shown in figure 3.15. Abel inversion of this data results in the plot shown in figure 3.15 where one should keep in mind that the values along the axis of symmetry are most error prone. Therefore these should be compared to the respective values of the lateral scan. Further studies of the influence of several parameters like forward power, gas flow and water loading can be found in [63].

3.5. Electro-magnetic fields of the MPT

Modelling of a plasma source means modelling of a very large variety of physical effects and up to now no simulations have been carried out regarding all aspects of technical plasmas. Nevertheless, many efforts were made to understand the details of current interest. For a classification, one can distinguish between the simulation of the plasma source and the simulation of the plasma itself, though there exists a natural coupling between both.

Modelling the plasma source is an engineering work and concentrates on mostly numeric electromagnetics, as e.g. in [101, 102, 103, 104, 105], and fluid-dynamic calculations [106, 107], while plasma modelling is an active area of research in plasma physics and its success strongly relies on the assumptions made. Here again a sub-classification in (hydro)dynamic models, dealing with the transport properties of the different species in a plasma and kinetic models for e.g. the electron energy distribution function (EEDF) can be made [68, 108, 109, 110]. Especially for the ICP several complete simulations trying to describe the electromagnetic field and the plasma with its dynamic and kinetic properties have been carried out [12, 111, 112].

These are, however, not applicable to the MPT, first due to their lack of an appropriate microwave description and second the fluid model has to be highly sophisticated since the gas flows in the MPT are very complex despite its relatively simple geometry.
To keep the modelling efforts at a moderate level and allow for an engineering tool rather than a thorough physical understanding we limit ourselves to some aspects of the MPT modelling and regard them as separate systems. In section 3.2.1 we already analysed the MPT in terms of its wave transmission characteristics. In the next sections the electromagnetic field calculations and some fluid-dynamic simulations are presented. Although these descriptions lack self-consistency there exist some interfaces which could be used to overcome this problem in an iterative way.

The electromagnetic field of the MPT is basically the field of an open coaxial line scattered into free space and several analytical approximation exist for its calculation. In case of the MPT less than 1 % of the input power is radiated into the surrounding. All these analytical approximations rely on certain assumptions and all bear the same problem; as soon as the plasma has to be considered these are all unusable.
To keep as general as possible the a common way is to solve the governing equations numerically. A short overview of some approaches is given in chapter B. Here it is enough to say that a generalised Finite Difference scheme on mapped grids is developed and applied for the calculations of the electromagnetic fields of the MPT.

3.5.1. Electro-magnetic field equations

The electro-magnetic fields sustaining the microwave induced plasma are described by Maxwell's equations

$$\begin{aligned} \nabla \times \underline{\mathbf{H}} &= \underline{\mathbf{J}} + \mathrm{j}\varepsilon_0\varepsilon_r\omega\underline{\mathbf{E}} = \mathrm{j}\varepsilon_0\underline{\varepsilon}_{pl}\omega\underline{\mathbf{E}} \\ \nabla \times \underline{\mathbf{E}} &= -\mathrm{j}\mu_0\omega\underline{\mathbf{H}} \end{aligned} \tag{3.23}$$

for dissipative, neutral and non-magnetic media. We assumed a harmonic time dependence $e^{j\omega t}$ since the steady state solutions are of interest here. The time averaged fields are then given by

$$\mathbf{E} = \frac{1}{T}\int_{-T/2}^{T/2} \underline{\mathbf{E}}\,\mathrm{d}t = \frac{1}{2}\sqrt{\underline{\mathbf{E}}\underline{\mathbf{E}}^{\star}}\ . \tag{3.24}$$

The complex plasma permittivity $\underline{\varepsilon}_{pl}$ is determined by the electron density n_e and the collision frequency ν as [66]

$$\underline{\varepsilon}_{pl} = 1 - \left(\frac{\omega_p}{\omega}\right)^2 \frac{\omega}{\omega - \mathrm{j}\nu} \tag{3.25}$$

with the plasma frequency ω_p defined as

$$\omega_p = \sqrt{\frac{n_e e^2}{\varepsilon_0 m_e}} \; . \tag{3.26}$$

ε_0 and μ_0 are the free-space permittivity and permeability, e is the electron charge and m_e the electron rest mass.
Eliminating the electrical field in the two Maxwell equations leads to the double curl equation

$$\nabla \times \nabla \times \underline{\mathbf{H}} = \varepsilon_0 \mu_0 \underline{\varepsilon}_{pl} \omega^2 \underline{\mathbf{H}} + \frac{\nabla \underline{\varepsilon}_{pl}}{\underline{\varepsilon}_{pl}} \times \nabla \times \underline{\mathbf{H}} \tag{3.27}$$

For vanishing gradients in the relative permittivity, $\nabla \underline{\varepsilon}_{pl} = 0$, this simplifies to the Helmholtz-equation

$$\Delta \underline{\mathbf{H}} + \varepsilon_0 \mu_0 \underline{\varepsilon}_{pl} \omega^2 \underline{\mathbf{H}} = 0 \; . \tag{3.28}$$

Note that Δ is the Vector-Laplace operator defined as

$$\Delta \equiv \nabla \left(\nabla \cdot\right) - \nabla \times \nabla \times \quad . \tag{3.29}$$

For numerical reasons 3.27 is rewritten into the form

$$\nabla \times \frac{1}{\underline{\varepsilon}_{pl}} \nabla \times \underline{\mathbf{H}} = \varepsilon_0 \mu_0 \omega^2 \underline{\mathbf{H}} \tag{3.30}$$

which enables an hermitian form of the discretised equation with respect to variations in $\underline{\varepsilon}_{pl}$.
In order to keep computation time and memory requirements at moderate levels we make the reasonable assumption of rotational symmetry of the problem considered thus leaving us with a quasi two-dimensional situation. The physical coordinate system used is the $(r, \varphi, z) - \mathit{system}$ which has to be distinguished from the computational coordinate system which has also rotational symmetry. Then all field components are derived from the azimuthal component of the magnetic field $\underline{\mathbf{H}}_\varphi$.

This reduces the double curl equation 3.30 to an equation for only one vector component:

$$[\nabla \times \frac{1}{\underline{\varepsilon}_{pl}} \nabla \times \underline{\mathbf{H}}]_\varphi = \varepsilon_0 \mu_0 \omega^2 \underline{\mathbf{H}}_\varphi \tag{3.31}$$

The electrical field can be calculated from the magnetic field by means of equation 3.5.1. Figure 3.16 shows a schematic drawing of the computation domain, i.e. the physical area for which equation 3.31 should be solved.

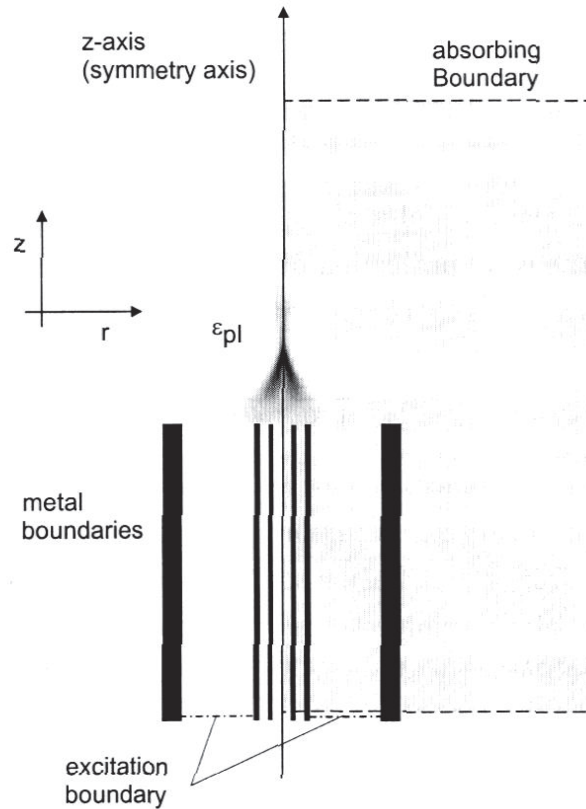

Figure 3.16.: Schematic drawing of the upper end of the Microwave Plasma Torch (MPT). The computation domain is indicated by a grey background; the excitation boundary (dotted lines) is sufficiently deep in the coaxial line for a pure TEM *field configuration.*

3.5.2. Boundary conditions

The boundary conditions are most subtle to set in any numerical approach to solve differential equations on a grid by discretisation. In figure 3.16 the computation

domain with applied boundary conditions is shown for the MPT. As a very good approximation the metallic surfaces can be regarded as ideal thus causing vanishing tangential electric fields

$$(\underline{\mathbf{E}} \cdot \mathbf{n}) = ((\nabla \times \underline{\mathbf{H}}) \cdot \mathbf{n}) = 0 \tag{3.32}$$

where $\mathbf{n}$ is a unit vector perpendicular to the surface. The Maxwell equations 3.5.1 indirectly determine the boundary condition for the magnetic field $\underline{\mathbf{H}}_{\varphi}$which is of the form of a homogeneous Neumann condition. The open boundaries ∂V of the computation domain are described by Absorbing Boundary Conditions (ABC) in 1st order [113, 114]

$$(\nabla \pm j\omega\sqrt{\varepsilon_0 \mu_0 \underline{\varepsilon}_{pl}})\underline{\mathbf{H}}_{\varphi}|_{\partial V} = \hat{P}^{\pm}\underline{\mathbf{H}}_{\varphi}|_{\partial V} = \mathbf{0} \tag{3.33}$$

which imply the assumption that the electro-magnetic wave propagates beyond the discretisation region in the form of a plane wave. As a shortcut we introduced the forward/backward plane wave projection operator $\hat{P}^{\pm}$. The absorption efficiency of this boundary is known to vary strongly with the incident angle θ as

$$R = \frac{1 - cos(\theta)}{1 + cos(\theta)} ,$$

this means that there are no reflections for perpendicular incidence, only. But calculations show that this is only of minor importance in our case as long as the boundary is sufficiently far away from the radiation source (plasma). Other "unknowns" as i.e. the exact conductivity distribution introduce the dominant error. Nevertheless, superior methods like the Perfectly Matched Layer (PML) as described in [115, 116] or simply higher order ABC would increase the computational accuracy with respect to this problem, if required.
The magnetic field $\underline{\mathbf{H}}_{\varphi}$has to vanish along the axis of rotational symmetry $r = 0$ for continuity reasons, i.e. it follows a homogeneous Dirichlet boundary condition for $r = 0$:

$$\underline{\mathbf{H}}_{\varphi}|_{r=0} = 0 . \tag{3.34}$$

Excitation and matching network

Care has to be taken at the excitation boundary; in general, this has to be set equal to a superposition of a forward and reflected TEM-wave which implies the knowledge of the reflection factor. This is an ad hoc unknown quantity since it involves the interaction of the electro-magnetic wave with obstacles in the computation domain. A classical approach to this problem is the application of Poynting's theorem

3.1 to express the electro-magnetic field in the computation domain as an effective impedance with respect to an in-coupling waveguide (a coaxial waveguide in our case) [117]. More elegantly and common in finite difference time domain (FDTD) applications, this problem is circumvented by the use of absorbing boundary conditions at the excitation boundary for the reflected wave:

$$\hat{P}^{-}[\underline{\mathbf{H}}_{\varphi}^{-}] = \mathbf{0} \tag{3.35}$$

where $\underline{\mathbf{H}}_{\varphi}^{-}$ denotes the reflected magnetic wave. This can be rewritten as

$$\hat{P}^{-}[\underline{\mathbf{H}}_{\varphi}] = \hat{P}^{-}[\underline{\mathbf{H}}_{\varphi}^{+}] \tag{3.36}$$

yielding the in-coupling ABC condition at the excitation boundary. $\underline{\mathbf{H}}_{\varphi}^{+}$ is the forward propagating TEM wave which is generally known because we can solve the Helmholtz equation 3.28 for an infinite coaxial transmission line analytically. Using cylindrical coordinates the TEM wave is described by

$$\underline{\mathbf{H}}_{\varphi}^{+} = \sqrt{\frac{P_{in}}{2\pi^2 Z_C}}\frac{1}{r}\,\mathrm{e}^{-\mathrm{j}\beta z} \tag{3.37}$$

where P_{in} is the forward power. The complex reflection factor $\underline{\Gamma}$ is then calculated at any point in the (coaxial) waveguide as

$$\underline{\Gamma} := \frac{-\underline{\mathbf{H}}_{\varphi}^{-}}{\underline{\mathbf{H}}_{\varphi}^{+}} = \frac{\underline{\mathbf{H}}_{\varphi}^{+} - \underline{\mathbf{H}}_{\varphi}}{\underline{\mathbf{H}}_{\varphi}^{+}}\ . \tag{3.38}$$

Up to now we only considered that part of the MPT as displayed in figure 3.16. But the actual MPT consists of more parts, see figure 3.1, namely the slotted part of the coaxial line with the short circuit for impedance matching. These are described by a two port equivalent circuit as shown in figure 3.2. Consequently, for a correct description of the exciting TEM wave for the numerical calculation one has to evaluate the elements of the scattering matrix **S** (see figure 3.3 for definition), which are always complex here and which will not be marked by underlining for simplicity.
Looking at figure 3.2 one can calculate the matrix elements S_{11} and S_{22} of the complex amplitude scattering matrix **S** [72] by matching the respective output port in reference plane t_1 or t_2. Since the MPT is a reciprocal junction it follows that $S_{12} = S_{21}$. Neglecting inner losses in the MPT device, which is actually a fairly good approximation, imposes the condition of energy conservation and thus for the complex amplitudes

$$\left|V_1^-\right|^2 + \left|V_2^-\right|^2 = \left|V_1^+\right|^2 + \left|V_2^+\right|^2\ , \tag{3.39}$$

which allows the calculation of S_{12} from S_{11} and S_{22}. The complex independent matrix elements are then give by

$$\mathbf{S} = \begin{pmatrix} S_{11} & S_{12} \\ S_{21} & S_{22} \end{pmatrix} = \begin{pmatrix} \frac{Y_c^{coax} - Y_c^{MPT} - \mathrm{j}B}{Y_c^{coax} + Y_c^{MPT} + \mathrm{j}B} & \sqrt{1 - S_{11}S_{11}^{\star}}\, \mathrm{e}^{\frac{1}{2}\mathrm{j}(arg(S_{11}) + arg(S_{22}) + \pi)} \\ S_{21} = S_{12} & \frac{Y_c^{MPT} - Y_c^{coax} - \mathrm{j}B}{Y_c^{MPT} + Y_c^{coax} + \mathrm{j}B} \end{pmatrix} \tag{3.40}$$

with $arg(S_{11}, S_{22}) \in [-\pi/2, \pi/2]$. Now we have to express the TEM excitation in the MPT reference plane t_2 in terms of the scattering matrix $\mathbf{S}$ and the TEM excitation at the MPT in-coupling t_1. The forward TEM wave V_2^+ is given by

$$V_2^+ = S_{21}V_1^- + S_{22}V_2^- = S_{21}V_1^- + S_{22}\underline{\Gamma}_l(t_2)V_2^+ \tag{3.41}$$

where we introduced the reflection factor $\underline{\Gamma}_l$ of the load denoted Z_p' in figure 3.2 at t_2. Solving for V_2^+ leads to the expression

$$V_2^+ = \frac{S_{21}}{1 - \underline{\Gamma}_l S_{22}} V_1^- \tag{3.42}$$

for the TEM excitation one would have to impose at reference plane t_2 as a function of the matching network expressed via $\mathbf{S}$ and the TEM wave at the in-coupling at t_1. Unfortunately, $\underline{\Gamma}_l$ is an unknown quantity which itself is a result of the numerical calculation to be carried out. If the assumption of a linear dependence of $\underline{\Gamma}_l$ on the electromagnetic field can be used, a simple way to overcome this problem is to carry out a calculation with $\underline{\Gamma}_l = 0$ and re-normalise the field values afterwards with a correction factor

$$\delta V_2^+ := \frac{1}{1 - S_{22}\underline{\Gamma}_l} . \tag{3.43}$$

We will follow this procedure in the next sections, it can also be applied in the case of non-linearities as long as these are treatable in an iterative manner where the re-normalisation has to be carried out after each iteration step.

3.5.3. Numerical approach

The finite difference approximation FD is a relatively simple way to obtain numerical solutions of differential equations and is a standard numerical method in computational electrodynamics both for frequency and time domain calculations

[118, 119, 120]. In the field of time domain calculations the Yee algorithm became the standard procedure due to its stability and the intrinsic fulfilment of Maxwell's 3rd and 4th equations in free space. This is accomplished by choosing a discretisation scheme such that the commutator of two spatial derivatives $[\partial_x, \partial_y] = 0$ vanishes even in discrete form. This scheme is generally applied to simple equidistant rectangular grids. However, many applications require more complicated and boundary fitted grids as well as non-equidistant grid lines in order to achieve a sufficient numerical accuracy at reasonable grid sizes. A covariant formulation of the differential equation, e.g. Maxwell's equations or the vector wave equation, provides a general approach for mapping arbitrary curvilinear physical grids onto e.g. equidistant Cartesian computational grids [121]. Conformal mapping for solving the two-dimensional Laplace equation is a well know special case. Curvilinear grids are used in finite difference time domain techniques FDTD [122, 123, 124] (for a covering overview see [125]) and in many other fields of numerical computation, especially fluid dynamics [126, 127]. However, in the literature on electro-magnetic calculations predominantly the Maxwell equations are considered [128, 129, 130] which greatly simplifies the covariant formulation as will be shown in the appendix B. In the general case, as for the vector wave equation, this simplification is not given and this formalism becomes more complex as will be presented here. The modelling of microwave plasma sources with their large gradients in field strengths and complex applicator shapes require such specially adopted computational grids for a sufficient numerical accuracy at reduced computation time and memory requirements. It may even be necessary to use boundary conformal grids to generate reasonable results at all [131].

It is far beyond the scope of this thesis to explain the mathematical details of the theory of differential manifolds naturally arising when considering differential equations in curvilinear coordinate systems and we would like to refer the reader to the literature as e.g. in [132, 133] or [134]. Nevertheless, a short outline containing all the necessary definitions required as well as the application to numerical computations is given in the appendix B. Here, it shall be sufficient to state the equations in covariant form; their derivation is outlined in the appendix B. The covariant form of the vector wave equation 3.31 as it applies to the problem under consideration here reads in conservative form, i.e. the Christoffel ${\Gamma^{\rho}}_{\mu\nu}$ symbols are included in the conservative derivatives, as

$$\sum_{\mu\nu} \partial_\mu \left(\frac{1}{\underline{\varepsilon}_p \sqrt{g}} g_{\mu\nu} \partial_\nu \right) \underline{\mathbf{H}}_{(\varphi)} + \sqrt{\frac{g}{g_{\varphi\varphi}}} \mu_0 \omega^2 \underline{\mathbf{H}}_{(\varphi)} = 0 \tag{3.44}$$

where we already expressed $\underline{\mathbf{H}}_{(\varphi)}$ in terms of physical components. It should be mentioned that the hermiticity of this expression is disturbed by the metric tensor $g_{\mu\nu}$ to such an extend as given by the spatial variation of these quantities (and this is determined by the grid). In a similar manner the metallic

$$\underline{\mathbf{E}}_{(0)} = -\frac{\mathrm{j}}{\omega\varepsilon_0\underline{\varepsilon}_{pl}\sqrt{g\ g_{00}}}(g_{00}\partial_{x^1}\sqrt{g_{\varphi\varphi}}\underline{\mathbf{H}}_{(\varphi)} - g_{01}\partial_{x^0}\sqrt{g_{\varphi\varphi}}\underline{\mathbf{H}}_{(\varphi)}) \qquad (3.45)$$

$$\underline{\mathbf{E}}_{(1)} = -\frac{\mathrm{j}}{\omega\varepsilon_0\underline{\varepsilon}_{pl}\sqrt{g\ g_{11}}}(g_{10}\partial_{x^1}\sqrt{g_{\varphi\varphi}}\underline{\mathbf{H}}_{(\varphi)} - g_{11}\partial_{x^0}\sqrt{g_{\varphi\varphi}}\underline{\mathbf{H}}_{(\varphi)}) \quad . \qquad (3.46)$$

and the absorbing boundary conditions

$$\partial_{x^\mu}\underline{\mathbf{H}}_{(\varphi)} \pm \frac{\mathrm{j}\omega}{\sqrt{g^{\mu\mu}}}\sqrt{\varepsilon_0\mu_0\underline{\varepsilon}_{pl}}\underline{\mathbf{H}}_{(\varphi)} = 0 \qquad (3.47)$$

can be written in covariant form.
The important point, however, is the numerical evaluation of arbitrary grid transformations with equation B.5 and equation B.10 and the covariant formulation of the vector wave equation 3.44. In addition, this is the only way to achieve second order accuracy for a second order equation as 3.44 at non-equidistant grids while keeping the finite difference expressions to the rather simple central difference form including only next neighbours.

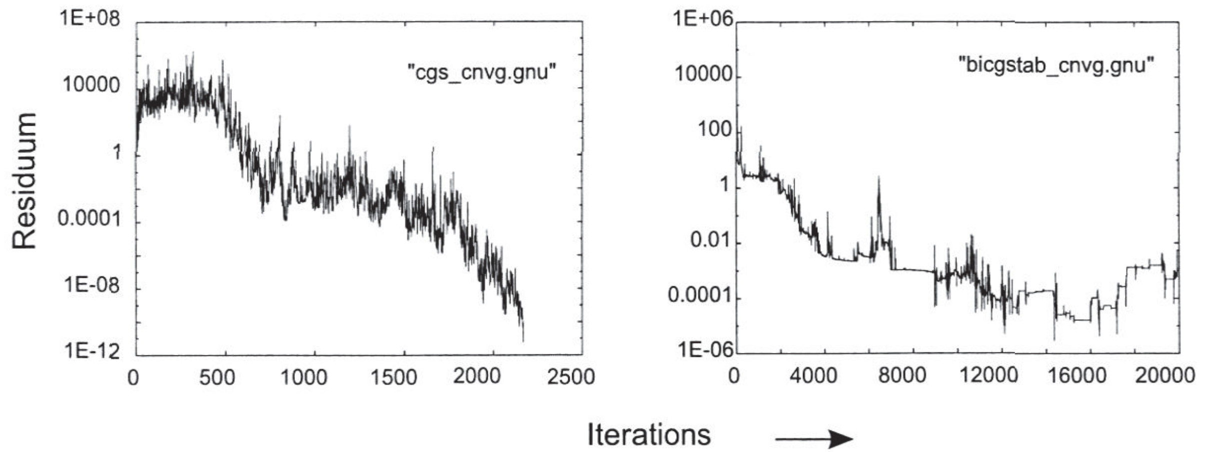

Figure 3.17.: The different convergence behaviours of the iterative solver CGS and BiCGStab for a typical FD problem on a mapped grid.

To avoid the explicit implementation of such error-prone formulas as B.19, C++ classes were written which allow a straight forward set-up of the band-matrix corresponding to the finite difference problem by providing data-structures for finite difference operators and tensors, etc. These are based on performance optimised linear algebra classes for vector-matrix operations which almost completely compensate for the known disadvantages of object oriented programming in numerical applications. The matrix equation is solved employing an optimised LU-solver [73] which turns out to be a good choice on current personal computers for grid resolutions of approximately $n \times n$ with $n \simeq 100$ points. Significantly higher resolutions are mainly constrained by $O(n^3)$ growing computation time and memory resources. In these cases iterative solvers like CGS or BiCGStab [135] are preferable. Figure 3.17 shows the convergence behaviour of these iterative solvers for a typical calculation of the MPT EM field. We use the LU-solver for a first rough calculation of the electro-magnetic field on a grid with low resolution and re-calculate with an iterative solver for higher resolutions or for changes in the permittivity of the plasma as is the case in self consistent calculations in combination with other models delivering the required permittivity distribution. All the following results are obtained at a staggered grid resolution of $N_z \otimes N_r = 800 \otimes 400$ points. From comparative calculations with $N_z \otimes N_r = 1600 \otimes 400$ and the knowledge that the error is inverse proportional to the grid resolution one can estimate the relative error ϵ_q of a quantity q to be of the order of 4 % which is quite acceptable. This follows from

$$\epsilon_q(N_1) = \frac{N_2^2(\frac{q_2}{q_1} - 1)}{N_1^2(1 - \frac{q_2 N_2^2}{q_1 N_1^2})} \tag{3.48}$$

where $q_{1,2}$ is the value of q at the respective grid resolution N_1 and N_2. The correctness of the numerical approach in principal follows from exemplary calculations of problems with known analytical solutions such as the reflection factor of a dielectric inhomogeneity in a coaxial waveguide.

3.5.4. The electromagnetic field of the MPT without a plasma

The electromagnetic field in the MPT without a plasma is calculated following the steps outlined in the previous section. This gives a very good estimation of the field strengths prior to ignition. The calculations are carried out for the matching conditions at which the MPT shows a minimum of the reflection factor $\underline{\Gamma}_l$ with an operating plasma. Here, we choose the matching conditions given by the numerical calculations in the next section rather than the experimental values since this allows

UB Dortmund

for a more direct comparison of the situations before and after ignition. In fact, the numerically extracted matching conditions, i.e. the lengths of L_T and L_S in figure 3.1, are in good agreement with the experimental ones except a systematic underestimation of L_S due to the fringe fields at the in-coupling as pointed out in section 3.2. The equations to be solved follow from the ones in section 3.5.1 by letting $\underline{\varepsilon}_{pl} = 1$.

As can be assumed from figure 3.18 there is hardly any radiation of electro-magnetic energy without an operating plasma. Integrating the Poynting vector along the surface of a cylinder as indicated in figure 3.16 shows that at 100 W forward power less than 3 W is radiated into the surrounding. There are high electric fields with a maximum of almost 200 kV m^{-1} (time averaged absolute value for 100 W forward power) strongly located at the outer corner of the inner conductor which decrease by an order of magnitude when moving towards the symmetry axis. This number has to be taken with care since the electric field at this corner point is expected to be divergent. Actually, in the case of electrostatic calculations this divergence is know to vary as $(\sqrt[6]{r^2 + z^2})^{-1}$ [117] where $\sqrt{r^2 + z^2}$ is the distance from the corner. One might take the numerical value as an average over the cell area since the finite difference formulation could also be derived from a finite integration approach. There is also a back-propagation of an electro-magnetic wave into the gas channel which is an order of magnitude smaller than the TEM wave in the coaxial section of the MPT.

3.5.5. Electromagnetic characteristics of the MPT after ignition of a plasma

While the MPT operates as a $^3\!/\!_4\,\lambda$ resonator whose quality factor is determined by metal losses and the amount of radiated microwave energy prior to ignition of a plasma the situation completely changes ones the plasma is ignited. Then, the quality factor becomes rather low so that a resonator approach does not seem to be of any use and a description in terms of an impedance matching network as outlined in section 3.2.1 is much more reasonable. Within this description, the plasma is represented by a complex dielectric constant and the MPT has to match this to the characteristic wave impedance, typically 50 Ω, to the power feeding coaxial cable. Only the spatial dielectric distribution has to be determined in some way.

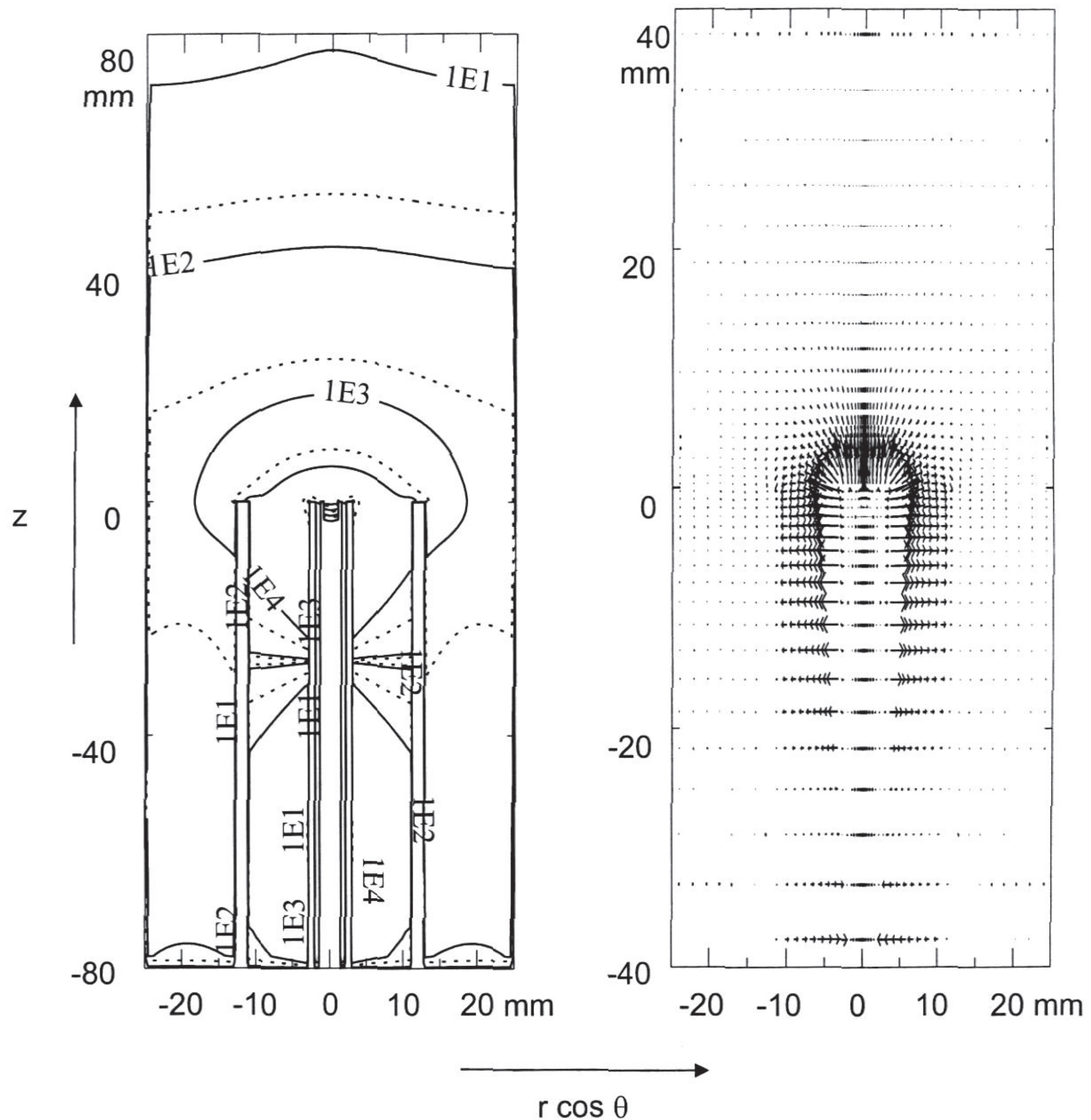

Figure 3.18.: Contour (left) and vector (right) plot of the electrical field in the MPT without an operating plasma. The highest field strengths are localised around the outer corner of the inner conductor with approximately 200 kV m^{-1}. *There is almost no microwave radiation leaving the plasma source. An integration of the Poynting vector around the computation domain boundary delivers a total radiated power of less than* 3 W. *The contour lines are scaled logarithmically; this applies to all following figures.*

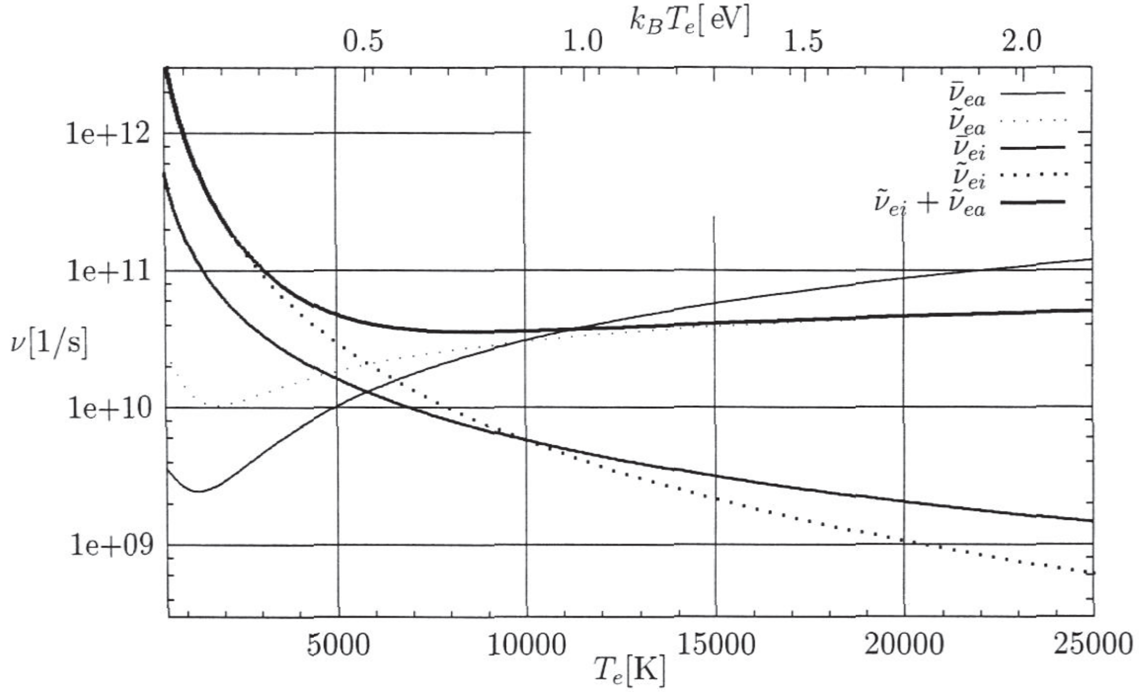

Figure 3.19.: Electron-ion- ($\bar{\nu}_{ei}$) and electron-atom-collision frequency ($\bar{\nu}_{ea}$) for elastic momentum transfer. The frequencies are proportional to n_i and n_a, respectively. Here, $n_i = 2 \cdot 10^{20}\, m^{-3}$, $n_a = 2 \cdot 10^{24}\, m^{-3}$ ($\hat{=}$ 3600 K) $\Rightarrow \alpha = 10^{-4}$ are assumed. In addition, $\tilde{\nu}_{ea}$ and $\tilde{\nu}_{ei}$ (dotted lines) are plotted with variable n_a from the ideal gas-law (see text) and $n_i = \alpha n_a$. The sum of $\tilde{\nu}_{ea} + \tilde{\nu}_{ei}$ is only weakly dependent on T_e between 5000 K *and* 25000 K *for constant pressure and ionisation degree α.*

The complex ϵ_r plasma model and the fit to Thomson scattering

This could in principle be constructed from experimental data like those obtained from Thomson scattering delivering the electron density and temperature distribution within the plasma as outlined in section 3.3. Equation 3.25 gives the plasma dielectric constant as a function of the average electron-neutral collision frequency ν for momentum transfer and the electron density n_e.

Here we will employ a rather simple model to estimate the effective collision frequency ν. Benoy [12, chapter 6.2] calculates the expression

$$Q_{eh} = Q_{ei} + Q_{ea} = n_e \sum_{s=i,a} \frac{2m_e}{m_s} \frac{3}{2} k_B (T_e - T_s) \bar{\nu}_{es} \tag{3.49}$$

for the energy transfer from electrons to heavy particles, where $\bar{\nu}_{ei}$ and $\bar{\nu}_{ea}$ are the average collision frequencies for momentum transfer between electron-ion and electron-atom collisions, respectively. There, $\bar{\nu}_{ei}$ is cited from [136] while $\bar{\nu}_{ea}$ is

obtained by a fit from experimental data [137]:

$$\bar{\nu}_{ei} = \frac{4\sqrt{2\pi}}{3}\left(\frac{e^2}{4\pi\varepsilon_0 m_e}\right)^2\left(\frac{m_e}{k_B T_e}\right)^{3/2} n_i \ln\Lambda \tag{3.50}$$

$$\bar{\nu}_{ea} = \sqrt{\frac{8k_B T_e}{\pi m_e}} n_a \left[\frac{5\cdot 10^{-20}}{(1+1.7\cdot 10^{-3}T_e)^2} - 3\cdot 10^{-21} + 2.8\cdot 10^{-24}T_e - 4.1\cdot 10^{-34}T_e^3\right] \tag{3.51}$$

$\ln\Lambda$ is the Coulomb-logarithm, which can be approximated by $\ln\Lambda \simeq 8$. The electron temperature has to be taken in Kelvin and $\bar{\nu}_{ea}$ is then given in units of $1/\mathrm{s}$. The dependency of the collision frequencies on the electron temperature T_e is shown in figure 3.19. For the assumed particle density the energy transfer to the atoms becomes more effective than to the ions above a temperature of 6000 K. The assumed neutral particle density $n_a = 2\,10^{24}$ m $^{-3}$ follows from the ideal gas law at a temperature of $T_h = 3600$ K (this average value follows from measurements as described in section 3.4).
Figure 3.19 contains two additional plots, $\tilde{\nu}_{ei}$ and $\tilde{\nu}_{ea}$. These follow from the assumption that the heavy particle temperature equals one third of the electron temperature exceeding 500 K, $T_h = 500$ K $+ (T_e - 500$ K$)/3$. Neglecting partial pressures of electrons and ions, it follows from the ideal gas law that $n_a = p/k_B T_h$. For the temperature independent ion density the same ionisation degree $\alpha = 10^{-4}$ is assumed. For $k_B T_e = 1.5$ eV ($\hat{=}\,17400$ K) it follows that

$$\nu = \tilde{\nu}_{ei} + \tilde{\nu}_{ea} = 4.6\cdot 10^{10}\frac{1}{s} \quad . \tag{3.52}$$

This value for the average electron-heavy particle collision frequency will be used throughout all numerical calculations unless stated otherwise. Unfortunately, the Thomson scattering method used here does not supply a sufficient spatial resolution for an adequate description of the plasma. To overcome this problem, an empirical formula with a set of five parameters is employed to approximate the electron density as a function of the coordinates z and r:

$$\begin{aligned} n_e(z,r) &= n_e^{max} a(z)\, \mathrm{e}^{-\left(\frac{r-d(z)}{b(z)}\right)^2} \\ a(z) &= \mathrm{e}^{-\frac{(z-z_0)^2}{h^2}} \\ d(z) &= -\frac{d_0}{z_0}z + d_0 \\ b(z) &= \frac{b_0-b_1}{z_0^2}(z-z_0)^2 + b_1 \end{aligned} \tag{3.53}$$

The five parameters z_0, d_0, b_0, b_1, h are fitted to the Thomson data by a non-linear

Levenberg-Marqaurdt algorithm. This can be done with a very low residual χ^2 value of typically 10^{-30}. Thus, the interpolation of the Thomson data is done with a very high confidence level and the extrapolation at least close to the measurement domain can be assumed to be adequate. Fitting this function to the Thomson data for the MPT standard conditions (100 W forward power, 500 mL min^{-1} and 200 mL min^{-1} Ar gas flow in the analyte and plasma gas channel, respectively) yields the following set of parameters

z_0	d_0	b_0	b_1	h
7 mm	2 mm	3.63 mm	0.5 mm	5 mm

Figure 3.20 shows a density plot of the analytical electron distribution function with the above parameters. It obviously reflects the optical appearance of a typical MPT generated plasma. The following electromagnetic calculations are based on this function with the stated parameter set.

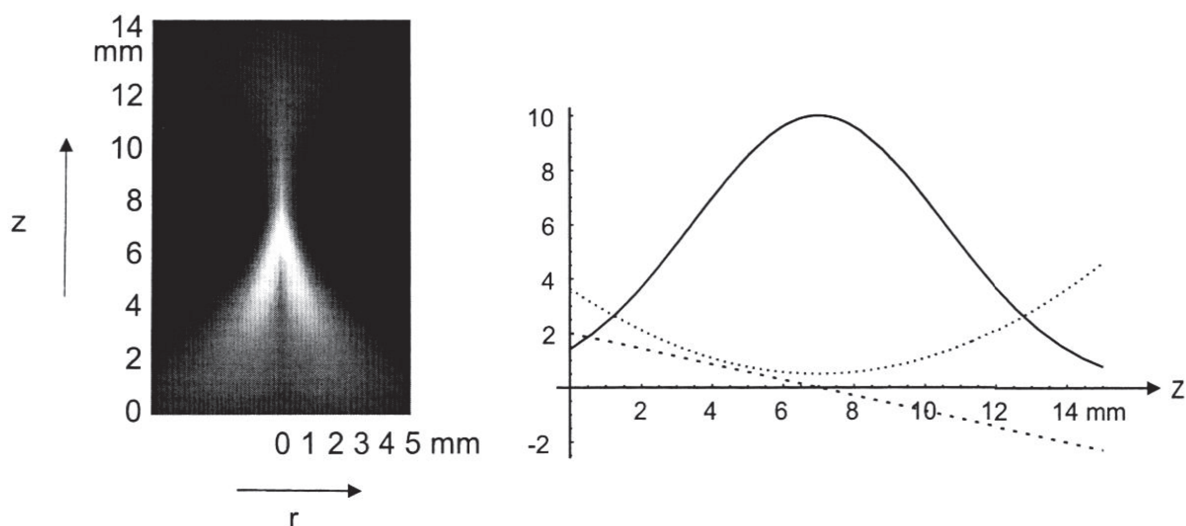

Figure 3.20.: Analytical function to describe the electron density distribution of the MPT plasma. The parameter of the function are fitted to Thomson scattering data and reproduce the experimental values within the measurement domain with high accuracy. On the left side a density plot of the assumed electron density is shown, the right plots show the variation of some sub-functions of the analytical electron density approximation with the hight z above the torch: solid line $a(z)$, dotted line $b(z)$ and dashed lined $d(z)$.

Electromagnetic fields

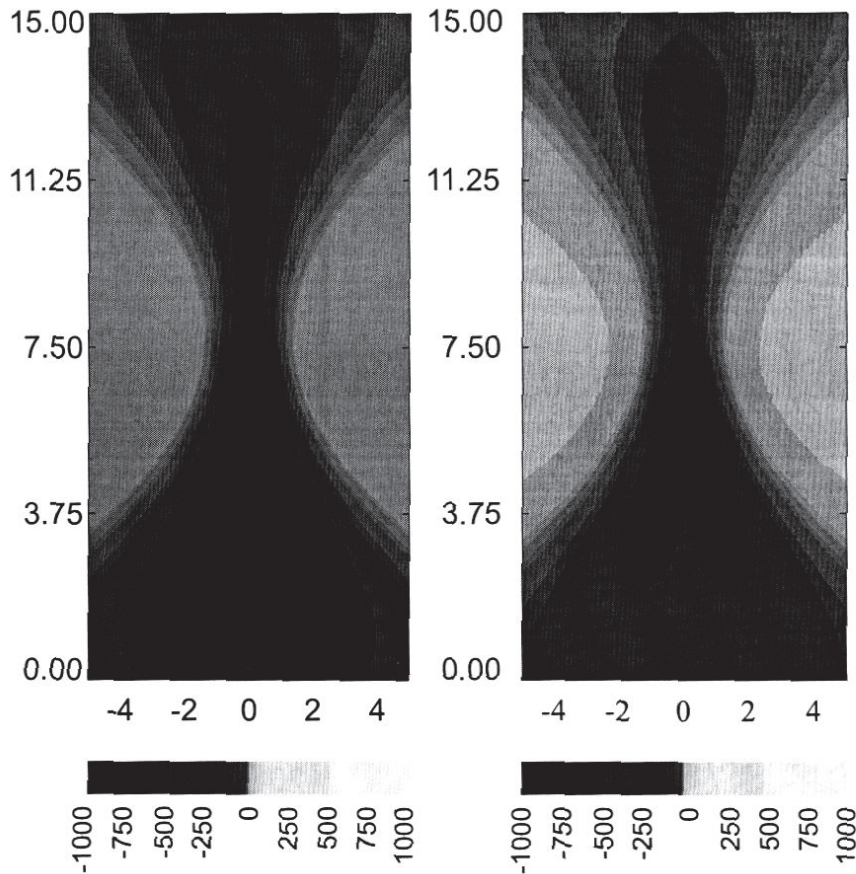

Figure 3.21.: Contour plot of the real part (right) and imaginary part (left) of the complex plasma dielectric constant. The corresponding specific conductivity distribution σ_{pl} follows from multiplying the shown values by the factor $\varepsilon_0\omega \approx 1/7.3\,(\Omega\ \mathrm{m})^{-1}$. The contour lines are scaled logarithmically; this applies to all following figures.

Employing a simple single electron model the above electron density distribution and effective collision frequency leads to a complex $\underline{\varepsilon}_r$ distribution as shown in figure 3.21 though expression 3.25. The corresponding specific conductivity distribution σ_{pl} follows from multiplying by the factor $\varepsilon_0\omega \approx 1/7.3\,(\Omega m)^{-1}$. Choosing matching conditions, i.e. setting the lengths L_T and L_S as described in figure 3.1 to appropriate values, the electromagnetic calculations supply information about the effective plasma reflection factor $\underline{\Gamma}_{pl}$, the electromagnetic fields ($\underline{\mathbf{H}}, \underline{\mathbf{E}}$) and the power absorption P_A and radiation $\underline{\mathbf{S}}$. At the end of this section a table is given to summarize the most important results.

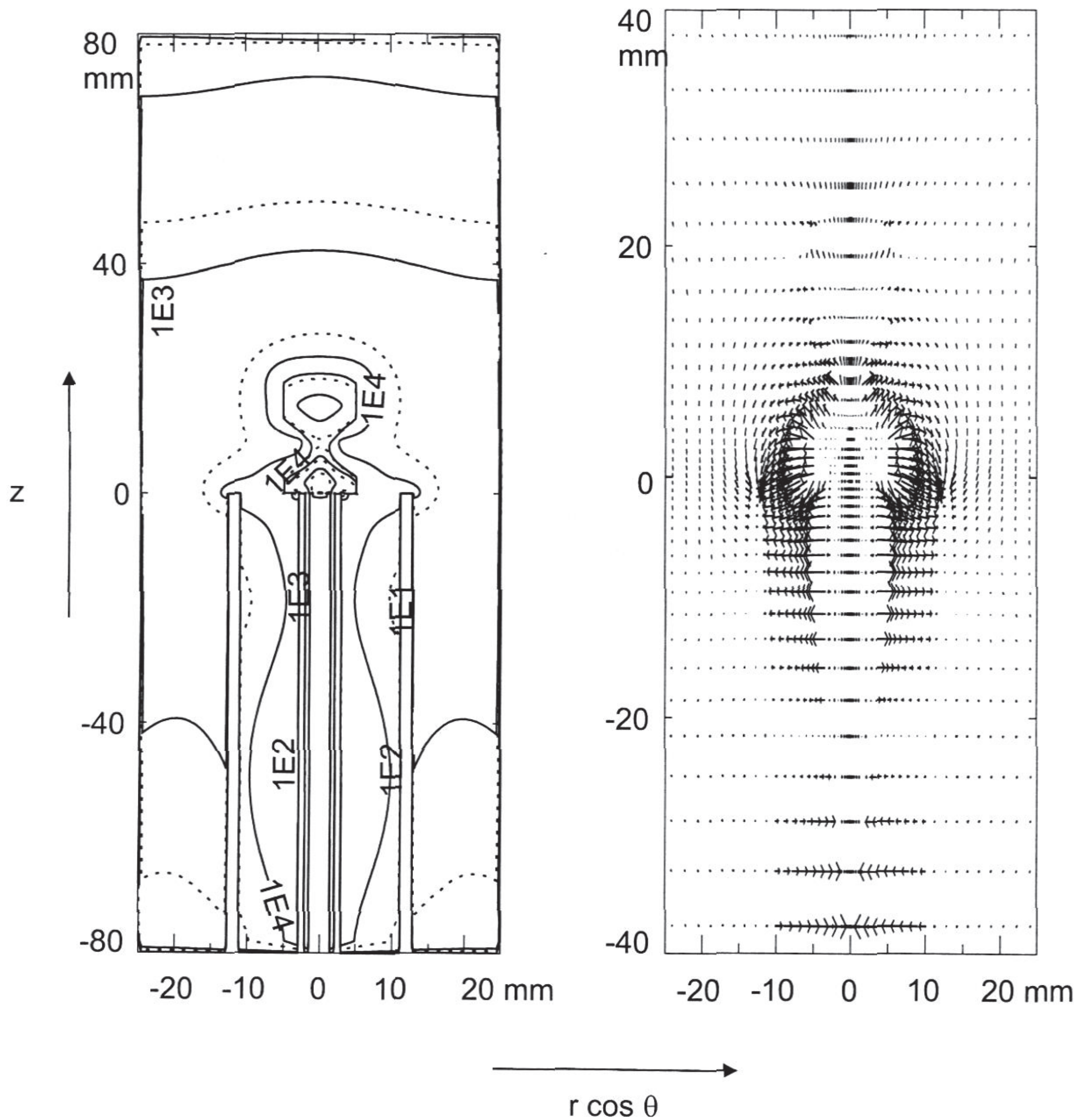

Figure 3.22.: Contour (left, time averaged absolute value) and vector (right, temporal snapshot) plot of the electric field in the MPT with an operating plasma. The highest field strengths are localized around the lower outer boundary of the plasma just above the torch with approximately 60 kV m^{-1}.

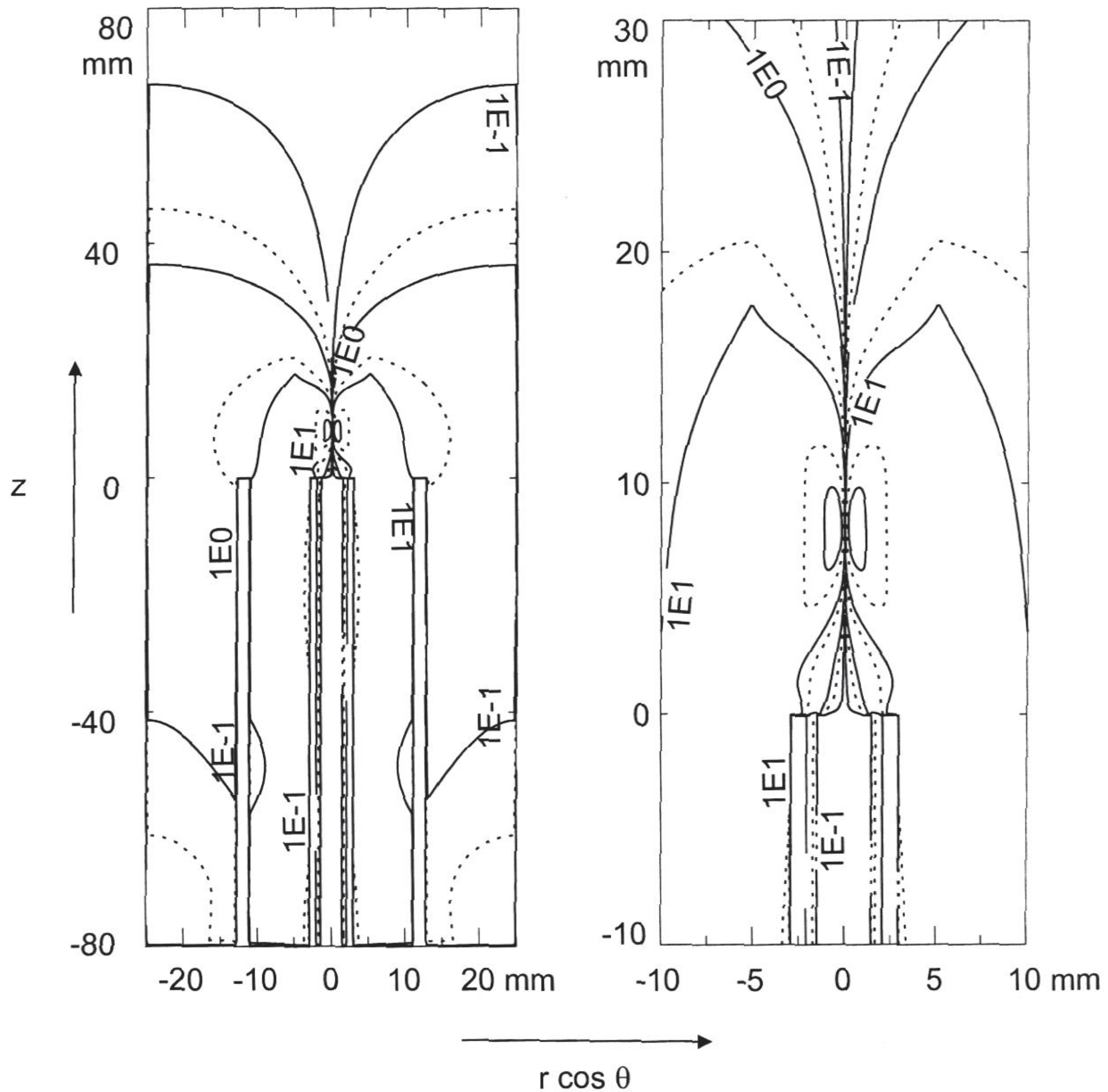

Figure 3.23.: Contour plot of the time averaged magnetic field $\mathbf{H}_\varphi$ of the MPT plasma in the full computation domain (left) and a magnified section showing the plasma region (right). The plots show that the plasma is confined by strong induced currents especially around the small spot of high electron density (hot spot).

Figure 3.22 shows a contour plot of the time averaged absolute values of the electric field strength (left) and a vector plot of the real part of electric field phasor $Re[\underline{\mathbf{E}}]$ which represents a momentary snapshot.One clearly observes a propagation of the electro-magnetic field up to the point of highest electron density approximately 7 mm above the torch ("hot spot"). It rapidly decays beyond this point. The electric field lines wrap around the plasma and only marginally penetrate into the outer plasma sheath due to the vast growth in conductivity when moving inside the plasma. The contour lines of the time averaged magnetic field $\mathbf{H}_\varphi$ are shown in figure 3.23. The reader should consider that the magnetic field has just a ϕ-component and is perpendicular to the shown (z, r)-plane. In contrast to the situation without a plasma, here the field lines reach far more into the MPT surrounding and suggest the operation of the plasma as a microwave antenna launching electromagnetic waves.

Power density and power flow

The finite difference calculation provide also insight into the energy flow and energy in-coupling processes in the MPT plasma, quantities which are quite complicate to measure. The energy flow is basically given by the real part of the complex Poynting vector $\underline{\mathbf{S}}$. Figure 3.24 shows two plot of $\underline{\mathbf{S}}$ at different scales. The left plot shows the whole computation domain and one easily recognizes the energy flow along the upper coaxial section of the MPT into the plasma. The right plot shows a magnification of the plasma region. Here, one can observe that the energy flows mainly into the plasma at heights below the "hot spot" but that at heights exceeding this point the microwave energy is radiated into the surrounding area. Indeed, integrating the Poynting vector along a volume enclosing the plasma shows that approximately 55 W (for details see table at the end of this section) is radiated and thus security and electromagnetic compatibility considerations have to be provided in applications.

Another important quantity is the power density distribution as shown in figures 3.25 and 3.26. It is the main coupling factor to fluid-dynamic simulations because it can be used to represent the local heating in the gas flow. As can be seen the highest values are reached at the "hot spot" inside the plasma rapidly decreasing towards the plasma boundaries. Only at the lower corners a comparable smooth increasing of the power density is observable, especially in the colour plot 3.26. These were supposed to be the main power in-coupling regions in former calculations [64] due to neglecting the matching characteristics of the MPT. These are treated in a proper way now as outlined in section 3.5.

Figure 3.26 also very clearly shows the so called hollow structure of the MPT plasma,

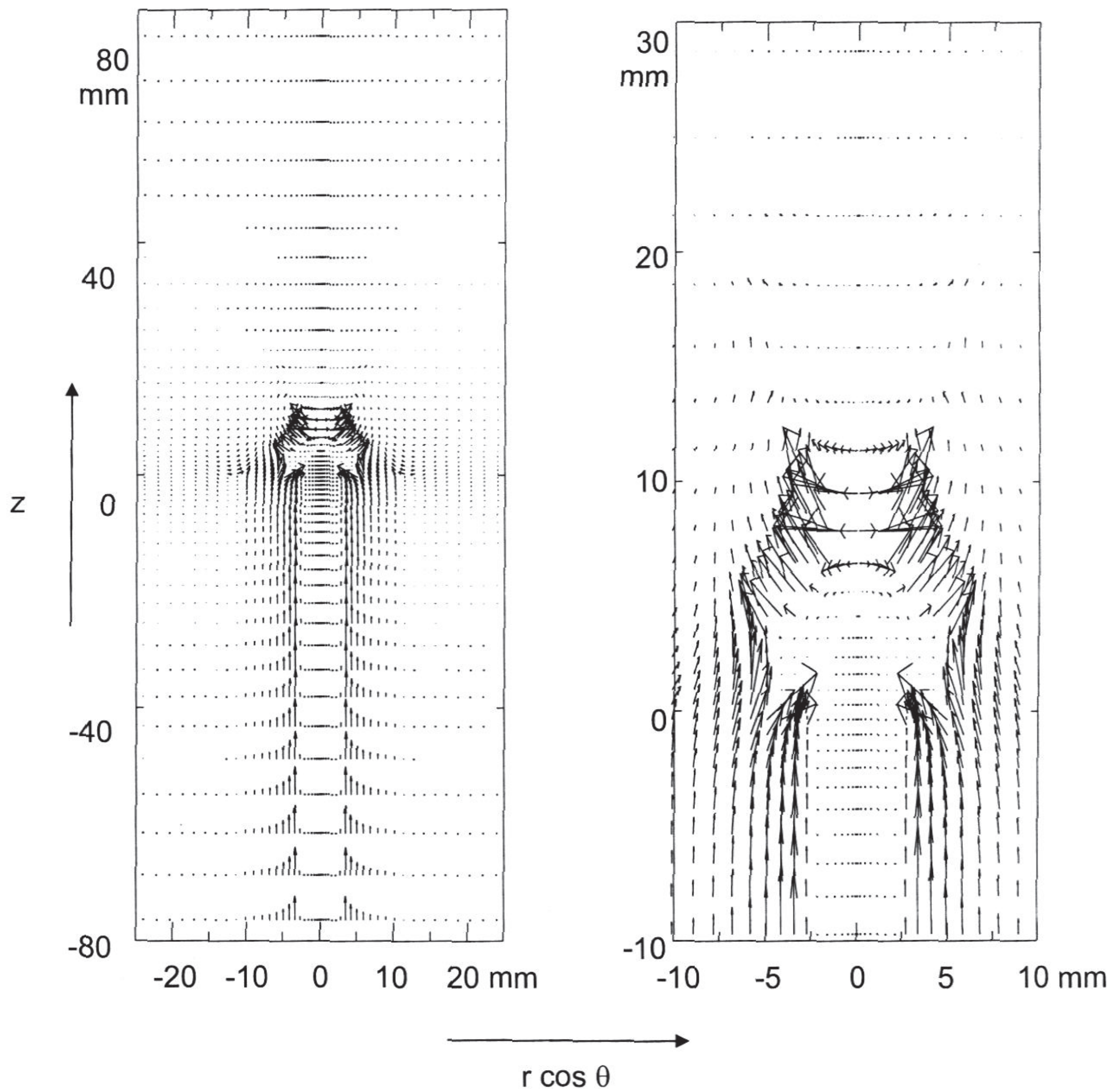

Figure 3.24.: Contour plot of the real part of the complex Poynting vector. The left plot shows the whole computation domain while the right plot shows a magnification of the plasma region. Integrating the Poynting vector along a volume enclosing the plasma shows that approximately 55 W *is radiated into the surrounding.*

Finite Difference Results Summary

	L_T [mm]	L_S [mm]	$\underline{Z}'_P$ (L_T) [Ω]	$\underline{\Gamma}_{pl}(L_T)$	$\underline{\Gamma}_{in}(L_T)$
impedance transformation	73.7	18.6	$40.8 - j\ 19.7$	$-0.277 - j\ 0.212$	$0.0034 - j\ 0.012$
	$\langle\lvert\underline{\mathbf{E}}\rvert\rangle_{max}\rvert_{(z,r)=(0,5)[mm]}$			$\langle\lvert\underline{\mathbf{H}}\rvert\rangle_{max}\rvert_{(z,r)=(8,0.5)[\text{ mm}]}$	
EM fields	60.5 kV m $^{-1}$			152.6 A m $^{-1}$	
	P_{in} [W]	P_A [W]	$P_{out}\rvert_{\partial V^N}$ [W]	$P_{out}\rvert_{\partial V^E}$ [W]	$P_{out}\rvert_{\partial V^S}$ [W]
power	101	46	0.3	16.7	37.9
$\sum_{\partial V} P_{out}$	54.9 W				

Table 3.1.: Some finite difference calculation results of the electromagnetic field of the MPT grouped in impedance transformation, field strengths and power.

i.e. a region of low energy density inside the lower (ionizing) part of the toroidal plasma. It is supposed that this structure is one of the reasons of the MPT's stability against aerosol loading in the analyte channel [32]. The aerosol passes a hot plasma sheath from the inside without significantly disturbing the energy in-coupling of the microwave along the outer sheath. Then it has to pass the "hot spot" of highest energy density resulting in a good atomisation performance of the MPT. These calculations also explain the measured electron density distribution, see section 3.3, and answer the questions why the highest electron densities are found 7 mm above the torch; it is a result of the strongly attenuated electromagnetic wave propagation along the plasma sheath. Assuming the highest electron densities at this point as a calculation input result in highest power densities there as to be expected from basic theory; thus the calculations are self-consistent.

3.6. Fluid-dynamic simulations of the MPT

In a first approach the Ar plasma can be looked at as a hot Ar gas stream with a spatial inhomogeneous energy in-coupling, i.e. an additional term in the energy equation of the fluid. This is the simplest and primary interface for fluid dynamic and electromagnetic simulations. The necessary quantities for the electrodynamic

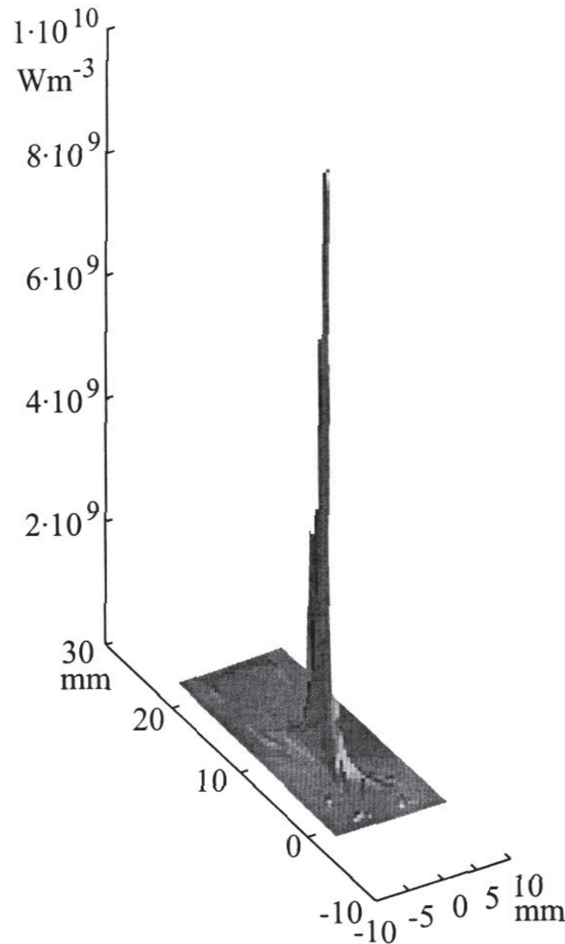

Figure 3.25.: Contour (left) and hill (right) plot of the power density in the MPT plasma. The highest values are reached at the "hot spot" inside the plasma 7 mm *above the torch ending rapidly decreasing towards the plasma boundaries. The hill plot clearly shows the extreme gradients in the power density distribution.*

calculations such as the electron density and the effective collision frequency have to be estimated from the fluid dynamic results like the density and temperature field via semi empirical formulas. A new electromagnetic simulation run delivers a new energy field for the fluid dynamic calculations in turn and thus closes the loop. Practically, one has to consider how this coupling can be carried out. Either an interpolation procedure has to be carried out between the different grids used or the same grid has to be used for both simulation programmes. This poses very strong restrictions on commercial software and is one of the major reason to prefer hand written code for either problem. Here, for the fluid dynamic calculations a commercial programme is chosen (FLUENT) and the electromagnetic part is implemented in C++ with the aid of a sophisticated class library for linear algebra and curvilinear finite differences.

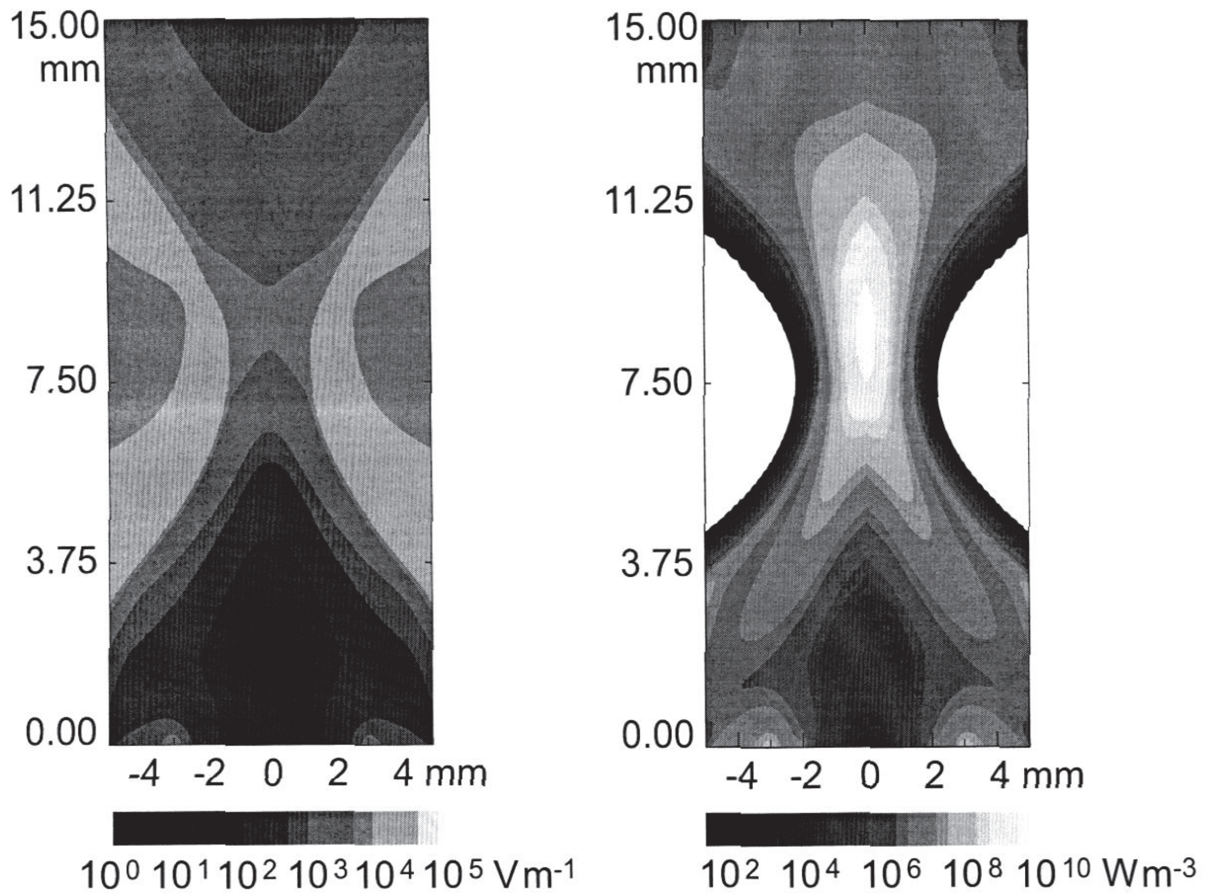

Figure 3.26.: Coloured contours of the power density P_A (right) and the time averaged electric field strength $\langle|\mathbf{E}|\rangle$ (left) in the MPT plasma. The colour gradients are scaled logarithmically to represent a broad range of values which can be depicted from the colour lookup table below the plot. This figure also very clearly shows the so called hollow structure of the MPT plasma, i.e. a region of low energy density inside the lower part of the toroidal plasma.

These allow the adaption of a structured mapped grid from external sources and thus simplify the interaction of both codes. Unfortunately, the interface from the viewpoint of the commercial code proved to be far from easy to construct so that only preliminary results for some de-coupled simulations are presented in figure 3.27. However, already with this simply energy incoupling mechanism, one readily observes some characteristics of the flow pattern typical for the MPT plasma as the broadening of the plasma plume region and the stabilising swirls left and right to the smallest area of the flow pattern just above the gas outlet. More elaborated simulations e.g. via employing the facilities of so called user defined functions (UDF) of FLUENT may allow for a much more detailed analysis of the flow pattern.

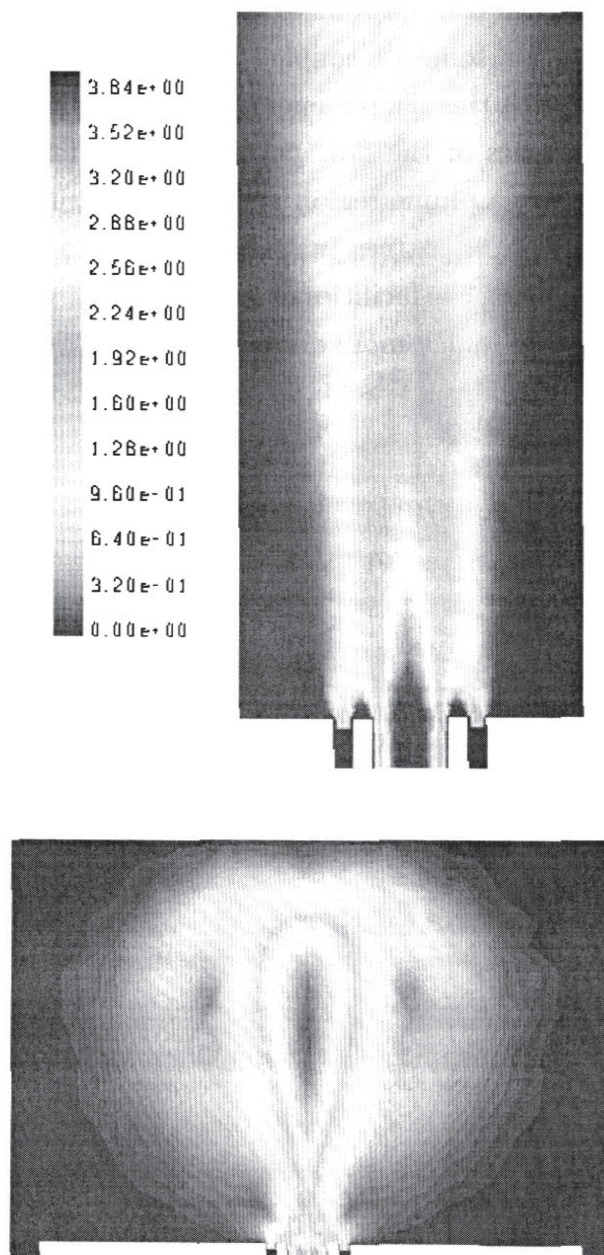

Figure 3.27.: Two exemplary calculations of the Ar *gas flow of the MPT performed with a commercial code (FLUENT). The upper picture shows the magnitude of the velocity field in* $\mathrm{m\ s^{-1}}$ *of a cold (*300 K*)* Ar *gas flow at standard conditions. The lower one includes an localized volumetric energy in-coupling of* $10^{10}\ \mathrm{W\ m^{-3}}$ *over a torus above the inner conductor; velocity magnitudes have to be scaled by the factor* 2.

4. Microstrip Plasma Sources

4.1. Introduction

In analytical chemistry the trends to miniaturise parts or whole chemical analysis systems nowadays are very important [142]. The upcoming of the so called "micro Total Analysis Systems" (μTAS) had its greatest push during the late eighties [143, 8]. It stands for the miniaturisation of one or several components needed for a chemical analysis as pumps[144], valves and reaction chambers[143], detectors[145] or separation techniques [146]. This reduction in size inherits several advantages as it leads to a reduced consumption of reagents and production of waste simultaneously enabling faster analysis due to reduced transport lengths and a potential better optimisations of mass transport for chemical reactions and separations. Further-on, less sample volume is required and the system may be constructed portable being important e.g. for monitoring environmental relevant elements and compounds directly at their sources of origin [145, 142].
The application of micro-structuring processes like photolithography and etching as used in the semiconductor industry [147] would allow for the complete integration of analysis systems on a single chip. For this purpose several substrates depending on the specific application like glass, fused silica or silicon could be used as well as polymers [143, 147]. The latter allow for a very simple and cost efficient mass production employing processes like LIGA ("Lithographie", "Galvanik", "Abformung") developed at the Forschungszentrum Karlsruhe [148, 149] or SIGA ("Silizium-Mikrostruktur", "Galvanik", "Abformung") developed at the University of Dortmund [150, 151, 152]. The first complete μTAS system was a GC on silicon wafer published by Terry et al. in 1979 [153] but it has met with no response until this field experienced a strong revival and rapid developments took place [154]. Today, many μTAS components are available [155, 156] like liquid chromatography or capillary electrophoresis.

The essence of this chapter has been published and legally protected in [138, 139, 140, 141]

A still missing component is an element-specific detector as e.g. a plasma. This gap was first bridged by Eijkel et at. in 1999 with the development of a miniaturised direct current (DC) plasma in He on a chip [157]. This was used for the determination of CH_4 though detection of an emission band of the CH radical. A great advantage of this method is the possible application of this plasma as a detector for GC. But it also suffers from a major drawback; a DC plasma intrinsically requires a direct contact of the plasma with the electrodes resulting in a more or less rapid destruction of these, in the specific plasma source cited here the life time is limited to two hours. An electrodeless microwave induced plasma source would overcome this problem. Its development and construction for diverse applications as in [139, 140, 141] is subject of this chapter.

4.2. Development and fabrication of microstrip plasma sources (MSPs)

Beginning from first experimental set-ups basing on PTFE substrates it was clear that a microwave induced plasma source can be constructed from microstrips. Microstrips belong to the group of planar transmission lines, see [72] for thorough introduction. It consists of a single conducting strip of width w placed on a dielectric substrate of thickness h and located on a ground plane as shows in figure 4.1. In most applications the microstrip transmission lines can be fabricated using conventional printed-circuit-board techniques which result in good mechanical tolerances and low cost. A commonly used substrate material is polytetraflouroethylene (PTFE) which has a dielectric constant of $\varepsilon_r = 2.1$ and a loss tangent of $tan\delta_\varepsilon = 0.0005$ at microwave frequencies [72]. But also ceramic materials like Al_2O_3 and BN as well as sapphire are used for substrates. And these materials also find application in the MSP construction due to their chemical resistance and high temperature stability as required for a plasma operation.

The fundamental mode of wave propagation in a microstrip line is not a pure TEM mode as a consequence of the inhomogeneous dielectric surrounding. This complicates an analytical analysis considerably and only within the low-frequency approximation this is possible at all e.g. by the Method of Moments [72]. But for frequencies below several GHz for practical microstrip lines where the typical lengths are several mm the wave propagation proceeds in a quasi-TEM mode. Then the typical transmission line parameters like the characteristic wave impedance Z_c and the propagation constant which is connected to the effective dielectric constant ε_e

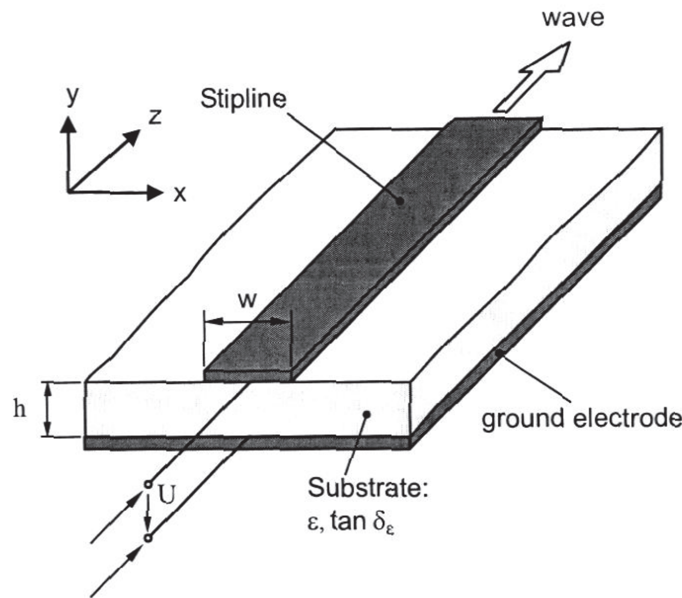

Figure 4.1.: Schematic drawing of a microstrip line on a substrate with dielectric constant ε_r and loss tangent δ_{ε_r}.

via

$$\beta = \sqrt{\varepsilon_e}\frac{2\pi}{\lambda_0} \tag{4.1}$$

can be obtained from numerical electrostatic calculations for any exotic cross-sectional form of the microstrip line. For this the electrostatic equation

$$\left(\nabla \cdot \underline{\varepsilon}_r \nabla \underline{\phi}\right) = 0 \tag{4.2}$$

with an in general complex potential function $\underline{\phi}$ and arbitrary boundary conditions, e.g. 1 V at strip and 0 V at ground as in figure 4.1, has to be solved. The electric field follows from

$$\underline{\mathbf{E}} = -\nabla \underline{\phi} \tag{4.3}$$

which in turn can be used to calculate the distributed capacity C_{ε_r} from

$$C_{\underline{\varepsilon}_r} = \frac{\varepsilon_r'}{\underline{V_0}\underline{V_0}^\star} \int_S \left(\underline{\mathbf{E}} \cdot \underline{\mathbf{E}}^\star\right) \mathrm{d}S \tag{4.4}$$

with $\varepsilon_r' = Re[\underline{\varepsilon}_r]$. This directly yields the characteristic wave impedance

$$Z_c = \frac{1}{c_0}\sqrt{C_{\underline{\varepsilon}_r} C_{air}} \tag{4.5}$$

where c_0 is the speed of light in vacuo and C_{air} the distributed capacitance of the air-filled line. It follows for the effective dielectric constant that

$$\varepsilon_e = \frac{C_{\underline{\varepsilon}_r}}{C_{air}} \quad . \tag{4.6}$$

With this approach the microstrip line my be treated as a TEM transmission line and can be analysed with the methods as outlined for the MPT in chapter 3. The real potential difference between the strip and the ground plane can then be calculated from

$$U = \sqrt{2PZ_c} \tag{4.7}$$

in dependence on the microwave power P.

4.2.1. Substrate processing

The Microstrip Plasma Source (MSP) basically consists of a planar microstrip line on a ceramic dielectric substrate and a massive copper plate which serves as a heat sink and where necessary as the ground electrode. The plasma-gas channel(s) are inside the dielectric substrate below the microstrip line. The plasma is encapsulated within the ceramic wafer not being affected and contaminated by the surrounding atmosphere. Plasma-wall interactions do not seem to play a prominent role provided the plasma gas flow does not drop below a critical value of some 10 $\mathrm{mL\,min^{-1}}$. The general approach to form these structured substrates is to build a sandwich of two ceramic plates in one or both of which the desired grooves are fabricated by an appropriate micro structuring process. Water-glass proved to be an ideal glue to fix the plates together. Careful handling is necessary in order not to contaminate the formed grooves with this glue. Another option is to use ceramic wafer with an already existing channel. Both possibilities are realized and MSP designs employing them are presented in the following sections.

4.2.2. Microstrip design and structuring

The microstrip design bases on experimental investigations and experience since no complete self consistent model for the simulation of the MSP exists. It bases on the same principles as outlined in chapter 3 for the MPT. The basic circuit consists of an open ended stripline of a length of approximately $\lambda/2$ under which the plasma is operated, a perpendicular coupling line and an open stub matching line. The exact arrangement depends on the required features of the MSP.

The fabrication of the metallic conductors is performed by a standard multi-step photolithographic process for integrated microwave circuits. First, the ceramic wafer is sputtered with a several 100 nm titanium adhesion layer. This is covered with the actual conducting copper layer of several μm thickness. This layer may be electro-plated to several 10 μm thickness depending on the specific application. From the

point of view of electromagnetic wave propagation same μm are sufficient since the skin depth of copper at 2.45 GHz is only $\approx 1.3\,\mu$m. The striplines are then delineated by a standard photolithographic process involving wet etching of the copper layer with $Na_2S_2O_8$ solution and removal of the titanium layer by diluted HF. An electro-plated golden protection layer proved to significantly enhance the life time of the MSP.

4.2.3. Electromagnetic modelling

One of the main features for sustaining a plasma is the electric field distribution in the gas channel. Apart from the applied microwave power, the geometrical set-up of the microstrip and the gas channel determine the electric field.
To estimate the applied voltage at the transmission line, one might assume that the electro-magnetic wave propagates as a quasi-TEM mode [72] as outlined in the previous sections. Then the voltage can be readily calculated between the two conductors from an assumed wave impedance of $Z_0 \cong 50\ \Omega$ and an applied power $P = 10$ W to be $U_0 \approx 32$ V. In this sense a numerical analysis of the influence of differently shaped gas channels on the electric field in the channel can be performed. Figure 4.2 shows the variation of the electric field along the $x = 0$ axis, i.e. the vertical symmetry axis, within the gas channel for a voltage of 1 V in fused silica wafer. One readily notes the advantage of a flat channel giving the highest relative fields. For comparison, a plot with the 'flat channel' configuration on a Al_2O_3 ceramic substrate is also included; here, the electric field is even more enhanced in the channel due to the larger step in relative dielectricity ($\varepsilon_r = 10$, in contrast to $\varepsilon_r = 3.5$ for fused silica).

One recognises that for $P = 10$ W we can expect electric fields of only about 240 V cm^{-1} occurring within the channel. This field strength is much too low to ignite the plasma. A stripline with a high Z_c-value would enhance the field strength as well as ceramic substrate with a high dielectric constant.

4.2.4. Fluid flow modelling

In order to gain insight in the gas flow patterns and the heat distribution inside the gas channel of the MSP several fluid dynamic calculations are carried out with an additional source term in the energy equation accounting for the microwave energy in-coupling to the plasma. This energy term is assumed to be spatially homogeneous and amounts to the total in-coupled microwave power over a length of

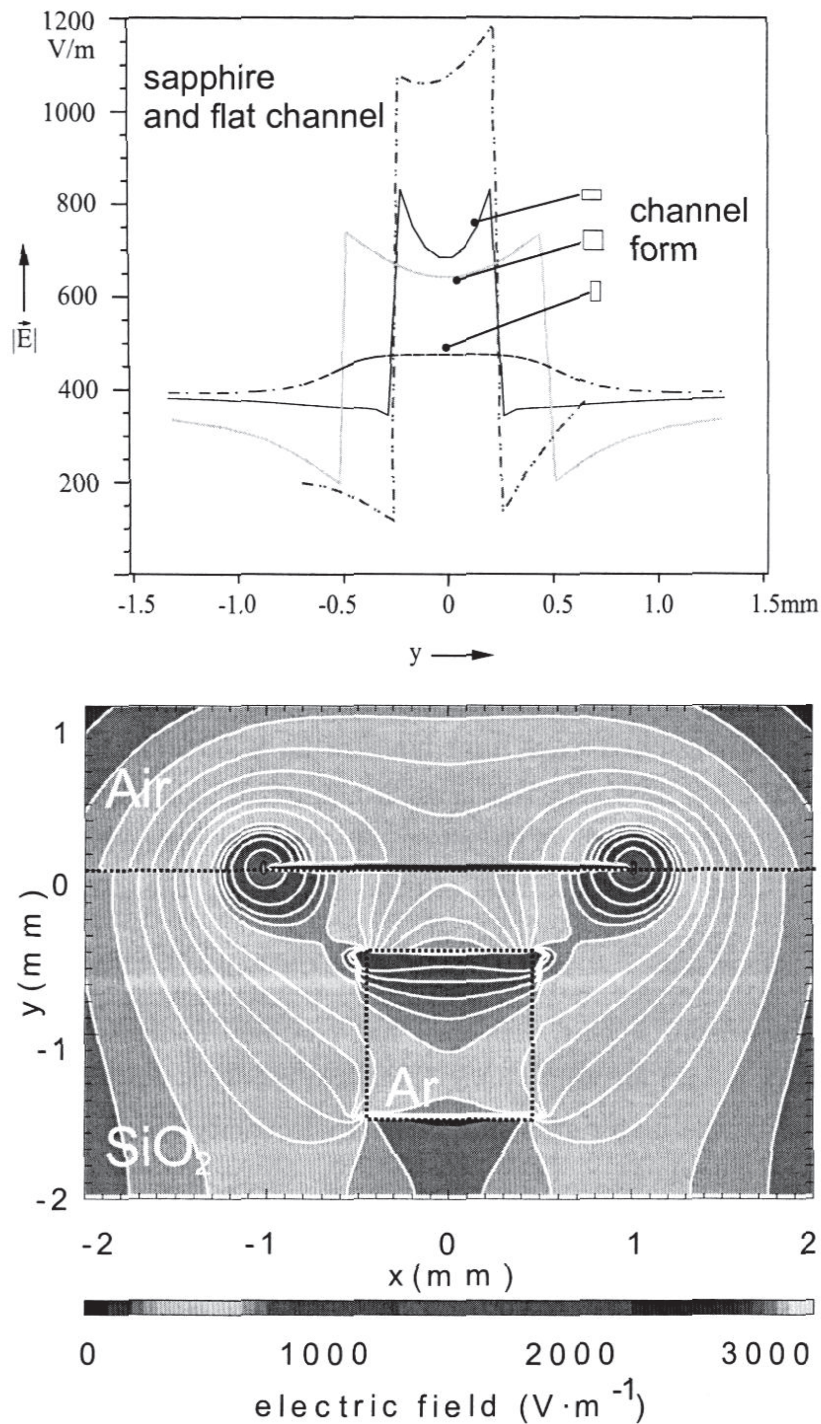

Figure 4.2.: Electrostatic field of an MSP based on fused silica. The upper graph shows the electric field along the $x = 0$ (symmetry) axis for differently shaped gas channels. The applied voltage for all electrostatic calculations is 1 V. Obviously, the flat horizontally oriented form, i.e. along the x-axis is most favourable for highest field strengths in the channel. For comparison, the flat channel configuration is also included for a sapphire substrate. The lower picture shows the spatial electric field distribution.

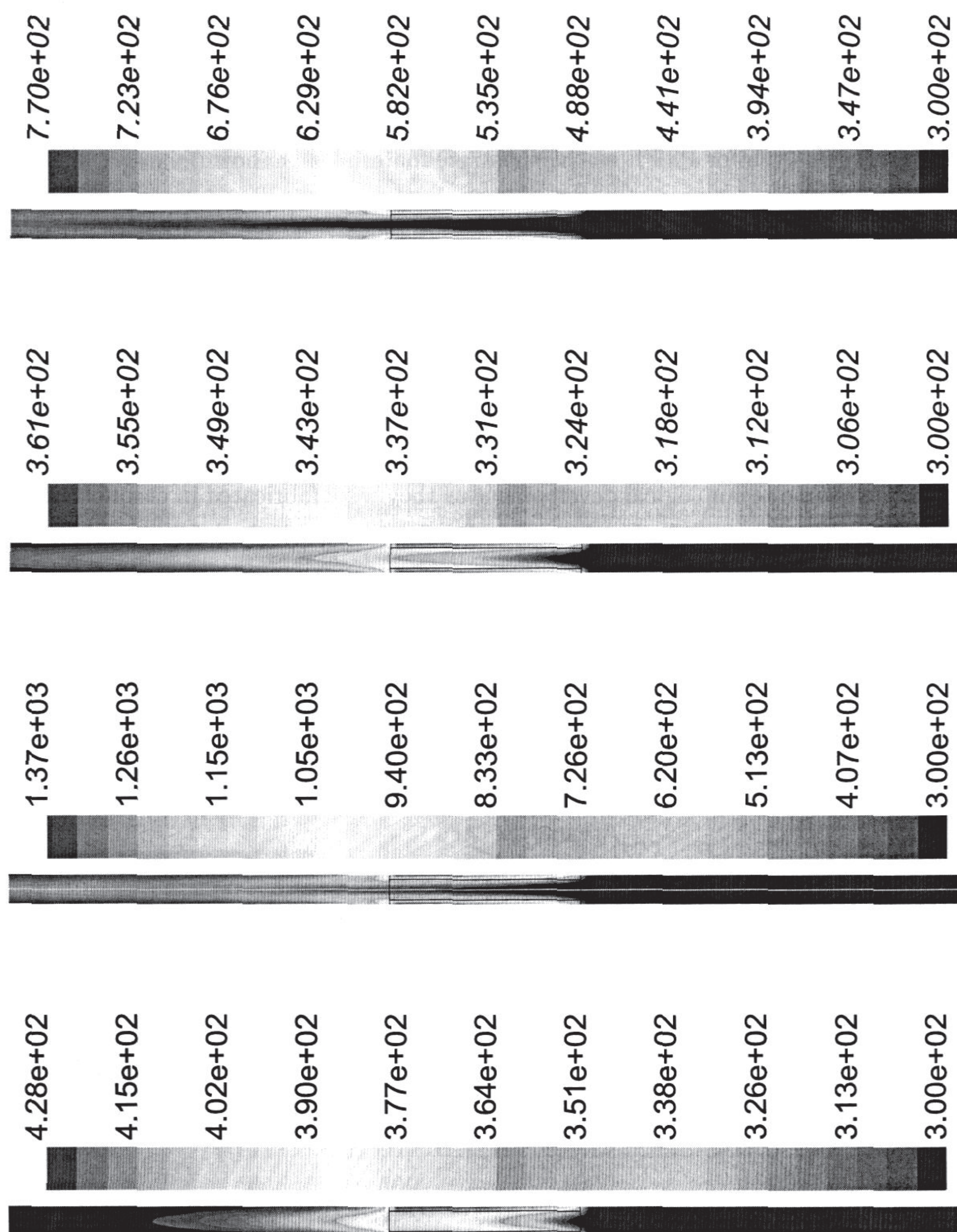

Figure 4.3.: Gas temperature distribution at different operating conditions inside the channel of a sapphire MSP with 0.9 mm *cross section. From top to bottom:* Ar *at* $P = 10$ W , $\dot{V} = 500$ mL min^{-1} *; ditto for* He; Ar *at* $P = 20$ W , $\dot{V} = 200$ mL min^{-1} *; ditto for* He.

5 mm for a gas channel of circular cross section with 0.9 mm in diameter. Figure 4.3 shows the temperature fields for Ar and He at different operating conditions for a sapphire substrate material. The temperature field correspondes well to the visually observable plasma shape. It should be noted that the temperatures for He are rather low even for PTFE as the substrate material (not shown).

4.3. Application specific MSP designs

The MSP design can be optimized according to the specific requirements of a certain application. This can be the possibility to sustain a He discharge at low power or the ability to work in low pressure or simply a smaller size of the wafer. The next three sections present different MSP design according to different applications. These also underwent some technological development as they were fabricated in chronological succession. However, all devices have the above outlined principals in common.

4.3.1. An MSP for the optical emission spectrometric (OES) analysis of mercury

Technology

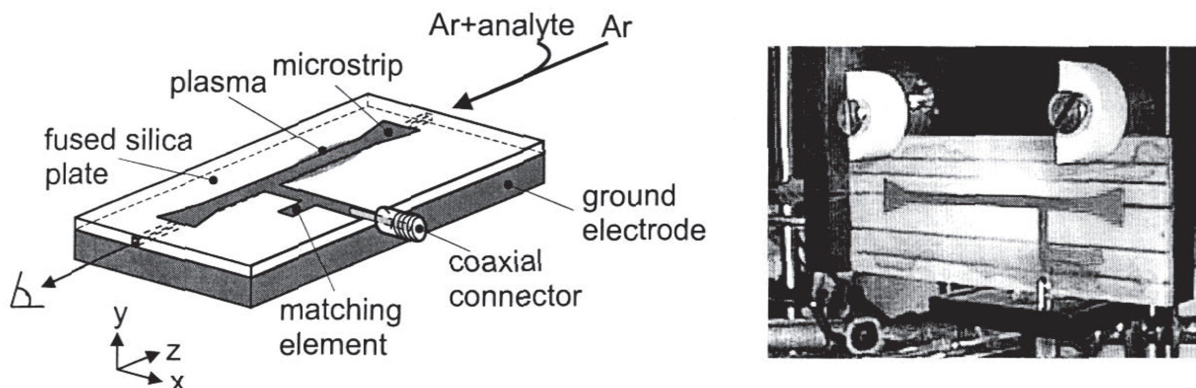

Figure 4.4.: Microstrip Plasma Source I (MSP I). The Plasma is confined in the gas channel under the central transmission line. It is reproducibly ignited there with the aid of a high voltage spark. The tapering of the central transmission line at the two open endings reduces the electrical field strength thus preventing a plasma ignition there.

The Microstrip Plasma Source (MSP I) basically consists of a planar microstrip

line on fused silica SiO_2 as dielectric substrate and a massive copper ground plate which also serves as a heat sink (see figure 4.4). The plasma-gas channel is inside the dielectric substrate below the microstrip line in the dielectric substrate. The plasma is encapsulated within the dielectric not being affected and contaminated by the surrounding atmosphere. Only a high signal from the OH bandhead at 306.4 nm, caused by traces of moisture in the plasma gas, and a small signal of the NH bandhead at 336.0 nm could be detected (figure 4.7). Plasma wall interactions do not seem to play a fundamental role provided the plasma gas flow does not drop below a critical value of some 10 mL min^{-1}. A dicing-saw equipped with diamond coated blades of 1000 μm in diameter was used producing this structure. One also could employ etching techniques for producing structures in fused silica and easily create curved channels and more complex structures.
The microstrip line and the additional open stub matching element were fabricated in three steps. The silica plate was sputtered with copper up to 1 μm to form the basis for a conducting layer. Electro-plating this initial layer up to several μm thickness is necessary since the skin-depth in copper at 2.45 GHz is about 2 μm. For the delineation of the described structures onto the processed silica plate standard photolithographic techniques are used.

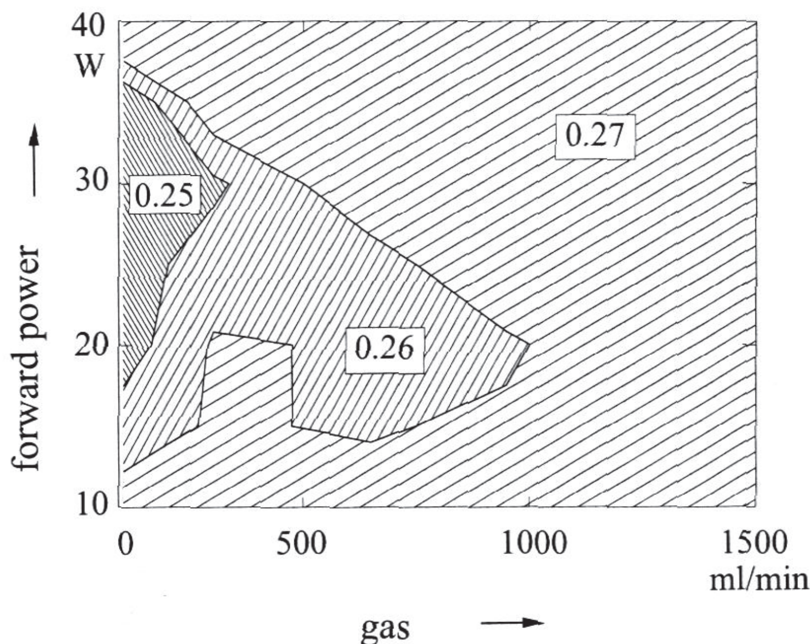

Figure 4.5.: Power and gas-flow range for a stable Ar *plasma and low reflected power. The contour lines indicate areas of constant amplitude reflection coefficient.*

Principles of Operation

The microstrip transmission lines are designed for about 50 Ω wave impedance without the plasma. After ignition of the plasma, the MSP can be considered, in a first view, as a lossy transmission line [72]. Nevertheless, since a plasma is the power absorbing medium, these descriptions have to be taken with care since highly non-linear effects arise when changing the matching conditions or the plasma supporting gas-flow or in-coupled microwave power. For simplicity, we regard the microstrip line with the operating plasma as a transmission line with a complex effective impedance $\underline{Z}_{pl}$. At least one reactive matching element in connection with the reactances of the open ended central transmission line turned out to be necessary for low reflection coefficients. The layout in figure 4.4 has been designed experimentally. A more complex matching network would cover a broader range of plasma-parameter and could equally well be integrated onto the fused silica plate. Nevertheless, we could achieve a stable plasma for a gas-flow range of 50 mL min^{-1} – 1600 mL min^{-1} Ar at a microwave forward power of 10 W – 40 W. The maximum reflected power was 4 W, giving a maximum amplitude reflection factor of 0.3, as depicted in figure 4.5. These relatively low power consumptions allow it to use a semiconductor microwave source. In order to efficiently collect the emitted radiation, a fiber optics coupling to a miniaturized spectrometer provided on a PC card is feasible. In this way a complete multi-element element-specific detection system could be installed on a single computer board as a part of a μTAS. In this section the analytical features of this new plasma source are demonstrated by a determination of traces of Hg in aqueous solutions with the aid of a flow injection cold vapour technique (FI-CV). This application is of high environmental interest, because of the high toxicity of Hg and its compounds [158]. The latter are released in the environment through the use of batteries or in industrial processes like the chlorine-alcaline electrolysis, which is still the largest anthropogenic emission source of Hg.

Experimental

In a SpectroMerc (Spectro Analytical Instruments, Kleve, Germany) flow-injection cold vapour atomic absorption (FI-CV-AAS) spectrometer, the atomic absorption detection is replaced by the MSP I. The radiation of the MSP is imaged onto the entrance slit of a 0.5 m Czerny-Turner monochromator with the aid of a quartz lens. The widths of the entrance and the exit slit of the monochromator are 40 and 70 μm, respectively. The intensities of the Hg *I* 253.7 nm line are measured with a photomultiplier, which is read out by a current to voltage converter and a personal computer

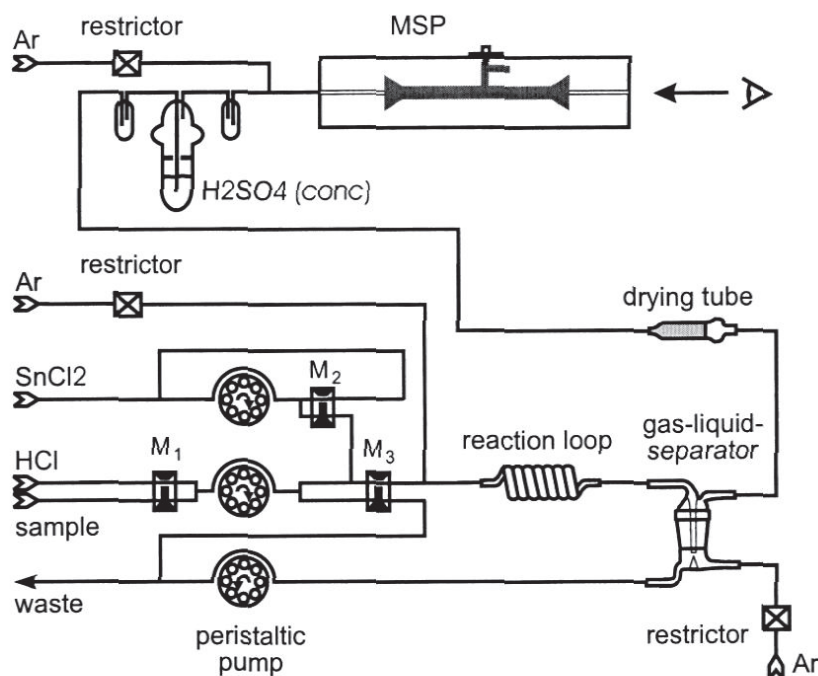

Figure 4.6.: CV-FI-MSP-OES set-up used.

equipped with a data acquisition card. In figure 4.6 the flow injection system used for the FI-CV-MSP-OES system is given. The exit of the gas/liquid separator is connected to the MSP via the drying tube containing $Mg(ClO_4)\,2 \cdot x\,H_2O$, provided in the FI-CV-AAS system. Additionally, the gas flow is bubbled through a vessel containing H_2SO_4 to remove any traces of moisture from the gas flow leaving the FI-CV system. Afterwards, this dried gas is mixed in a T-connector with the plasma gas flow before entering the MSP I. The FI-CV system is operated in a segmented-flow mode, and the sample, acid and $SnCl_2$ solution flows are injected separately through tubings with the aid of a peristaltic pump. All flows are regulated by magnetic valves, which are switched under computer control. The optimized parameters of the Hg vapour generator and more details about the system used are given by Haase et al. [159]. When the AAS cell in FI-CV system is replaced by the MSP I the delay time between each measuring circle must be increased and Ar must be used instead of N_2. Also both gas restrictors are to be kept in the position "open" during the whole measurement cycle.

Results

According to the visually observed plasma form it can be recognized that in the centre of the gas channel the intensities of the Hg I 253.7 nm obtained are somewhat

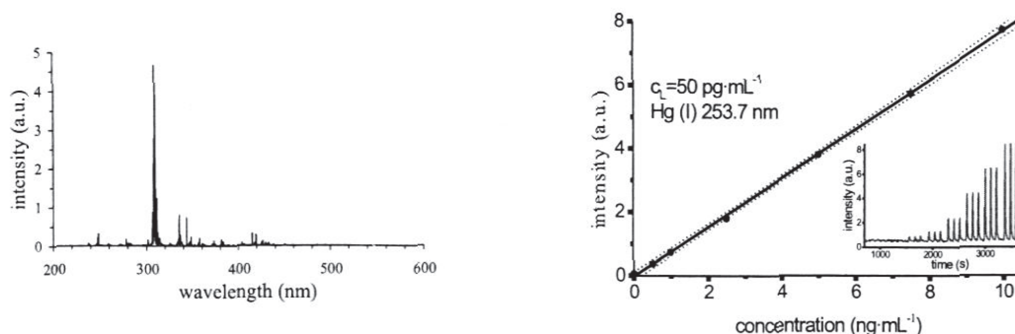

Figure 4.7.: Emission spectrum of a 15 W Ar *MIP in the MSP (left) and calibration curve for* Hg. *This is obtained with standard solutions containing* Hg *between* 0.5 *and* $10\,\mathrm{ng\,mL^{-1}}$ *(Plasma conditions are* 30 W *forward power and an* Ar *gas flow of* $300\ \mathrm{mL\,min^{-1}}$ *plasma gas plus* $400\ \mathrm{mL\,min^{-1}}$ *carrier gas flow).*

lower. The plasma thus fills out the gas channel almost homogeneously. The rotational and excitation temperatures measured were 650 ± 30 K and 8000 ± 1600 K, respectively. The errors in the determination of the temperatures were determined by the errors in the slope of the Boltzmann plots. As expected the plasma is far away from local thermal equilibrium (LTE), as it is the case in many other microwave induced plasmas. The relatively low rotational temperatures explain, why the plasma has a low tolerance against traces of water e.g. in the Hg vapour containing gas flows. Therefore, it was required to dry the analyte containing gas flow additionally by leading it through a sulfuric acid containing vessel. The high excitation temperature and the high analyte number densities in the MSP device explain the good excitation capacity of the MSP. The long term stability and the precision achievable over a time period of about 80 min were tested by performing 45 replicate measurements with solutions of $10\ \mathrm{ng\,mL^{-1}}$ Hg. The relative standard deviation for the heights of the transient emission signals obtained was only 1.4 %. In figure 4.7 a calibration curve obtained with standard solutions having concentrations of Hg between $0.5\,\mathrm{ng\,mL^{-1}}$ and $10\,\mathrm{ng\,mL^{-1}}$ is given. The relative standard deviations for the replicate measurements were between 0.5 % and 0.5 % in the case of peak height measurements, the correlation coefficient was 0.9998 and the limit of detection calculated according to [160] was $50\,\mathrm{pg\,mL^{-1}}$.

The MSP II design and first developments for aerosol introduction

The introduction of aerosols is a long and well known problem in MIPs. Devices with a relatively high tolerance against aerosol introduction are the MPT as discussed

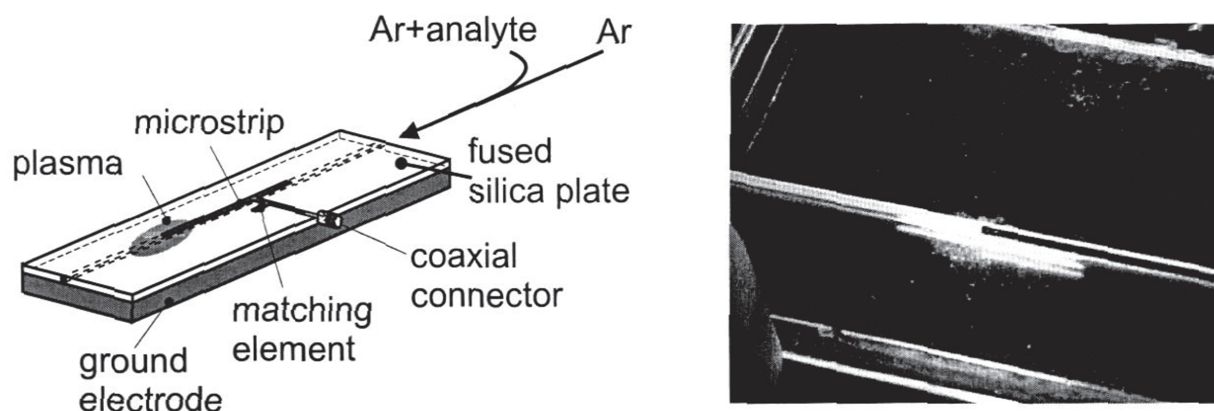

Figure 4.8.: MSP II design and photograph with operating Ar *plasma.*

in chapter 3 or comparable set-ups. The MSP I is unfortunately very sensitive for aerosol contaminations in the plasma gas stream. Guided by the insights gained with the MPT an experimental MSP set-up is constructed, rather similar to the MSP I design but omitting the necessity for a 50 Ω wave impedance of the strip line and moving the plasma operation from the centre of the central strip line to its end (see figure 4.8). In this way the electric field strengths are increased due to the higher wave impedance of a smaller strip line. In addition a set of transverse channels is created for a separate aerosol introduction, see figure 4.9. Experiments show that a stable plasma can be sustained at a gas flow of 500 mL min^{-1} and 15 W forward power even if a 200 mL min^{-1} water saturated Ar gas stream introduced through the transverse channels. By this it is shown that principally an MSP could be constructed for the analysis of aerosols. Further developments have to show how to proceed in this direction.

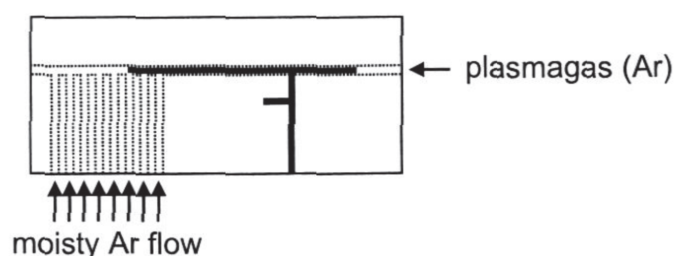

Figure 4.9.: MSP II with separated aerosol introduction channels.

4.3.2. An MSP for the optical emission spectrometric (OES) non-metal detection

Introduction

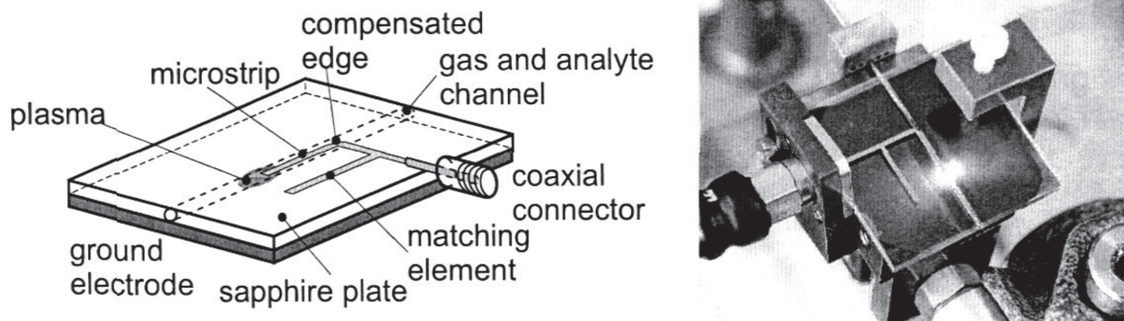

Figure 4.10.: Microstrip plasma source for He *(MSP III). The quadratic sapphire wafer is* 30 mm *long and* 1.5 mm *thick. It has a grown-in channel of* 0.9 mm *in diameter. The microstrip line has a width of* 0.8 mm*. Photograph of the MSP IV. The plasma can easily be recognised as the bright spot below the end of the microstrip.*

With the above presented set-up it is not possible to sustain a He plasma at power levels below 40 W, which in turn could be very useful for the detection of non-metals, e.g. as required by element-specific detection in gas chromatography (GC). For low-power He plasmas and for a further miniaturization of the set-up the microstrip approach is optimized with the aid of numerical simulations and improved layout rules [72] of the microstrip configuration. A reduction of the average forward power to approximately 2 W would allow for the use of very small and low cost integrated microwave power supplies with sizes in the sub cm^{-3} range as they are used in mobile communication devices. This allows for very compact plasma sources already including the microwave generator. Driven by these aims we developed an MSP on the basis of a sapphire wafer as described below.

Technology and Design

The He Microstrip Plasma source (MSP III) consists of a single 1.5 mm sapphire wafer with a straight grown-in gas channel of 0.9 mm diameter and 30 mm length. Both sides of the wafer are covered by a 100 nm titanium adhesion layer and a 2 μm copper layer produced by sputtering. The microstrips are delineated by standard

photolithographic processes used for integrated microwave circuits. A shielding of the structured microstrip with an electroplated Au layer of several mm thickness enhances the long term stability. The ground electrode is connected to a copper socket with an active air cooler of 25 × 25 mm size. Figure 4.10 shows the MSP III geometry with the microstrip configuration and the integrated plasma gas channel together with a photograph. The He-plasma is excited near the end of the microstrip line. It has a length of typically several mm. The microstrip geometry is optimized to use only a small amount of wafer area. This is done by introducing a compensated edge to bend the electrode by 90 degrees. The exact design of this edge is very important for an effective and reflectionless propagation of the microwave field along the electrode and must follow well-know rules [72]. The ratio of electrode width to electrode separation determines the electric field strength between them. In general, smaller electrodes increase the characteristic wave impedance thus resulting in higher voltages. The electrodes are chosen to achieve high electric fields in the plasma channel while retaining a good matching to the 50 Ω power line. Sapphire substrates are chosen because of their relative high anisotropic dielectric constants of $\varepsilon_x = \varepsilon_z = 9.4$ and $\varepsilon_y = 11.6$ along the respective axes (see figure 4.10 for axis orientation) which considerably enhances the electric field strength in the gas channel. This is indicated by simple Finite Difference calculations. In addition, its mechanical and thermal stability is much better compared to fused silica and it is also chemically inert.

Results

Following these concepts, we were able to fabricate an MSP, which generates a He or Ar plasma inside the gas channel at atmospheric pressure with forward power of 5 – 30 W (1 – 10 W in Ar) and gas flows of 50 – 1000 mL min^{-1}. Moreover, the He plasma is self-igniting when exceeding a certain threshold of forward power, which depends on the gas flow. For a gas flow of 100 mL min^{-1} this is just below 10 W forward power. First experiments show the ability to excite Cl with this He plasma thus enabling its usage as an element specific emission detector for e.g. in gas chromatography (GC). This was shown by introducing small amounts of saturated $HCCl_3$-vapour with the aid of a microlitre syringe via a septum in the He gas flow. In figure 4.11 the obtained emission signals for the Cl (I) 912.11 nm line for a 20 and 50 ml injection are shown. These were obtained by a 0.5 m Czerny-Turner monochromator with a CCD camera in the focal plane [140]. This experiment was taken at 15 W forward power and a He gas flow of 700 mL min^{-1}. Obviously, the plasma is able to atomise the organic molecules and to excite in an appropriate

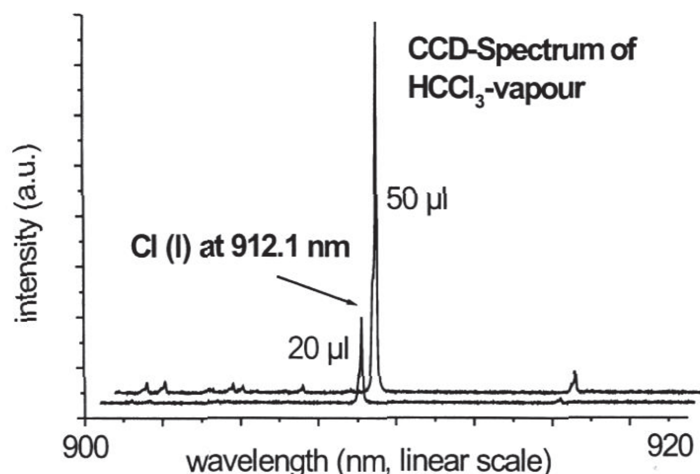

Figure 4.11.: CCD spectrum of $HCCl_3$ *vapour volumes (absolute amount of* 4 µg *(*20 µl *) and* 4 µg *(*50 µl *), respectively) introduced into the plasma gas flow. The lines are shifted for a better graphical representation but belong both to the* Cl (*I*) *line at* 912.1 nm *.*

way, so that quantitative Cl detection should be possible. Despite the fact that we deal with a low-power small-scale plasma one has to keep in mind that the power density is still comparable to other more common microwave induced plasma as e.g. the MPT [64]. Here, the ability to excite Cl with a He plasma is well known [27]. Besides the power density, the electric field strength is a fundamental parameter for sustaining a plasma. The MSP III achieves high electric field strengths due to the compact geometry and the high permittivity of the substrate. In common MIPs the electric field is increased by enhanced power levels. This is a fairly inefficient way to proceed as the electric field increases with the square root of the forward power, only.

4.3.3. An MSP for the atomic absorption spectrometric (AAS) chlorine analysis

Atomic absorption spectrometry (AAS) is besides OES the complementary method atomic spectrometry bases on. It uses the characteristic resonance absorption of radiation for the element specific detection. This method found broad acceptance since the introduction of laser diodes. The analytical performance of laser diode AAS (LD-AAS) is by far superior as compared to conventional AAS and ideally

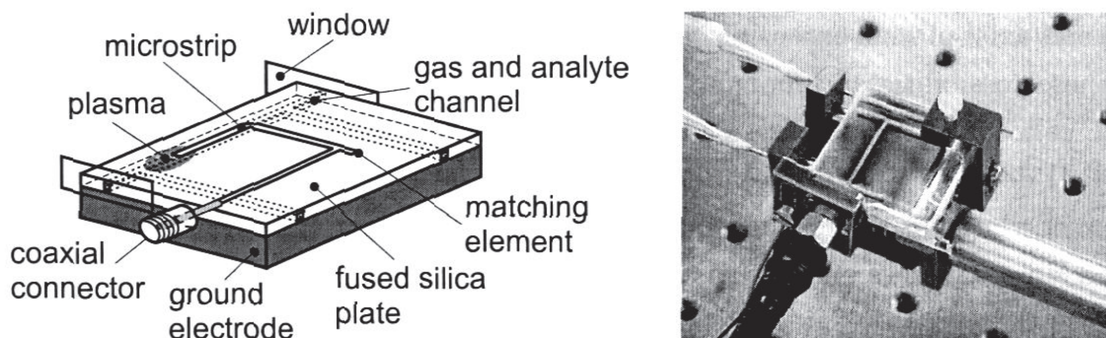

Figure 4.12.: Schematic drawing (left) and photo (right) of an MSP IV device for LD-AAS operated at a modulated power of 13.5 W .

suits the needs of the semiconductor industry where contaminations of chemicals must not exceed a value of 0.1 ng mL^{-1} . These extremely low detection limits can be ascribed to wavelength modulation techniques [161, 162] and the low random noise of the laser diodes. Many elements can already be detected by LD-AAS but the non-metals. Their resonance lines lie within the vacuum UV region still not covered by laser diodes. Another approach is to employ meta stable states which can only be produced in sufficient quantity at low pressure [163, 164].

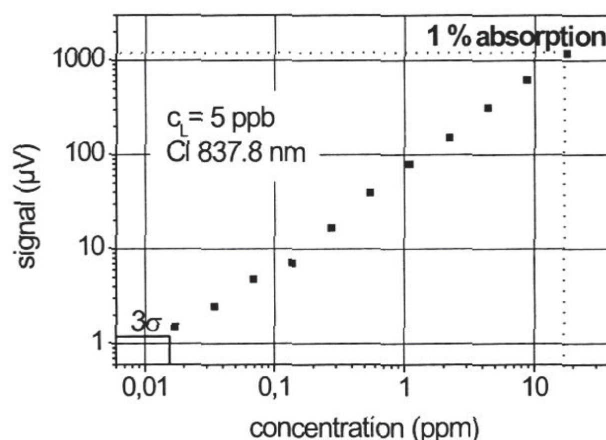

Figure 4.13.: Calibration for Cl in a He *plasma of an MSP IV with LD-AAS.*

An MSP could be an ideal plasma source for such applications because of its small

size and axial plasma extension which allows for a good absorption rate. Motivated by these possibilities a completely new MSP design is carried out, as shown in figure 4.12, called MSP IV. It bases on the same fabrication techniques as the MSP I and MSP II devices. But due to its usage for AAS the laser beam has to pass the gas channel which for this purpose has a *Pi* shape. The open ends are sealed up with fused silica windows and the gas in- and outlet are realised by the two arms of the Π form channel.
First experiments demonstrated the principal ability to detect chlorine via LD-AAS. Since the Ar plasma suffers from some disturbances by the introduction of the analyte a He plasma is chosen for the calibration as shown in figure 4.13. It is obtained by introducing diluted CCl_2F_2 with the plasma gas leading to a calibration between 0.03 ppm and 17.5 ppm. The transition $4s\,^4P_{5/2} \longrightarrow 4p\,^4D^0_{7/2}$ for Cl is observed at 837.824 nm. The plasma modulation frequency is 12.5 kHz at an average forward power of 13.5 W. The detection limit under these conditions for Cl is $c_L = 5$ ppb at a linear range of at least three decades.

5. Conclusion and final remarks

The modified MPT presented here as well as in its original form presented by Jin et al. in [6] found manifold applications predominantly in the field of analytical chemistry. An excellent review on most of the MPT related research of the last years from the viewpoint of a chemist can be found in [42].
The MPT is improved in terms of stability and construction simplicity as outlined in [32]. An electric equivalent circuit helps to analyse and understand its operational principles which can be best described as an impedance matching network just with a dynamic complex load (plasma). Electromagnetic and fluid dynamic modelling give further inside into processes like power dissipation and gas flow which would be very difficult to measure. In combination with sophisticated plasma diagnostic measurements like Thomson scattering of the electron density finite difference calculations can consistently predict the spatial distribution of electromagnetic fields and power in-coupling into the plasma. This is the primary interface for fluid dynamic calculations of the gas and heat flows as these are highly sensitive to this additional energy term. These simulations also lead to a lumped element model of the plasma as a complex load impedance which can be used in turn to further optimise MPT design within a certain range of macroscopic parameters like power and gas flow.
This modified MPT is used in combination with spark ablation (SA) for the analysis of metals (MPT-OES) [71] and for the element specific detection in combination with high performance liquid chromatography (HPLC) for the speciation of Cr(III) and Cr(IV) in soils [57]. In addition, some research in industrial applications is upcoming in the last years with MPT-like constructions for combustion or surface treatment in a variety of different working environments. Here, the MPT owns a high potential since it is still all but simple to generate microwave induced plasmas at atmospheric pressure with comparable stability and compactness as the MPT without loosing its simplicity in construction.
The analytical features of the new miniaturised microwave plasma source MSP I based on microstrip technology for OES showed that it has great potential for use in μTAS. The rotational and excitation temperatures of 650 K and 8000 K, re-

spectively, explain both its low tolerance for water loaded aerosols and its good excitation capacity. The spatial intensity distribution for the Hg I 253.7 nm line showed that the MSP device is able to excite the analyte in a suitable way and that the plasma channel in the MSP device is almost completely filled by the plasma. With the experimental set-up for the determination of Hg in aqueous solutions by FI-CV-MSP-OES a limit of detection, which is only slightly higher than in FI-CV-AAS could be obtained. Therefore, the use of the MSP device instead of the AAS detection offers the possibility of multielement determinations. The latter in principle showed be easily possible with all types of vapour generation volatile compound formation by chemical methods (e.g. Ni as $Ni(CO)_4$, I, S, ...), electrothermal vaporisation of dry solution residues, laser and spark ablation for direct solids sampling a.s.o.. However, in every particular case the limiting factors such as the accompanying gases formed, eventual gas pressure jumps or influences of the sample vapour clouds on the plasma still have to be investigated in detail for the types of samples to be analysed.

The MSP II set-up shows to be a promising candidate for an aerosol tolerant MIP. Here again the principle of separate channels for the plasma gas and the aerosol introduction proved to be successful. However, these positive first experiments have to be completed by a systematic approach to optimize the MSP for such applications. Here, one could also think about surface treatment applications of any kind.

The MSP III meets the requirements for a low-power He plasma at atmospheric pressure and could be very useful for the emission detection of non-metals like halogens and chalcogens. It can also be operated with argon at power levels above 1 W . As this set-up shows the potential for further down-scaling of the wafer height and increasing the characteristic wave impedance of the microstrip e.g. by reducing the strip width w, it would also allow for still lower operation power thus enabling the use of very small and cost efficient integrated microwave transmitters as used in mobile communications. This however, requires a shift of the operation frequency to e.g. the 1800 MHz GSM band. From a technical point of view no serious difficulties should be expected but international restrictions on freely usable ISM bands may cause some problems. The self ignition of a He discharge is of great practical interest since it overcomes the otherwise necessary external ignition by a high voltage spark, which in turn would require special protection to prevent semiconductor microwave sources from damage.

And finally also the forth device, the MSP IV, demonstrated its principal ability to serve as a plasma source for LD-AAS. Despite manifold problems preliminary set-ups encountered with the low pressure facilities, one could readily think of a similar

set-up as the MSP III but with an Π shaped channel. This would allow for very simple set-ups for AAS. One may conclude that there are still lots of different areas where the basic technology of the MSP devices can lead to prosperity.

Summary

Subject of this thesis are microwave induced plasma sources (MIP) operated at atmospheric pressure in noble such like helium or argon. The main field of their application is the atomic spectrometric chemical analysis where plasma sources in general and especially MIPs look upon a long tradition. The focus is less on the generated plasma itself but on the design and simulation of the plasma sources. Two basically distinct approaches are chosen to meet the analytical requirements.

First, coaxial plasma sources are discussed, exemplified at the "Microwave Plasma Torch" (MPT) design. These produce a toroidal flame like plasma on top of the gas feeding structures without plasma-material interactions thus preventing spectral disturbances. It is shown that these plasma sources are operated basically non-resonant and as a consequence suffer much less from matching problems due to plasma perturbations by analyte introduction. This stability against wet aerosol is also supported by the specific hollow structure of the plasma, i.e. the plasma density has a minimum in the centre of the toroidal flame by which an analyte introduced along this channel causes only little perturbation. An electric equivalent circuit model is employed to describe the impedance transformation characteristics and to calculate optimal matching conditions. The major parameter there is the unknown effective plasma impedance. This is extracted from in an experimental way from reflection factor measurements.

The electron density and the electron temperature for an MPT plasma are determined by Thomson scattering measurements under different operating condition in order to study the influence of several macroscopic parameter. It is shown that the hollow structure can also be found in the electron density distribution. The electron density leads within the framework of the dielectric plasma model and numerical field calculations to an effective plasma impedance whose magnitude is comparable to the experimental value.

A generalised finite difference approach on mapped grids is developed for the numerical calculation of the electromagnetic field of the MPT and the derived quantities as power flow and dissipated power density. It allows for a simple central difference formulation of the differential operators in second order through a covariant formulation of the governing field equations. It should be noted that this is the only way to maintain second order accuracy on non-equidistant grids while keeping the discretisation as simple as on equidistant grids.

The second solution presented to construct a low power MIP is through the usage of microstrip technology. This new invention allows for very compact and power saving devices ideally suited for micro total analysis systems (μTAS) or mobile applications. The microstrip plasma sources (MSPs) are fabricated on a ceramic substrate such as fused silica or sapphire with gas flow structures inside and a printed circuit on top following well known techniques of integrated microwave circuit design. With these devices, power levels as low as several Watt and gas flows of some 10 $\mathrm{mL\,min^{-1}}$ can be achieved. The low power requirements allow for the employment of standard semiconductor transmitters such as used in mobile communications as a high frequency source.

Some optimised designs for applications in optical emission spectrometry (OES) and atomic absorption spectrometry (AAS) are presented together with first results of their analytical performances. Preliminary numerical modelling is carried out to investigate the mass transport and electromagnetic characteristics of the MSP.

A. Layouts of microstrip plasma sources

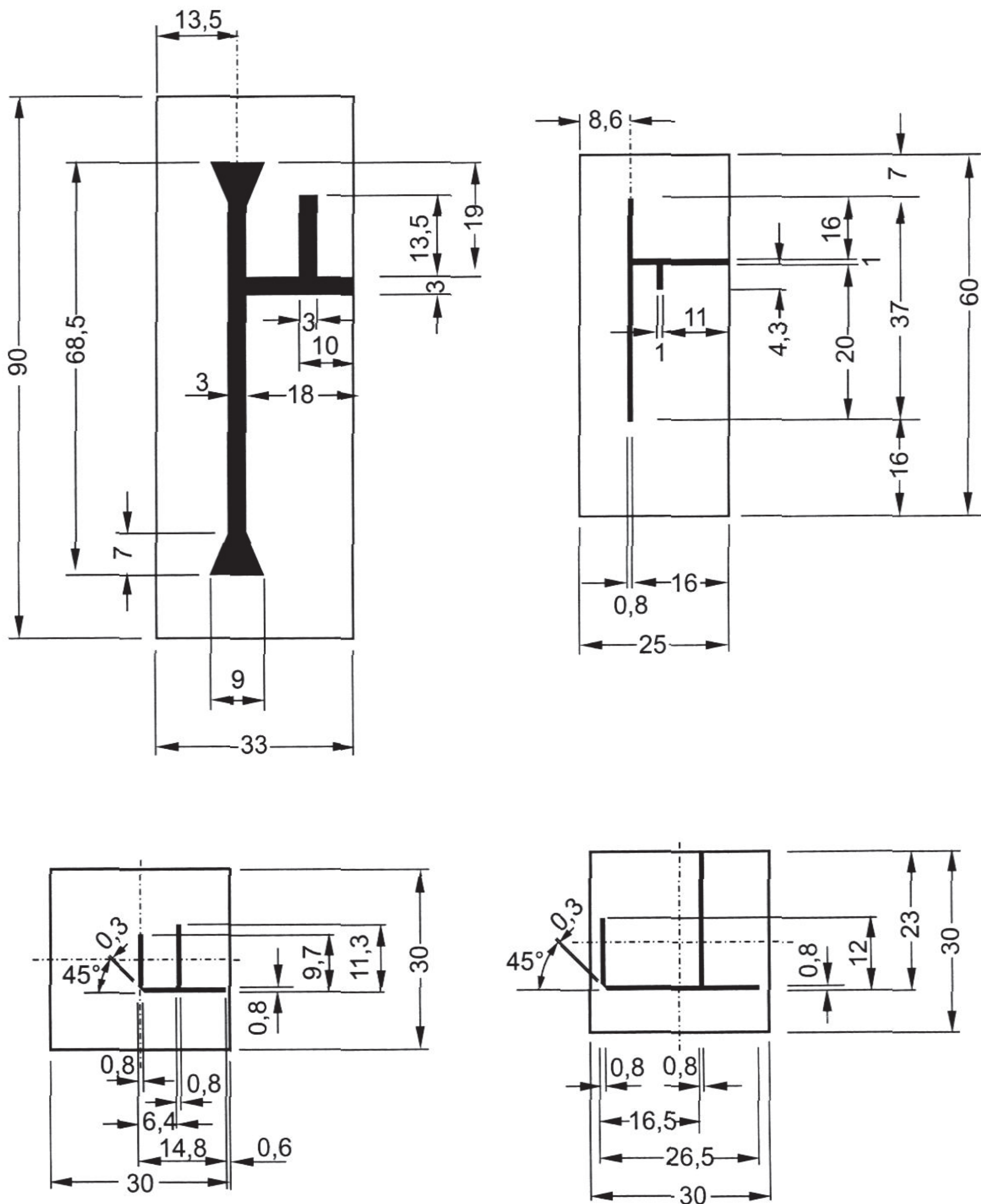

B. Finite Differences on mapped grids

B.1. Transformation coefficients, metric tensor and Christoffel symbols

For a description of the physical objects considered here (plasma and plasma source), we like to choose grid lines which conform to the object boundaries as well as possible. These grid lines should also be non-equidistantly spread over the computation domain to account for the possible inhomogeneity of fields to be calculated, becoming dense in regions of high field gradients and sparse elsewhere. The (Cartesian) coordinates of the points of intersecting grid-lines are denoted with x^i. By construction it is possible to map these x^i onto an equidistant and rectangular grid made up of the values of the curvilinear coordinates x^μ at these points:

$$x^\mu \mapsto x^i = x^i(x^\mu) \quad . \tag{B.1}$$

In fact choosing the curved grid-lines as coordinate lines of a new coordinate system assures this feature [121]. For simplicity we always confine the x^μ to the interval $[0,1]$ with a spacing $\Delta x^\mu = \frac{1}{N_\mu - 1}$ if N_μ is the number of grid-lines of the respective coordinate. It should be mentioned that there is no need for an analytical expression for this mapping as all the necessary quantities are derived from the x^i through numerical evaluation. Thus a numerical data-set of "hand-made" grid-lines would also be sufficient.

In curvilinear and non-orthogonal coordinates one has to distinguish between covariant and contravariant base vectors (see figure B.2) and the respective components of vectors expressed with reference to these bases. Covariant base vectors are tangential to coordinate lines while contravariant base vectors are perpendicular to these. In general a contravariant vector $\mathbf{V}^\mu$ is defined by the fact, that its components are transformed according to the coordinate differentials

$$\mathrm{d}x^i = \frac{\partial x^i}{\partial x^\mu}\,\mathrm{d}x^\mu =: \partial_{x^\mu} x^i\,\mathrm{d}x^\mu =: p_\mu{}^i\,\mathrm{d}x^\mu \quad , \tag{B.2}$$

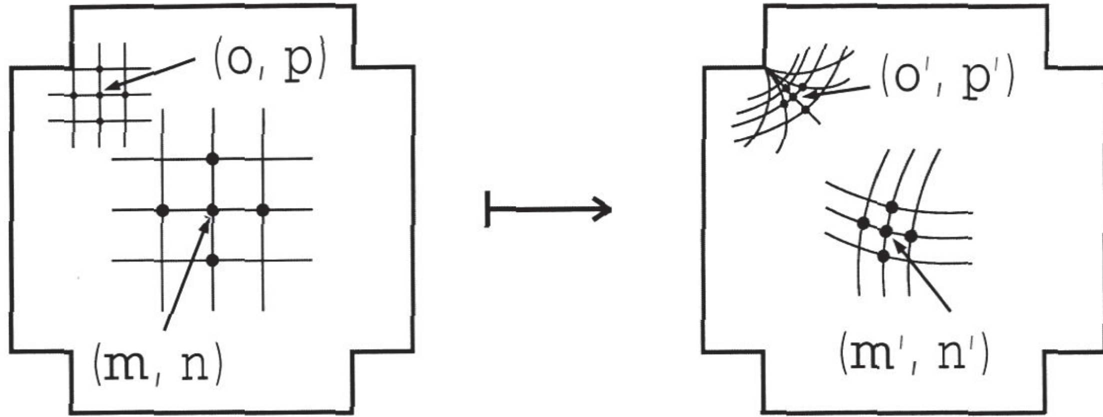

Figure B.1.: Grid transformation example.

where ${p_\mu}^i$ is the Jacobian Matrix of the transformation. This matrix will be evaluated numerically [123] through finite difference expressions of the form

$$\frac{\partial x^i}{\partial x^\mu} = \frac{1}{2\Delta x^\mu}(x^i(x^\mu + \Delta x^\mu) - x^i(x^\mu - \Delta x^\mu)) \quad , \tag{B.3}$$

which gives a second order truncation error since the x^μ form a simple, rectangular and equidistant grid by construction. Even if the analytical mapping is given, the numerical evaluation should be preferred due to its minor overall errors as pointed out in [121]. A covariant vector $\mathbf{V}_\mu$ is defined by the inverse transformation. They are connected through

$$\mathbf{V}_\mu = \sum_\nu g_{\mu\nu} \mathbf{V}^\nu \quad , \tag{B.4}$$

where the metric tensor is defined as

$$g_{\mu\nu} = \sum_i {p_\mu}^i {p_\nu}^i \quad . \tag{B.5}$$

The contravariant metric must be calculated from

$$\sum_\nu g_{\mu\nu} g^{\nu\rho} = \delta_\mu^\rho \quad , \tag{B.6}$$

i.e. a matrix inversion has to be carried out, since the back transformation is in general not known except for the cases where the transformation is given by an analytical expression and invertible. Further-on, we introduce the physical components of covariant and contravariant vectors

$$\mathbf{V}_{(\mu)} = \sqrt{g^{\mu\mu}} \mathbf{V}_\mu \tag{B.7}$$

$$\mathbf{V}^{(\mu)} = \sqrt{g_{\mu\mu}} \mathbf{V}^\mu \tag{B.8}$$

and put them into parentheses. Their definition is necessary when referring to physical quantities since the curvilinear base vectors are not normalised in general and would lead to strange units otherwise. In curvilinear coordinates the usual partial derivative has to be replaced by a covariant derivative defined as

$$\mathrm{D}_\mu \mathbf{V}_\nu := \partial_{x^\mu} \mathbf{V}_\nu - \sum_\rho \Gamma^\rho{}_{\mu\nu} V_\rho \qquad \mathrm{D}^\mu \mathbf{V}_\nu := \sum_\rho g^{\mu\rho}\, \mathrm{D}_\rho \mathbf{V}_\nu \quad . \tag{B.9}$$

acting on a covariant vector $\mathbf{V}_\mu$. Here we require the calculation of the Christoffel-symbols (of the second kind)

$$\Gamma_{\rho\mu\nu} = \sum_i p_\rho{}^i p_{\mu\nu}{}^i \quad . \tag{B.10}$$

This formulation of calculating the $\Gamma_{\rho\mu\nu}$ is advantageous for a direct numerical finite difference evaluation. The Christoffel-symbols of the first kind are then obtained from

$$\Gamma^\rho{}_{\mu\nu} = \sum_\tau g^{\rho\tau} \Gamma_{\tau\mu\nu} \quad . \tag{B.11}$$

The second order transformation coefficients appearing in this definition are

$$p_{\mu\nu}{}^i := \frac{\partial^2 x^i}{\partial x^\mu \partial x^\nu} \quad . \tag{B.12}$$

The differential operators occurring in all equations are replaced by finite difference approximations:

$$\partial_{x^i} \psi \longmapsto \Sigma_j c_j \psi(x^i|_j) \quad . \tag{B.13}$$

where the coefficients c_j are determined by a series expansion around the central point. A simple example for these mappings and the evaluation of the metric quantities is given in section B.3.

B.2. Covariant formulation of Maxwell's equations and the vector wave equation

The above equations define all the metric quantities required to formulate 3.30 in a covariant, i.e. coordinate system independent way:

$$\begin{aligned}[\nabla \times \frac{1}{\varepsilon_{pl}} \nabla \times \underline{\mathbf{H}}]_\mu &= \sum_{\nu,\rho,\sigma,\tau} \epsilon_{\mu\nu\rho} \epsilon^{\rho\sigma\tau}\, \mathrm{D}^\nu \frac{1}{\varepsilon_{pl}} \mathrm{D}_\sigma \underline{\mathbf{H}}_\tau \\ &= \sum_\nu \mathrm{D}^\nu \frac{1}{\varepsilon_{pl}} \mathrm{D}_\mu \underline{\mathbf{H}}_\nu - \mathrm{D}^\nu \frac{1}{\varepsilon_{pl}} \mathrm{D}_\nu \underline{\mathbf{H}}_\mu = \varepsilon_0 \mu_0 \omega^2 \underline{\mathbf{H}}_\mu \end{aligned} \tag{B.14}$$

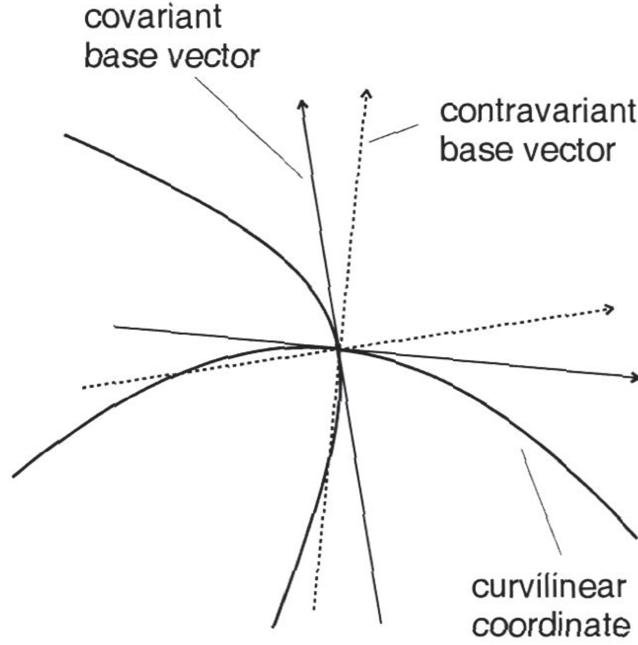

Figure B.2.: Covariant and contravariant base vectors of a curvilinear coordinate system.

The co- and contravariant ϵ-(pseudo)tensors are defined as

$$\epsilon_{\mu\nu\rho} = \sqrt{g}\;\epsilon_{(\mu\nu\rho)} \tag{B.15}$$

$$\epsilon^{\mu\nu\rho} = \frac{\epsilon^{(\mu\nu\rho)}}{\sqrt{g}} \tag{B.16}$$

where $g = \det[g_{\mu\nu}]$ is the determinant of the covariant metric tensor and $\epsilon_{(\mu\nu\rho)}$ is the known total antisymmetric unit (pseudo)tensor. We introduce the covariant $x_\mu \in \{x_0, x_1, x_\varphi\}$ and contravariant coordinates $x^\mu \in \{x^0, x^1, x^\varphi\}$ but restrict ourselves to rotational symmetry with the azimuthal components x_φ and x^φ respectively. This reduces the above double curl equation to the vector Laplace equation

$$\sum_\mu \mathrm{D}^\mu \frac{1}{\underline{\varepsilon}_{pl}} \mathrm{D}_\mu \underline{\mathbf{H}}_\varphi + \underline{\varepsilon}_0 \mu_0 \omega^2 \underline{\mathbf{H}}_\varphi = 0 \quad , \tag{B.17}$$

since $\mathrm{D}^\varphi(\underline{\varepsilon}_{pl})^{-1}\mathrm{D}_\mu \underline{\mathbf{H}}_\varphi = 0$. This is also valid without rotational symmetry since in curvilinear but non-Riemannian (flat) spaces the commutator of the covariant derivative vanishes and $(\nabla \cdot \underline{\mathbf{H}}) = 0$ applies.

Expanding the covariant differentiation leads to the expression

$$\sum_\mu \mathrm{D}^\mu \frac{1}{\underline{\varepsilon}_{pl}} \mathrm{D}_\mu \underline{\mathbf{H}}_\varphi = \sum_{\mu\nu} g^{\mu\nu} \mathrm{D}_\mu \frac{1}{\underline{\varepsilon}_{pl}} \mathrm{D}_\nu \underline{\mathbf{H}}_\varphi$$

$$= \sum_{\mu\nu} g^{\mu\nu} \left(\partial_{x^\mu} \frac{1}{\underline{\varepsilon}_{pl}} \partial_{x^\nu} \underline{\mathbf{H}}_\varphi - \partial_{x^\mu} (\frac{1}{\underline{\varepsilon}_{pl}} \Gamma^{\varphi}_{\ \varphi\nu} \underline{\mathbf{H}}_\varphi) - \frac{1}{\underline{\varepsilon}_{pl}} \Gamma^{\varphi}_{\ \varphi\mu} \partial_{x^\nu} \underline{\mathbf{H}}_\varphi \right)$$
$$+ \sum_{\mu\nu\rho} g^{\mu\nu} \frac{1}{\underline{\varepsilon}_{pl}} \left(\Gamma^{\rho}_{\ \varphi\mu} \Gamma^{\varphi}_{\ \rho\nu} \underline{\mathbf{H}}_\varphi - \Gamma^{\rho}_{\ \mu\nu} \partial_{x^\rho} \underline{\mathbf{H}}_\varphi + \Gamma^{\rho}_{\ \mu\nu} \Gamma^{\varphi}_{\ \varphi\rho} \underline{\mathbf{H}}_\varphi \right) \quad . \tag{B.18}$$

for the vector Laplace operator. This expression considerably simplifies for rotational symmetry leading to the wave equation in its final form used for the numerical calculations

$$\sum_{\mu\nu} g^{\mu\nu} \left(\partial_{x^\mu} (\frac{1}{\underline{\varepsilon}_{pl}} \partial_{x^\nu} (\sqrt{g_{\varphi\varphi}} \underline{\mathbf{H}}_{(\varphi)})) - \Gamma^{\varphi}_{\ \varphi\nu} \partial_{x^\mu} (\frac{1}{\underline{\varepsilon}_{pl}} \sqrt{g_{\varphi\varphi}} \underline{\mathbf{H}}_{(\varphi)}) - \frac{1}{\underline{\varepsilon}_{pl}} \Gamma^{\varphi}_{\ \varphi\nu} \partial_{x^\mu} (\sqrt{g_{\varphi\varphi}} \underline{\mathbf{H}}_{(\varphi)}) \right)$$
$$- \sum_{\mu\nu\rho} \frac{1}{\underline{\varepsilon}_{pl}} g^{\mu\nu} \Gamma^{\rho}_{\ \mu\nu} \partial_{x^\rho} (\sqrt{g_{\varphi\varphi}} \underline{\mathbf{H}}_{(\varphi)}) + \varepsilon_0 \mu_0 \omega^2 \sqrt{g_{\varphi\varphi}} \underline{\mathbf{H}}_{(\varphi)} = 0 \quad , \tag{B.19}$$

where we already expressed $\underline{\mathbf{H}}_{(\varphi)}$ in terms of physical components. Starting with the covariant form of the Maxwell equations which is relatively simple due to the fact that

$$\sum_{\mu\nu\rho} g_{\eta\mu} \epsilon^{\mu\nu\rho} (\partial_{x^\nu} \underline{\mathbf{H}}_\rho - \Gamma^{\tau}_{\ \nu\rho} \underline{\mathbf{H}}_\tau) = \sum_{\mu\nu\rho} g_{\eta\mu} \epsilon^{\mu\nu\rho} \partial_{x^\nu} \underline{\mathbf{H}}_\rho$$
$$= \mathrm{j}\omega \varepsilon_0 \underline{\varepsilon}_{pl} \underline{\mathbf{E}}_\eta \quad , \tag{B.20}$$

since

$$\sum_{\nu\rho} \epsilon^{\mu\nu\rho} \Gamma^{\tau}_{\ \nu\rho} = 0 \quad , \tag{B.21}$$

one arrives at a conservative expression for the vector wave equation which looks comparably simple

$$\sum_{\mu\nu} \partial_\mu \left(\frac{1}{\underline{\varepsilon}_p \sqrt{g}} g_{\mu\nu} \partial_\nu \right) \underline{\mathbf{H}}_{(\varphi)} + \sqrt{\frac{g}{g_{\varphi\varphi}}} \mu_0 \omega^2 \underline{\mathbf{H}}_{(\varphi)} = 0 \quad . \tag{B.22}$$

B.3. Grid transformation example

As an illustration of the above formalism we consider a simple stretched cylindrical grid according to

$$z' = a_1 z + a_2 z^2 \qquad r' = b_1 r + b_2 r^2 \tag{B.23}$$

which is still orthogonal and calculate the metric quantities analytically from their definition. The corresponding metric tensor is

$$g_{\mu\nu} = \sum_i \frac{\partial x_i'}{\partial x_\mu} \frac{\partial x_i'}{\partial x_\nu}$$

$$= \begin{pmatrix} (a_1 + 2a_2 z)^2 & 0 & 0 \\ 0 & (b_1 + 2b_2 r)^2 & 0 \\ 0 & 0 & (b_1 r + b_2 r^2)^2 \end{pmatrix} , \tag{B.24}$$

and reduces to the well known metric of cylindrical coordinates for an unstretched grid as can be seen by letting $a_1 = 1,\ a_2 = 0,\ b_1 = 1,\ b_2 = 0$. Only five components of the Christoffel-symbols are non-vanishing:

$$\Gamma^0_{\ 00} = \frac{2a_2}{a_1 + 2a_2 z} \tag{B.25}$$

$$\Gamma^1_{\ 11} = \frac{2b_2}{b_1 + 2b_2 r} \tag{B.26}$$

$$\Gamma^1_{\ \varphi\varphi} = -\frac{b_1 r + b_2 r^2}{b_1 + 2b_2 r} \tag{B.27}$$

$$\Gamma^\varphi_{\ 1\varphi} = \Gamma^\varphi_{\ \varphi 1} = \frac{b_1 + 2b_2 r}{b_1 r + b_2 r^2} \quad . \tag{B.28}$$

The wave equation B.19 is then given by the lengthy expression

$$\begin{aligned} g^{00}\partial_{x^0}(\frac{1}{\underline{\varepsilon}_{pl}}\partial_{x^0}(\sqrt{g_{\varphi\varphi}}\underline{\mathbf{H}}_{(\varphi)})) - \frac{1}{\underline{\varepsilon}_{pl}} g^{00}\Gamma^0_{\ 00}\partial_{x^0}(\sqrt{g_{\varphi\varphi}}\underline{\mathbf{H}}_{(\varphi)}) \\ + g^{11}\{\partial_{x^1}(\frac{1}{\underline{\varepsilon}_{pl}}\partial_{x^1}(\sqrt{g_{\varphi\varphi}}\underline{\mathbf{H}}_{(\varphi)})) - \\ \Gamma^\varphi_{\ \varphi 1}\partial_{x^1}(\frac{1}{\underline{\varepsilon}_{pl}}\sqrt{g_{\varphi\varphi}}\underline{\mathbf{H}}_{(\varphi)}) - \frac{1}{\underline{\varepsilon}_{pl}}\Gamma^\varphi_{\ \varphi 1}\partial_{x^1}(\sqrt{g_{\varphi\varphi}}\underline{\mathbf{H}}_{(\varphi)})\} \\ - \frac{1}{\underline{\varepsilon}_{pl}} g^{11}\Gamma^1_{\ 11}\partial_{x^1}(\sqrt{g_{\varphi\varphi}}\underline{\mathbf{H}}_{(\varphi)}) + \varepsilon_0\mu_0\omega^2\sqrt{g_{\varphi\varphi}}\underline{\mathbf{H}}_{(\varphi)} &= 0 \end{aligned} \tag{B.29}$$

For comparison, this expression reduces to the known vector wave equation in cylindrical coordinates

$$\partial_r(\frac{1}{r}\partial_r(r\underline{\mathbf{H}}_{(\varphi)})) + \partial_z^2\underline{\mathbf{H}}_{(\varphi)} + \varepsilon_0\underline{\varepsilon}_{pl}\mu_0\omega^2\underline{\mathbf{H}}_{(\varphi)} = 0 \tag{B.30}$$

in the case of an unstretched grid and neglecting the $\nabla\underline{\varepsilon}_{pl}$ contributions. When comparing equation B.29 and equation B.30 we note the much higher complexity of equation B.29. The important point, however, is a potentially drastic reduction of the number of grid points (in our calculations up to a factor of 100) by a concentration of grid-lines in important regions and the FD discretisation running on an equidistant grid in the transformed space. Moreover, the grid transformations related metric can be performed with equation B.5 in an efficient numerical way.

C. List of symbols

symbol	explanation
α	ionisation degree
β	propagation constant
$f(\mathbf{r}, \mathbf{v}, t)$	phase space distribution function
$g_{\mu\nu}$	metric tensor
$\underline{\Gamma}$	reflection factor
${\Gamma^{\rho}}_{\mu\nu}$	Christoffel symbols
$\underline{\varepsilon}_r$	complex dielectric constant
E_{ion}	first ionisation energy
$\underline{\mathbf{E}}$	phasor of electric field
$\underline{\mathbf{H}}$	phasor of magnetic field
j	imaginary unit
$\mathbf{k}$	wave vector
λ_0	wave length in vacuo
λ_D	Debye length
σ	specific conductivity
ω	angular (microwave) frequency
ω_{pl}	plasma frequency
p	pressure
$\nu_{ss'}$	collision frequency between two species s,s'
$\mathbf{S}$	amplitude scattering matrix
T	temperature
$\underline{Y}$	admittance
$\underline{Z}$	impedance

D. Physical constants

symbol		value
c_0	speed of light in vacuo	$299\,792\,458 \ \mathrm{m\,s^{-1}}$
ε_0	vacuum permittivity	$(\mu_0 c_0^2)^{-1} \approx 8.854 \cdot 10^{-12} \frac{\mathrm{A\,s}}{\mathrm{V\,m}}$
μ_0	vacuum permeability	$4\pi \cdot 10^{-7} \frac{\mathrm{V\,s}}{\mathrm{A\,m}}$
e	electron charge	$1.602 \cdot 10^{-19}\,\mathrm{C}$
m_e	electron mass	$9.11 \cdot 10^{-31}\,\mathrm{kg}$
u	atomic mass unit	$1.66 \cdot 10^{-27}\,\mathrm{kg} = 1823\ \mathrm{m_e}$
h	Plank's constant	$6.626 \cdot 10^{-34}\,\mathrm{J\,s}$
k_B	Boltzmann constant	$1.381 \cdot 10^{-23} \frac{\mathrm{J}}{\mathrm{K}}$

Bibliography

[1] M. Moisan, G. Sauvé, Z. Zakrzewski, and J. Hubert. Atmospheric pressure high power Microwave Plasma Torch, the TIA design. *Plasma Sources, Sci. Technol.*, 3:584–592, 1994.

[2] M. Moisan, R. Gremier, and Z. Zakrzewski. The electromagnetic performance of a surfatron-based coaxial microwave plasma torch. *Spectrochim. Acta*, 50B(8):781–789, 1995.

[3] C.I.M. Beenakker. A cavity for microwave-induced plasmas operated in helium and argon at atmospheric pressure. *Spectrochim. Acta*, B 31:483–486, 1976.

[4] A. Disam, P. Tschö pel, and g. Tölg. Emissionsspektrometrische bestimmung von elementspuren in wäSSrigen lösungen mit einem mantelgasstabilisierten, kapazitiv angekoppelten mikrowellenplasma. *Fresenius Z. Anal. Chem.*, *310:131–143, 1982.*

[5] M. Selby and G.M. Hieftje. Taming the surfatron. *Spectrochim. Acta* **B**, 42:285–298, 1987.

[6] Q. Jin, C. Zhu, M.W. Borer, and G.M. Hieftje. A Microwave Plasma Torch assembly for atomic emission spectroscopy. *Spectrochim. Acta* **B**, 46B(3):417–430, 1991.

[7] J.A. Bittencourt. *Fundamentals of Plasma Physics.* Pergamon Press, Oxford, first edition, 1986.

[8] A. Manz, N. Graber, and H.M. Widmer. Miniaturized total chemical analysis systems: A novel concept for chemical sensing. *Sensors and Actuators*, B1:244–248, 1990.

[9] G.R. Kirchhoff and R. Bunsen. Chemical analysis by spectrum observation. *Phil. Mag.*, 20(89–98):106–109, 1860.

[10] R. Keller, J.M. Mermet, M. Otto, and H.M. Widmer. *Analytical Chemistry.* Wiley - VCH, Weinheim, 1998.

[11] A.F. Hollemann and N. Wiberg. *Lehrbuch der Anorganischen Chemie.* Walder de Gruyter, Berlin, 101 edition, 1995.

[12] Daniel A. Benoy. *Modelling of Thermal Argon Plasmas.* PhD thesis, Technische Universiteit Eindhoven, Faculteit Technische Natuurkunde, ETP, 1993.

[13] L. Ebdon, E.H. Evans, A. Fisher, and S.J. Hill. *An Introduction to Analytical Atomic Spectrometry.* John Wiley & Sons Ltd., 1998.

[14] S. Greenfield, I.L. Jones, and C.T. Berry. High-pressure plasma as spectroscopic emission source. *Analyst*, 89:713–720, 1964.

[15] R.H. Wendt and V.A. Fassel. Induction-coupled plasma spectrometric excitation source. *Anal. Chem.*, 37:920–922, 1965.

[16] S.J. Hill, editor. *Inductively Coupled Plasma Spectrometry and its Applications.* Sheffield Academic Press, Sheffield, 1999.

[17] J.A.C. Broekaert. *Ullman's Encyclopedia of Industrial Chemistry*, volume B 5, chapter Atomic Spectroscopy. VCH, Weinheim, 1994.

[18] J.A.C. Broekaert. *Plasma optical emission and mass spectrometry*, volume B 5. VCH, Weinheim, 1994.

[19] M. Huang, S.A. Lehn, E.J. Andrews, and G.M. Hieftje. Comparison of electron concentrations, electron temperatures, gas kinetic temperatures, and excitation temperatures in argon icps operated at 27 and 40 mhz. *Spectrochim. Acta* **B**, 52:1173–1193, 1997.

[20] M.R. Cave, O. Butler, J.M. Cook, M.S. Cresser, L.M. Garden, A.J. Holden, and D.L. Miles. Atomic spectrometric update – environmental analysis. *J. Anal. At. Spectrom.*, 14:279–352, 1999.

[21] P. Schramel. Consideration of inductively coupled plasma spectroscopy for trace-element analysis in bio-medical and environmental fields. *Spectrochim. Acta* **B**, 38:199–206, 1983.

[22] I.B. Brenner and A. Zander. Geoanalysis using plasma spectrochemistry - milestones and future prospects. *Fresenius J. Anal. Chem.*, 335:559–570, 1996.

[23] B. Fairmen, M.W. Hinds, S.M. Nelms, D.M. Penny, and P. Goodall. Atomic spectrometry uopdate - industrial analysis: metals, chemicals and advanced materials. *J. Anal. At. Spectrom.*, 13:233R – 266R, 1998.

[24] J.M. de Regt. *Fundamentals of inductively coupled argon plasmas.* PhD thesis, Technische Universiteit Eindhoven, Faculteit Technische Natuurkunde, ETP, Eindhoven, February 1996.

[25] J.M. de Regt, F.P.J. de Groote, J.A.M. v.d. Mullen, and D.C. Schram. Comparison of active and passive spectroscopic method to investigate atmospheric Inductively Coupled Plasmas. *Spectrochim. Acta* **B**, 51:1371–1383, 1996.

[26] F.H.A.G. Fey. *Excitation Balances and Transport in an inductively coupled Plasma.* PhD thesis, Technische Universiteit Eindhoven, Faculteit Technische Natuurkunde, ETP, Eindhoven, February 1993.

[27] J.A.C. Broekaert and U. Engel. *Encyclopedia of Analytical Chemistry*, chapter Microwave-induced plasma systems in atomic spectroscopy. John Wiley & Sons, in print.

[28] C.I.M. Beenakker, B. Bosman, and P.W.J. Bpumans. An assessment of microwave-induced plasma generated in argon with cylindrical TM_{010} cavity as an excitation source for emission spectrometric analysis of aerosols. *Spectrochim. Acta* **B**, 33:373–381, 1978.

[29] L.R. Layman and G.M. Hieftje. New computer controlled microwave discharge emission spectrometer employing microarc sample atomization for trace and micro element analysis. *Anal. Chem.*, 47:194–202, 1975.

[30] Y. Okamoto, M. Yasuda, and S. Murayama. High-power microwave-induced plasma source for trace element analysis. *Jap. J. Appl. Phys.*, 29(4):L670–L672, 1990.

[31] H. Matusiewicz. A novel microwave plasma cavity assembly for atomic emission spectrometry. *Spectrochim. Acta* **B**, 47:1221–1227, 1992.

[32] A.M Bilgic, C. Prokisch, J.A.C. Broekaert, and E. Voges. Design and modelling of a modified 2.45Ghz coaxial plasma torch for atomic spectrometry. *Spectrochim. Acta* **B**, 53:773–777, 1998.

[33] Jeroen Jonkers. *Excitation and Transport in small scale Plasmas*. PhD thesis, Technische Universiteit Eindhoven, Faculteit Technische Natuurkunde, ETP, February 1998.

[34] J. Jonkers, J.M. de Regt, J.A.M. van der Mullen, H.P.C. Vos, F.P.J. de Groote, and E.A.H. Timmermans. On the electron temperatures and densities in plasmas produced by the "torche á injection axiale". *Spectrochim. Acta* **B**, 51:1385–1392, 1996.

[35] J. Jonkers, H.P.C. Vos, J.A.M. van der Mullen, and E.A.H. Timmermans. On the atomic state densities of plasmas produced by the "torche á injection axiale". *Spectrochim. Acta* **B**, 51:457–465, 1996.

[36] J.D. Cobine and D.A. Wilbur. The electronic torch and related high frequency phenomena. *J. Appl. Phys.*, 22:835–841, 1951.

[37] R. Mavrodineanu and R.C. Hughes. Excitation in radio–frequency discharges. *Spectrochim. Acta* **B**, 19:1309–1317, 1963.

[38] U. Jechte and W. Kessler. über den anregungsmechanismus einer hf–fackelentladung bei 2400 mhz. *Z. Phys.*, 178:133–145, 1964.

[39] W. Tappe and J. van Calker. Quantitative spektrochemische untersuchungen mit hochfrequenten plasma-flammen. *Z. Anal. Chem.*, 198:13–20, 1963.

[40] N.H. Bings, M. Olschewski, and J.A.C. Broekaert. Two dimensional spatially resolved excitation and rotational temperatures as well as electron number density measurements in capacitively coupled microwave plasmas using argon, nitrogen and air as working gases by spectroscopic methods. *Spectrochim. Acta* **B**, 52:1956–1981, 1997.

[41] N.H. Bings and J.A.C. Broekaert. The use of different plasma gases (argon, nitrogen and air) for capacitively coupled microwave-plasma optical emission spectrophotometry (CMP OES): Figures of merit and temperature measurements. *Fresenius J. Anal. Chem.*, 355:242–243, 1996.

[42] Q. Jin, Y. Duan, and J.A. Olivares. Development and investigation of microwave plasma techniques in analytical atomic spectrometry. *Spectrochim. Acta*, 52B:131–161, 1997.

[43] P.W.J.M. Boumans, F.J. de Boer, F.J. Dahmen, H. Hoelzel, and A. Meier. A comparative investigation of some analytical performance characteristics of an inductively coupled radio frequency plasma and a capacitively coupled microwave plasma for solution analysis by emission spectrometry. *Spectrochim. Acta* **B**, 30:449–469, 1975.

[44] C.I.M. Beenakker. Evaluation of a microwave-induced plasma in helium at atmospheric pressures as an element-selective detector for gas chromatography. *Spectrochim. Acta* **B**, 31:173–187, 1977.

[45] A. Aziz, J.A.C. Broekaert, and F. Leis. A contribution to the analysis of microamounts of biological samples using a combination of graphite furnace and microwave induced plasma atomic emission spectroscopy. *Spectrochim. Acta* **B**, 37:318–389, 1982.

[46] E.I. Brooks and K.I Timmins. Sample introduction device for use with a microwave-induced plasma. *Analyst*, 110:557–558, 1985.

[47] P.C. Uden. *Element-specific chromatographic detection by atomic emission spectroscopy.* American Chemical Society, Washington DC, 1992.

[48] J. Hubert, M. Moisan, and A. Richard. A new microwave plasma at atmospheric pressure. *Spectrochim. Acta*, B 33:1–10, 1978.

[49] S. Luge and J.A.C. Broekaert. Use of optical emission spectrometry with microwave-induced plasma (mip) discharges in a surfatron combined to different types of hydride generation for the determination of arsenic. *Microchom. Acta*, 113:277–286, 1994.

[50] R.L.A. Sing and J. Hubert. Noise characterization of a 'surfatron' mip and the implications for fourier-transform-based detection in gc-mip-aes. *Appl. Spectrosc.*, 44:1605–1612, 1990.

[51] M. Caetano, R.E. Golding, and E.A. Key. Factorial analysis and response surface of a gas chromatogarphy microwave-induced plasma system for the determination of halogenated compounds. *J. Anal. At. Spectrom.*, 7:1007–1011, 1992.

[52] L.J. Galante, M. Selby, and G.M. Hieftje. A low-power, surfatron source for the atomic-emission-spectrometric detection of nonmetals in aqueous solution. *Appl. Spectrosc.*, 42:559–567, 1988.

[53] L.J. Galante, M. Selby, D.R. Luffer, G.M. Hieftje, and M. Novotny. Characterization of the microwave-induced plasma as a detector for supercritical fluid chromatography. *Anal. Chem.*, 60:1370–1376, 1988.

[54] M.H. Abdallah, S. Coulombe, J. Mermet, and J. Hubert. An assessment of an atmospheric pressure helium microwave plasma produced by a surfatron as an excitation source in atomic emission spectroscopy. *Spectrochim. Acta* **B**, 37:583–592, 1982.

[55] U. Richts, J.A.C. Broekaert, P. Tschöpel, and G. Tölg. Comparative study of a beenakker cavity and a surfatron in combination with electrothermal evaporation from a tungsten coil for microwave plasma optical emission spectrometry (mip-aes). *Talanta*, 38:863–869, 1991.

[56] B.W. Pack and G.M Hieftje. An improved microwave plasma torch for atomic spectrometry. *Spectrochim. Acta* **B**, 52:2163–2168, 1997.

[57] C. Prokisch and J.A.C. Broekaert. Element determination in aqueous and acetonitrile containing solutions by atomic emission spectrometry using a microwave plasma torch (MPT). *Spectrochim. Acta* **B**, 53:1109–1120, 1998.

[58] C.L. Yang, Z.X. Zhuang, Y. Tu, P.Y. Yang, and X.R. Wang. Thermospray nebulizer as a sample introduction technique for microwave plasma torch atomic-emission spectrometry. *Spectrochim. Acta* **B**, 53:1427–1435, 1998.

[59] Q.H. Jin, H.Q. Zhang, W.J. Yang, Q. Jin, and Y.H. Shi. Determination of trace silver, gold, germanium, lead, tin, and tellurium by microwave plasma torch atomic emission spectrometry coupled with an electrothermal vaporization sample introduction system. *Talanta*, 44:1605–1614, 1997.

[60] Q. Jin, F. Wang, C. Zhu, D.M. Chambers, and G.M. Hieftje. Atomic-emission detector for gas chromatography and supercritical-fluid chromatography. *J. Anal. At. Spectrom.*, 5:487–494, 1990.

[61] B.W. Pack, J.A.C. Broekaert, J.P. Guzowski, J. Poehlman, and G.M. Hieftje. Determination of halogenated hydrocarbons by helium microwave plasma torch time-of-flight mass spectrometry coupled to gas chromatography. *Anal. Chem.*, 70:3957–3963, 1999.

[62] C. Prokisch, A.M. Bilgic, E. Voges, J.A.C. Broekaert, J. Jonkers, M. van Sande, and J.A.M. van der Mullen. Photographic plasma images and electron number densities as well as electron temperature of a modified argon MPT measured by spatially resolved thomson scattering. *Spectrochim. Acta* **B**, 54(9):1253–1266, 1999.

[63] U. Engel, C. Prokisch, E. Voges, and J.A.C. Broekaert. Spatially resolved measurements and plasma tomography with respect to the rotational temperatures for a microwave plasma torch. *J. Anal. At. Spectrom.*, 13:955–961, 1998.

[64] A.M. Bilgic, K. Garloff, and E. Voges. Finite Difference calculations of electromagnetic fields in arbitrary curvilinear coordinates for coaxial microwave plasma sources. *Plasma Sources Sci. Technol.*, 8(2):325–331, May 1999.

[65] S. C. Brown. *Introduction to electrical discharges in gases.* Wiley series in plasma physics. John Wiley & Sons, New York, 1966.

[66] Michel Moisan and Jacques Pelletier. *Microwave Excited Plasmas.* Elsevier, Amsterdam, 1st edition, 1992.

[67] C.M. Fereirra and M. Moisan. *Microwave Discharges: Fundamentals and Applications.* Plenum Press (NATO ASI), New York, 1993.

[68] J. v.d. Mullen. *Excitation Equilibria in Plasmas; a Classification.* PhD thesis, Technische Universiteit Eindhoven, Faculteit Technische Natuurkunde, ETP, 1986. Published: Physics Reports (vol. 191, no. 2 & 3), North Holland (Elsevier), Amsterdam (1990).

[69] S. Chapman and T.G. Cowling. *The Mathematical Theory of non-uniform gases.* Cambrigde University Press, London, third edition, 1970.

[70] E.W. McDaniel. *Collision phenomena in ionized gases.* John Wiley & Sons, 1964.

[71] U. Engel, A. Kehden, E. Voges, and J.A.C. Broekaert. Direct solid atomic emission spectrometric analysis of metal samples by an argon microwave plasma torch coupled to spark ablation. *Spectrochim. Acta* **B**, 54:1279–1289, 1999.

[72] R.E. Collin. *Foundations for Microwave Engineering.* McGraw-Hill Inc., New York, international edition, 1992.

[73] W.H. Press, S.A. Teukolsky, W.T. Vetterling, and B.P. Flannery. *Numerical Recipes in C.* Cambridge University Press, second edition, 1992.

[74] Geoffrey V. Marr. *Plasma Spectroscopy.* Elsevier Publishing, Amsterdam, 1968.

[75] S. Murayama, H. Matsuno, and M. Yamamoto. Excitation of solutions in a 2450 MHz discharge. *Spectrochim. Acta* **B**, 23:513–518, 1968.

[76] A. Rodero, M.C. Quintero, A. Sola, and A. Gamero. Preliminary spectroscopic with helium microwave induced plasma produced in air by use of a new structure: the axial injection torch. *Spectrochim. Acta* **B**, 51:467–479, 1996.

[77] J. Cotrino, M. Saez, M.C. Quintero, A. Mendez, E. Sanchez Uria, and A. Sanz Medel. Spectroscopic determination of fundamental parameters in an argon microwave induced plasma (surfatron) at atmospheric pressure. *Spectrochim. Acta* **B**, 47:425–435, 1992.

[78] K. Kitagawa and T. Takeuchi. Spectroscopic studies of microwave excited plasmas. *Anal. Chim. Acta.*, 60:309–318, 1972.

[79] F. Liang, H.Q. Zhang, Q. Jin, D.X. Zhang, Y.H. Lei, and Q.H. Jin. Use of microwave plasma torch atomic emission spectrometry for the determination of silicon. *Fresenius J. Anal. Chem.*, 357:384–388, 1997.

[80] D.S. Hanselman, N.N. Sesi, M. Huang, and G.M. Hieftje. The effect of sample matrix on electron density, electron temperature and gas temperature in the argon inductively coupled plasma examined by thomson and rayleigh scattering. *Spectrochim. Acta* **B**, 49:495–526, 1994.

[81] M. Huang, P.Y. Yang, D.S. Hanselman, C.A. Monnig, and G.M. Hieftje. Verification of a maxwellian distribution in the icp. *Spectrochim. Acta* **B**, 45:511–520, 1990.

[82] K.A. Marshall and G.M. Hieftje. Thomson scattering for determining electron densities and temperatures in an inductively coupled plasma. i. assement of the technique for a low-flow, low-power plasma. *Spectrochim. Acta* **B**, 43:841–849, 1988.

[83] G.M. Hieftje. Plasma diagnostic for understanding and control. *Spectrochim. Acta* **B**, 47:3–25, 1992.

[84] M. Huang, D.S. Hanselman, P. Yang, and G.M. Hieftje. Isocontour maps of electron temperature, electron number density and gas kinetic temperature in the ar inductively coupled plasma obtained by laser-light thomson and rayleigh scattering. *Spectrochim. Acta* **B**, 47:765–785, 1992.

[85] M. Huang and G.M. Hieftje. Simultaneous measuement of spatially resolved electron temperatures, electron number densities and gas temperatures by laser light scattering from the icp. *Spectrochim. Acta* **B**, 44:739–749, 1989.

[86] J.M. de Regt, R.A.H. Engeln, F.P.J. de Groote, J.A.M. v.d. Mullen, and D.C. Schram. Thomson Scattering experiments on a 100 MHz inductively coupled plasma calibrated by raman scattering. *Rev. Sci. Instrum.*, 66:3228, 1995.

[87] J. Jonkers, L.J.M. Selen, J.A.M. van der Mullen, E.A.H. Timmermans, and D.C. Schram. Steep plasma gradients studied with spatially resolved thomson scattering measurements. *Plasma Sources Sci. Technol.*, 6:533–539, 1997.

[88] F. Halzen and A.D. Martin. *Quarks & Leptons.* John Wiley & Sons, New York, international edition, 1984.

[89] M. Huang and G.M. Hieftje. Thomson scattering from an ICP. *Spectrochim. Acta* **B**, 40:1387–1400, 1985.

[90] M. Huang and G.M. Hieftje. A new procedure for determination of electron temperatures and electron concentrations by thomson scattering from analytical plasmas. *Spectrochim. Acta* **B**, 44:291–305, 1989.

[91] H.-W. Bartels. Lectures on plasma physics. München, October 1993. Summer University for Plasma Physics, MPI Garching.

[92] S.J. Chang. *Introduction to Quantum Field Theory.* World Scientific, New York, international edition, 1990.

[93] M.C.M van de Sanden, G.M. Janssen, J.M. de Regt, D.C. Schram, J.A.M. v.d. Mullen, and B. van der Sijde. A combined thomson-rayleigh scattering diagnostic using an intensified photodiode array. *Rev. Sci. Instrum.*, 63:3369–3377, 1992.

[94] S. Nowak, J.A.M. van der Mullen, A.C.A.P. van Lammeren, and D.C. Schram. On the influence of water on the electron density in an argon inductively coupled plasma. *Spectrochim. Acta* **B**, 44:411–418, 1989.

[95] M. Huang, D.S. Hanselman, Q. Jin, and G.M. Hieftje. Non thermal features of atmospheric pressure argon and helium microwave induced plasmas observed by laser-light thomson scattering and rayleigh scattering. *Spectrochim. Acta* **B**, 45:1339–1352, 1990.

[96] J.F. Alder, R.M. Bombelka, and G.F. Kirkbright. Electronic excitation and ionization temperature in a high frequency inductively coupled plasma source and the influence of water vapour on plasma parameters. *Spectrochim. Acta* **B**, 35:163–175, 1980.

[97] S. Long and R. Browner. Influence of water on conditions in the inductively coupled argon plasma. *Spectrochim. Acta* **B**, 43:1461–1471, 1988.

[98] B.L. Caughlin and M.W. Blades. Effect of wet and dry nebulizer gas on the spatial distribution of electron density. *Spectrochim. Acta* **B**, 42:353–360, 1987.

[99] I. Ishii and A. Montaser. A tutorial discussion on measurements of rotational temperature in inductively coupled plasmas. *Spectrochim. Acta* **B**, 46:1197–1206, 1991.

[100] J.A.C. Broekaert. *Anal. Chim. Acta*, 196:1, 1987.

[101] H. Rau and B. Trafford. Rotationally symmetrical electric fields and electron density distributions in a microwave plasma used in optical fibre production. *J. Phys. D: Appl. Phys.*, 22:1613–1619, 1989.

[102] T.A. Grotjohn. Numerical modeling of a compact ecr ion source. *Rev. Sci. Instrum.*, 63(4):2535–2537, April 1992.

[103] T.A. Grotjohn, W. Tan, V. Gopinath, A.K. Srivastava, and J. Asmussen. Modelling the electromagnetic excitation of a compact ecr ion/free radical source. *Rev. Sci. Instrum.*, 65(5):1761–1765, May 1994.

[104] M. Walter, D. Korzec, H.M. Hütten, and J. Engemann. Computer-Aided Design of Microwave Plasma Sources: Potential and applications. *Jpn. J. Appl. Phys.*, 36(1/7B):4777–4783, July 1997.

[105] M. Walter, D. Korzec, A. Meier, A. Decker, H.-M. Hütten, and J. Engemann. Electromagnetic field simulation for planar microwave plasma source of slot antenna type. *Reports of the Institute of Fluid Science*, 10:209–216, 1997.

[106] S.V. Patankar and D.B. Spalding. A calculation procedure for heat, mass and momentum transfer in three-dimensional parabolic flows. *Int. J. Heat Mass Transfer*, 15:1787, 1972.

[107] P.C. Huang, J. Heberlein, and E. Pfender. A two-fluid model of turbulence for a thermal plasma jet. *Plasma Chemistry and Plasma Processing*, 15(1):25–46, 1995.

[108] F.J. Gordillo-Vazquez and J. Cotrino. A simplified hydrokinetic model for a steady-state microwave discharge sustained by travelling waves at atmospheric pressure conditions. *J. Appl. Phys.*, 78(7):4360–4370, 1995.

[109] G.M.W. Kroesen, D.C. Schram, C.J. Timmermans, and J.C.M. de Haas. The energy balance of a plasma in partial local thermodynamic equilibrium. *IEEE Trans. Plasma Sci.*, 18(6):985–990, 1990.

[110] E.V. Karoulina and Y.A. Lebedev. Computer simulation of microwave and dc plasmas: comparative characterisation of plasmas. *J. Phys. D: Appl. Phys.*, 25:401–412, 1992.

[111] G.M. Janssen, J. van Dijk, D.A. Benoy, M.A. Tas, K.T.A.L. Burm, W.J. Goedheer, J.A.M. van der Mullen, and D.C. Schram. PLASIMO: A general model a) applied to an argon cascaded arc plasma. *Plasma Sources Sci. Technol.*, 8, February 1999.

[112] J. Mostaghimi, P. Proulx, and M.I. Boulos. A two-temperature model of the inductively coupled rf plasma. *J. Appl. Phys.*, 61(5):1753–1760, 1987.

[113] B. Engquist and A. Majac. Absorbing Boundary Conditions for the numerical simulation of waves. *Mathematics of Computation*, 31:629–651, 1977.

[114] Gerrit Mur. Absorbing Boundary Conditions for the Finite Difference approximation of the Time-Domain electromagnetic field equations. *IEEE Trans. on Electromagnetic Compatibility*, EMC-23:377–382, November 1981.

[115] J.-P. Berenger. A Perfectly Matched Layer for the absorption of electromagnetic waves. *J. Computational Phys.*, 114(2):185–200, October 1994.

[116] R. Mittra and Ü. Pekel. A new look at the Perfectly Matched Layer (PML) concept for the reflectionless absorption of electromagnetic waves. *IEEE Microwave and Guided Wave Lett.*, 5(3):84–86, March 1995.

[117] J.D. Jackson. *Klassische Elektrodynamik.* W. de Gruyter, Berlin, New York, 1983.

[118] Kane S. Yee. Numerical solution of initial boundary value problems involving Maxwell's equations in isotropic media. *IEEE Trans. Antennas Propagat.*, AP-14(8):302–307, May 1966.

[119] M.J. Beaubien and A. Wexler. An accurate Finite-Difference method for higher order waveguide modes. *IEEE Trans. Microwave Theory Tech.*, MTT-16(12):1007–1017, December 1968.

[120] A. Taflove. *Computational electrodynamics: The Finite-Difference Time-Domain method.* Artech House, Boston, 1995.

[121] J. F. Thompson, Z.U.A. Warsi, and C. W. Mastin. *Numerical Grid Generation.* Elsevier Science Publishing Co., Inc., Amsterdam, 1985.

[122] Richard Holland. Finite-Difference solutions of Maxwell's Equations in Generalized Nonorthogonal Coordinates. *IEEE Trans. on Nuclear Science*, NS-30(6):4589–4591, December 1983.

[123] Mario Fusco. FDTD algorithm in curvilinear coordinates. *IEEE Trans. Antennas Propagat.*, 38(1):76–89, January 1990.

[124] P. H. Harms, Jin-Fa Lee, and R. Mittra. A study of the nonorthogonal FDTD method versus the conventional FDTD technique for computing resonant frequencies of cylindrical cavities. *IEEE Trans. Microwave Theory Tech.*, 40(4):741–746, April 1992.

[125] A. Taflove. *Advances in computational electrodynamics: The Finite-Difference Time-Domain method.* Artech House, Boston, 1998.

[126] S.B. Pope. The calculation of turbulent recirculating flows in general orthogonal coordinates. *J. Computational Phys.*, 26:197–217, 1978.

[127] Suhas V. Patankar. *Numerical Heat Transfer and Fluid Flow.* McGraw-Hill, New York, 1980.

[128] K. S. Yee, J. S. Chen, and A. H. Chang. Conformal Finite-Difference Time-Domain (FDTD) with overlapping grids. *IEEE Trans. Antennas Propagat.*, 40(9):1068–1075, September 1992.

[129] K. S. Yee and J. S. Chen. Conformal hybrid Finite Difference Time Domain and finite volume time doamin. *IEEE Trans. Antennas Propagat.*, 42(10):1450–1455, October 1994.

[130] N. K. Madsen and R. W. Ziolkowski. Numerical solutions of Maxwell's equations in the Time Domain using irregular nonorthogonal grids. *Wave Motion*, 10:583–596, December 1988.

[131] R. Holland. Pitfalls of staircase meshing. *IEEE Trans. on Electromagnetic Compatibility*, 35(4):434–439, November 1993.

[132] L.P. Eisenhart. *Riemannian Geometry.* Princeton University Press, Princeton, 1949.

[133] W.D. Curtis and F.R. Miller. *Differential Manifolds and Theoretical Physics.* Academic Press, Inc., San Diego, 1985.

[134] P.A.M. Dirac. *General Theory of Relativity.* J Wiley & Sons, New York.

[135] R. Barrett et al. *Templates for the Solution of Linear Systems: Building Blocks for Iterative Methods.* Society for Industrial and Applied Mathematics, Philadelphia, 1994. Available via `http://""www.netlib.org/""templates/`.

[136] M. Mitchner and C.H. Kruger. *Partially Ionized Gases.* Wiley & Sons, New York, 1977.

[137] J.A. Rees H.B. Milloy, R.W. Crompton, and A.G. Robertson. *Austr. Journ. of Physics*, 30:61, 1977.

[138] A. M. Bilgic, E. Voges, C. Prokisch, and J.A.C. Broekaert. Streifenleitungsanordnung mit integrierten Gaszuführungen für mikrowelleninduzierte Plasmaquellen zur Anwendung in der analytischen Atomspektrometrie, 1998. Patentanmeldung Nr. 198 51 628.2.

[139] A.M. Bilgic, U. Engel, E. Voges, M. Kückelheim, and J.A.C. Broekaert. A new low power microwave plasma source using microstrip technology for atomic emission spectrometry. *Plasma Sources Sci. Technol.*, 9(1):1–4, 2000.

[140] U. Engel, A.M. Bilgic, O. Haase, E. Voges, and J.A.C. Broekaert. A new microwave induced plasma based on microstrip technology and its use for the atomic emission spectrometric determination of mercury with the aid of the cold-vapour technique. *Anal. Chem.*, 72(1):193–197, 1999.

[141] A.M. Bilgic, E. Voges, U. Engel, and J.A.C. Broekaert. A low-power 2.45 GHz microwave induced helium plasma source at atmospheric pressure based on microstrip technology. *J. Anal. At. Spectrom.*, 15(6):579–580, 2000.

[142] M.D. Luque de Castro and L. Gàmiz-Gracia. Miniaturisation: a well-defined trend in separation and preconcentration techniques. *Anal. Chim. Acta*, 351:23–40, 1997.

[143] S.J. Haswell. Development and operating characteristics of micro flow injection analysis systems based on electroosmotic flow. *Analyst*, 122:1R–10R, 1997.

[144] H.T.G. van Lintel, F.C.M van de Pol, and S. Bouwstra. A piezoelectric micropump based on micromachining of silicon. *Sensors and Actuators*, 15:153–167, 1988.

[145] H.J. Ache. Chemical microanalytical systems: objectives and latest developments. *Fresenius J. Anal. Chem.*, 355:467–474, 1996.

[146] M. McEnery, A. Tan, J. Alderman, J. Patterson, S.C. O'Mathuna, and J.D. Glennon. Liquid chromatography on-chip: progression towards a μ-total analysis system. *Analyst*, 125:25–27, 2000.

[147] W. Menz and J. Mohr. *Mikrosystemtechnik für Ingenieure*. VCH, Weinheim, 2. edition, 1997.

[148] E.W. Becker, W. Ehrfeld, P. Hagmann, A. Maner, and D. Münchmeyer. Fabrication of microstructures with aspect ratios and great structural heights by synchrotron radiation lithography, galvanoforming and plastic molding (LIGA process). *Microelectron. Eng.*, 4:35–56, 1986.

[149] P. Bley. The liga process for fabrication of three-dimensional microscale structures. *Interdisc. Sci. Rev.*, 29:267–272, 1993.

[150] A. Neyer, T. Knoche, and L. Müller. Fabrication of low polymer waveguides using injection moulding technology. *Electronic. Lett.*, 29:399–400, 1993.

[151] R. Klein and A. Neyer. Silicon micromachining for microreplication techniques. *Electronic. Lett.*, 30:1672–1674, 1994.

[152] A. Neyer. Mikrostrukturen für die optische kommunikationstechnik. *Uni Report*, 26:15–22, 1998.

[153] S.C. Terry, J.H. Jerman, and J.B. Angell. A gas chromatographic air analyzer fabricated on a silicon wafer. *IEEE Trans. Electron Devices*, ED-26:1880–1886, 1979.

[154] H. Becker and C. Gärtner. Mikrosystemtechnik in den life sciences. *Phys. Blätter*, 55:51–53, 1999.

[155] A. van den Berg and P. Bergveld, editors. *Micro total analysis systems*. MESA. Kluwer Academics Publishers, Dordrecht, 1994.

[156] J.D. Harrison and A. van den Berg, editors. *Micro total analysis systems '98*. MESA. Kluwer Academics Publishers, Dordrecht, 1998.

[157] J.C.T. Eijkel, H. Stoeri, and A. Manz. An atmosperic pressure dc glow discharge on a microchip and its application as a molecular emission detector. *J. Anal. At. Spectrom.*, 15:297–300, 2000.

[158] M. Morita, J. Yoshinaga, and J.S. Edmonds. The determination of mercury species in environmental and biological samples. *Pure and Appl. Chem.*, 70:1585–1615, 1998.

[159] O. Haase, M. Klare, K. Krengel-Rothensee, and J. A. C. Broekaert. Evaluation of the determination of mercury at the trace and ultra-trace levels in the presence of high concentrations of nacl by flow injection-cold vapour atomic absorption spectrometry using $SnCl_2$ and $NaBH_4$ as reductands. *Analyst*, *123:1219–1222, 1998.*

[160] H. Kaiser and H. Specker. Bewertung und vergleich von analysenverfahren. *Fresenius' Z. Anal. Chem.*, 149:44–66, 1956.

[161] V. Liger, A. Zybin, Y. Kuritsyn, and K. Niemax. Diode-laser atomic-absorption spectrometry by the double-beam-double modulation technique. *Spectrochim. Acta* **B**, 52:1125–1138, 1997.

[162] A. Zybin, V. Liger, and Y. Kuritsyn. Dynamic range improvement and background correction in diode laser atomic absorption spectrometry. *Spectrochim. Acta* **B**, 54:613–619, 1999.

[163] J. Koch and K. Niemax. Characterization of an element selective gc-plasma detector based on diode laser atomic absorption spectrometer. *Spectrochim. Acta* **B**, 53:71–79, 1998.

[164] J. Koch, M. Miclea, and K. Niemax. Analysis of chlorine in polymers by laser sampling and diode laser atomic absorption spectrometry. *Spectrochim. Acta* **B**, 54:1723–1735, 1999.